

This is the author accepted version of:

Daubar, I. and Lognonné, P. and Teanby, N. and Miljkovic, K. and Stevanovic, J. and Vaubillon, J. and Kenda, B. et al. 2018. Impact-Seismic Investigations of the InSight Mission. *Space Science Reviews*. 214 (8): Article ID 132. <http://doi.org/10.1007/s11214-018-0562-x>

1 **Impact-Seismic Investigations of the InSight Mission**

2
3 Ingrid Daubar¹, Philippe Lognonné², Nicholas A. Teanby³, Katarina Miljkovic⁴, Jennifer
4 Stevanović^{3,5}, Jeremie Vaubillon⁶, Balthasar Kenda², Taichi Kawamura^{7,2}, John Clinton⁸,
5 Antoine Lucas², Melanie Drilleau², Charles Yana⁹, Gareth S. Collins¹⁰, Don Banfield¹¹, Matthew
6 Golombek¹, Sharon Kedar¹, Nicholas Schmerr¹², Raphael Garcia¹³, Sebastien Rodriguez²,
7 Tamara Gudkova¹⁴, Stephane May⁹, Maria Banks¹⁵, Justin Maki¹, Eleanor Sansom⁴, Foivos
8 Karakostas², Mark Panning¹, Nobuaki Fuji², James Wookey³, Martin van Driel⁸, Mark
9 Lemmon¹⁶, Veronique Ansan¹⁷, Maren Böse⁸, Simon Stähler⁸, Hiroo Kanamori¹⁸, James
10 Richardson¹⁹, Suzanne Smrekar¹, W. Bruce Banerdt¹

11
12 ¹Jet Propulsion Laboratory, California Institute of Technology, Pasadena, CA 91109, USA

13 ²Institut de Physique du Globe de Paris-Sorbone Paris Cité, Université Paris Sorbonne, Diderot,
14 75013 Paris, France

15 ³School of Earth Sciences, University of Bristol, Wills Memorial Building, Queens Road,
16 Bristol, BS8 1RJ, UK

17 ⁴Curtin University, School of Earth and Planetary Science, GPO Box U1987, Perth WA 6845,
18 Australia

19 ⁵Atomic Weapons Establishment, Aldermaston, Berkshire, UK

20 ⁶IMCCE, Paris, France

21 ⁷National Astronomical Observatory of Japan

22 ⁸ETH Zurich, Zurich, Switzerland

23 ⁹Centre National d'Etudes Spatiales, France

24 ¹⁰Dept. Earth Science & Engineering, Imperial College, London, UK

25 ¹¹420 Space Sciences, Cornell Center for Astrophysics and Planetary Science, Cornell
26 University, Ithaca, NY 14853

27 ¹²University of Maryland, Department of Geology, College Park MD 20742, USA

28 ¹³ISAE-SUPAERO, Toulouse University, 10 Ave E. Belin, 31400 Toulouse

29 ¹⁴Schmidt Institute of Physics of the Earth RAS, Moscow, Russia

30 ¹⁵NASA Goddard Space Flight Center, Greenbelt, MD 20771, USA

31 ¹⁶Texas A&M Univ., College Station, TX

32 ¹⁷LPG Nantes, UMR6112, CNRS-Université de Nantes, 2 rue de la Houssinière, BP 92208,
33 44322 Nantes cedex 3, France

34 ¹⁸California Institute of Technology, Pasadena, CA

35 ¹⁹Planetary Science Institute, Tucson, AZ

36
37
38 Copyright 2018. All rights reserved.
39

40 **ABSTRACT**

41
42 Impact investigations will be an important aspect of the InSight mission. One of the scientific
43 goals of the mission is a measurement of the current impact rate at Mars. Impacts will
44 additionally inform the major goal of investigating the interior structure of Mars.
45

46 In this paper, we review the current state of knowledge about seismic signals from impacts on
47 the Earth, Moon, and laboratory experiments. We describe the generalized physical models that
48 can be used to explain these signals. A discussion of the appropriate source time function for
49 impacts is presented, along with spectral characteristics including the cutoff frequency and its
50 dependence on impact momentum. Estimates of the seismic efficiency (ratio between seismic
51 and impact energies) vary widely. Our preferred value for the seismic efficiency at Mars is $5 \times$
52 10^{-4} , which we recommend using until we can measure it during the InSight mission, when
53 seismic moments are not used directly. Effects of the material properties at the impact point and
54 at the seismometer location are considered. We also discuss the processes by which airbursts and
55 acoustic waves emanate from bolides, and the feasibility of detecting such signals.
56

57 We then consider the case of impacts on Mars. A review is given of the current knowledge of
58 present-day cratering on Mars: the current impact rate, characteristics of those impactors such as
59 velocity and directions, and the morphologies of the craters those impactors create. Several
60 methods of scaling crater size to impact energy are presented. The Martian atmosphere, although
61 thin, will cause fragmentation of impactors, with implications for the resulting seismic signals.
62

63 We also benchmark several different seismic modeling codes to be used in analysis of impact
64 detections, and those codes are used to explore the seismic amplitude of impact-induced signals
65 as a function of distance from the impact site. We predict a measurement of the current impact
66 flux will be possible within the timeframe of the prime mission (one Mars year) with the
67 detection of ~a few to several tens of impacts. However, the error bars on these predictions are
68 large.
69

70 Specific to the InSight mission, we list discriminators of seismic signals from impacts that will
71 be used to distinguish them from marsquakes. We describe the role of the InSight Impacts
72 Science Theme Group during mission operations, including a plan for possible night-time meteor
73 imaging. The impacts detected by these methods during the InSight mission will be used to
74 improve interior structure models, measure the seismic efficiency, and calculate the size
75 frequency distribution of current impacts.
76
77

78 **Keywords**

79 InSight; Mars; Impact Cratering; Seismology
80

1 INTRODUCTION

The Discovery mission InSight (Interior Exploration using Seismic Investigations, Geodesy and Heat Transport (Banerdt et al., 2017; this volume) will study the interior of Mars using seismic signals. These will emanate from not only interior tectonic sources, but from impacts as well. This paper describes the impact-related investigations being planned for the InSight mission, and how seismic detection of impact events will further the scientific goals of the mission.

The scientific goals of the InSight mission include both the direct measurement of impacts and other science that will benefit from the information impacts provide. Measuring the rate of crater formation at the surface will achieve the goal of determining the impact flux at Mars. Impacts will also inform the major goal of investigating the interior structure of Mars, as each impact will provide a set of seismic signals that have passed through the interior. Locating the corresponding craters precisely on the surface of the planet will provide a definitive source location, something that tectonic seismic sources will most likely not be able to accomplish because they are much less likely to have identifiable surface expressions. This additional information will inform seismic ray paths, seismic velocities, and the physical properties of the material through which the rays traveled.

The InSight seismometer, SEIS (Seismic Experiment for Interior Structure; Lognonné et al., this issue) is expected to record seismic signals from a number of impactors that regularly hit the Martian surface, and from these measurements estimate the rate of meteorite impacts on the surface of Mars. In addition, impacts could add a substantial number of seismic sources to an otherwise seismically quiet planet, whose natural quake rate estimated to be ~1000 times lower than on Earth (Golombek et al, 1992; Golombek 2002; Knapmeyer et al.; 2006; Plesa et al., 2018). This is despite the planet being 100 times larger than Moon. See Lognonné & Mosser (1993), Lognonné & Johnson (2007, 2015), and Lorenz and Panning (2018) for comparisons of tectonically-driven seismicity and seismic detection perspectives.

The Impacts Science Theme Group (STG) was formed to oversee all of the impact cratering-related science of the InSight mission. Membership in the Impacts STG is open to any interested InSight science team member. The purpose of the group is to coordinate scientific analyses before and during the landed mission, and support operations to ensure the acquisition of impact-related data. Impact-related scientific analyses include the seismic source and waveform modeling of impact generated seismic signals; detection, localization, and characterization of impact sources; detection of meteors; modeling of meteor infrasound and acoustic source and shock signals; and comparative impact signal analyses between Mars, Earth and Moon.

In this paper, we summarize the current state of knowledge of impact-related seismology based on terrestrial and lunar studies, and the expectations for Martian impact seismology. The latter is based on our present understanding of the current impact rate and predictions of the Martian seismic response from the interior and atmosphere. We present a number of impact-seismic numerical models, benchmarked against each other in preparation for analysis of InSight data. Finally, Impacts STG operational and data analysis plans for the mission are also described.

127 **2 BACKGROUND**

128

129 Impacts have been recorded seismically only on our own planet and the Moon. Without prior
130 knowledge of what Martian impact-induced seismicity will look like, we must extrapolate from
131 our knowledge of those two bodies to predict what InSight will observe on Mars.

132

133 **2.1 IMPACTS IN TERRESTRIAL SEISMOLOGY**

134

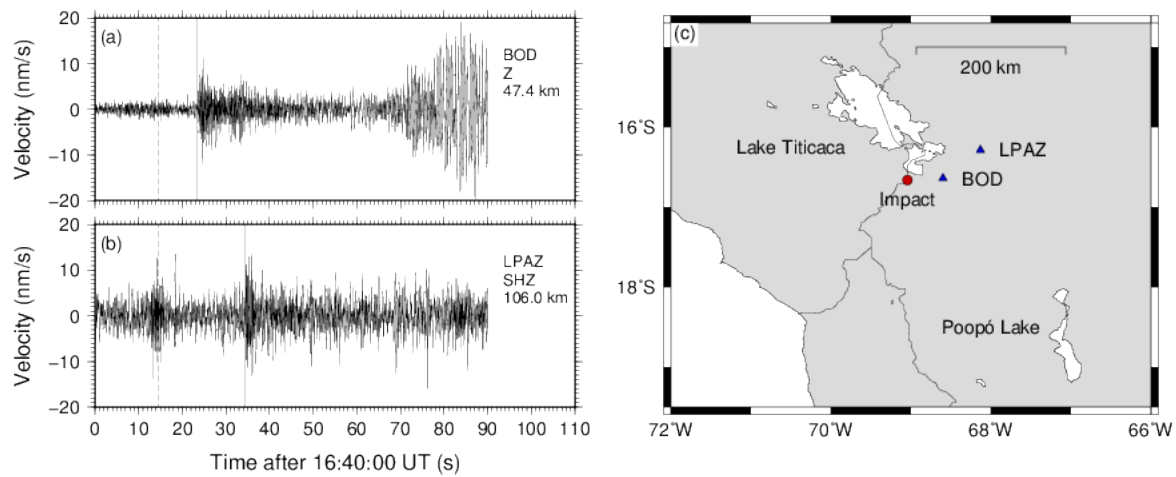
135 Seismic signals from bolides were recognized as early as the beginning of the last century, with
136 the detection of the seismic coupled airwave of the Tunguska event (Ben-Menahem, 1975,
137 Chyba et al., 1993). However, in general it is rare to detect seismic signals from meteoroid
138 impacts on the Earth's surface, because its substantial atmosphere either ablates, fragments, or
139 significantly slows the meteoroids before impact (Edwards et al., 2008). Most of the seismic
140 signals detected from impacts are therefore associated with acoustic waves that have been
141 converted to seismic waves at the Earth's surface. Earth is also farther from the asteroid belt than
142 Mars, so has about half as many meteoroids of a given size impacting the top of the atmosphere
143 (Davis, 1993; Hartmann, 2005; Williams et al., 2014), although the higher impact velocities at
144 Earth balance this effect to some degree. This is in addition to the fact that the Earth is
145 seismically very noisy, primarily due to oceanic, tectonic, atmospheric, and cultural noise
146 sources (Peterson, 1993). All these factors conspire to make detections of seismic waves from
147 impact events extremely challenging on Earth.

148

149 A recent example of an impact that gave a detectable seismic signal was the Carancas event in
150 Bolivia (Brown et al., 2008; Le Pichon et al., 2008; Tancredi et al., 2009), where an impact crater
151 with a diameter of 13.5 m formed on 15 September 2007. This event had the advantage of being
152 reported by eye witnesses, so the origin time is well constrained. There is some debate over the
153 size and speed of the impactor, which may have had its velocity reduced by atmospheric drag
154 from an original velocity of 10 km/s to subsonic speeds of a few hundred meters per second by
155 the time of impact. Adding to these complications, the impact was into water-saturated soil.
156 Therefore, this impact may not be a particularly representative example of the kind of seismic
157 signal we expect on Mars.

158

159



160

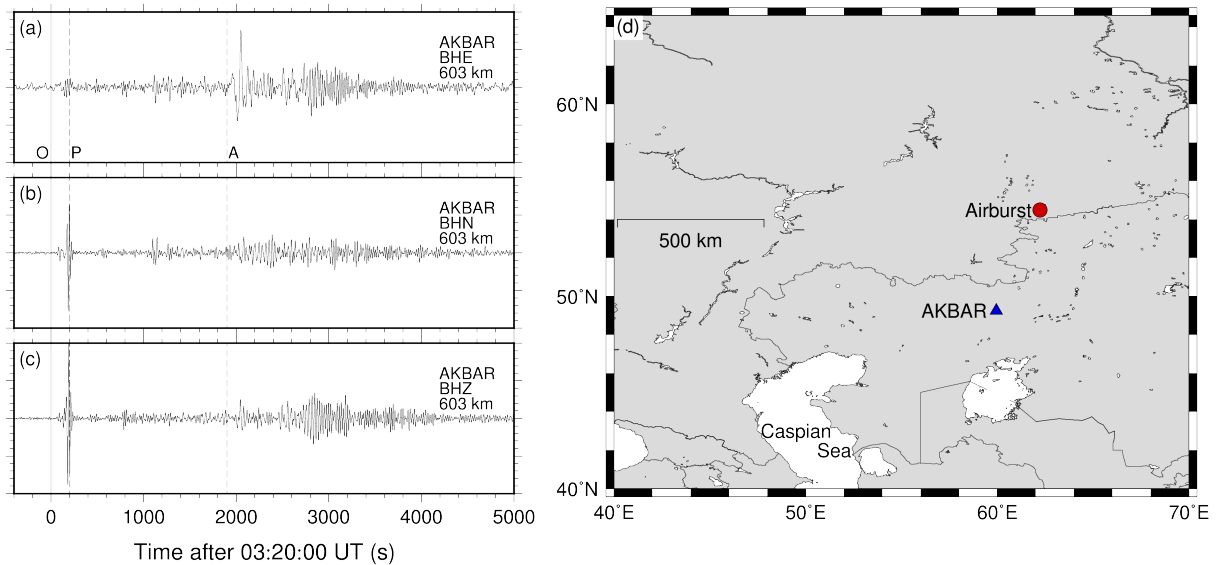
161 *Figure 1:*

162 *Seismograms from the Carancas impact event in Bolivia. (a) Vertical seismogram from the*
 163 *closest station of the Bolivian Seismic Network. Dashed vertical line shows the origin time and*
 164 *solid vertical line shows the first arrival direct P-wave. The high-amplitude long-period signal at*
 165 *70+ seconds is the airwave. (b) Seismogram recorded at the LPAZ GSN station at 106 km offset.*
 166 *At this distance, the signal is already close to the ambient noise level. (c) Location map showing*
 167 *impact and station locations.*

168

169 Figure 1 shows example seismograms from the Carancas impact recorded at distances of 47 and
 170 106 km. Because the signal is small, the event can only be seen at close distances. Hence, there is
 171 limited separation between phases, making identification and development of impact diagnostics
 172 difficult. Nevertheless, there is evidence of a reduced S-wave amplitude and a late-arriving
 173 airwave.

174



175
 176 **Figure 2:**
 177 *Seismograms from the Chelyabinsk airburst event. (a, b, c) Three component seismograms*
 178 *recorded at AKBAR seismic station. Data have been filtered with a 20–200 s bandpass filter.*
 179 *Labelled vertical lines are: O, origin time; P, seismic precursor; and A, airwave arrival. The*
 180 *airwave is a low frequency wave, travelling at the speed of sound in air, with an emergent*
 181 *character. (d) Location map showing airburst event and station location.*

182
 183 Airburst events are another potential source of seismic energy for InSight. An airburst occurs
 184 when a bolide enters a planetary atmosphere and abruptly disrupts and decelerates, depositing
 185 much of its kinetic energy into a propagating acoustic wave in a manner similar to an explosion.
 186 This event is triggered when the dynamic pressure acting on the bolide as it traverses the
 187 planetary atmosphere exceeds the strength of the object. The precise altitude of disruption is
 188 governed partially by the material properties of the bolide and partially by the atmospheric
 189 density.

190
 191 Airbursts are relatively common on Earth. The most notable recent event was the Chelyabinsk
 192 superbolide in 2013 over Russia (Brown et al. 2013), which was so large that acoustic energy
 193 coupled into the ground and was able to propagate as seismic energy (Fig. 2). Another notable
 194 example of an airburst that generated both seismic and acoustic detections was the Oregon State
 195 Bolide in 2008, which occurred directly over the US seismic array. It is expected that airbursts
 196 will be a significant source of both seismic and acoustic signals for InSight, given the larger
 197 impactor population and quieter environment (Brown et al., 2013; Stevanović et al, 2017).
 198 Section 4.5 discusses airburst events in detail, including detection plans with InSight.

199
 200 **2.2 IMPACTS IN LUNAR SEISMOLOGY**

201
 202 The first extraterrestrial seismic observations were made on the Moon by the Apollo missions.
 203 The Apollo program performed almost eight years of seismic studies from 1969-1977, including

204 five years of network observation with four seismic stations. During this time, more than 13,000
205 events were identified. Among the detected seismic events, meteorite impacts were the second
206 largest group; approximately 1,800 impacts were identified (Nakamura, 2003). On airless bodies
207 such as the Moon, impactors fall directly on the ground and generate seismic signals. This is
208 different from the Earth or Mars, where impactors first interact with the atmosphere. For a m-
209 scale impactor, deceleration in the atmosphere can lead either to an airburst combined with
210 possible subsonic surface impacts (for most terrestrial impacts), or to both an airburst and
211 supersonic ground impacts (for Martian impacts). Impactors of this scale can also be entirely
212 ablated in an atmospheric layer so that no fragments reach the ground. Thus, on planets and
213 satellites with atmospheres, small meteoroids are potentially more detectable using acoustic
214 airwaves than seismic waves, and only large impactors reach the surface. On the Moon, the lack
215 of an atmosphere implies all impacts are detected through their ground displacement alone.

216
217 Figure 3 shows an example of seismic events observed on the Moon recorded by the Apollo
218 seismic network up to a distance of 3,242 km. Because impacts are superficial events, their
219 signals propagate through the fractured megaregolith layer (brecciated material 1-3 km thick)
220 and crust twice: once below the source, and then again below the detecting station. Lunar
221 seismograms are thus characterized by intense scattering and resulting long, ringing coda
222 (backscattering waves due to heterogeneities). The scattering mainly occurs in the megaregolith
223 layer, which has been "gardened" by many impacts and as a result is highly porous and fractured.
224 Thus impact signals experience more scattering compared to endogenic events such as deep and
225 shallow moonquakes (Gudkova et al., 2011). The coda of lunar impacts are longer than that of
226 deep and shallow moonquakes and may last for as long as an hour. Fig. 4 shows an illustration of
227 the difference between the spectra of an impact and a shallow moonquake, occurring at
228 comparable distance. Clear differences in the waveform and the coda can be seen, and thus we
229 can discriminate quakes from impacts (this will be discussed further in Section 6.1).

230
231 The relationship between seismic signals and impact energy was studied using artificial impacts.
232 During the Apollo missions, the seismometers detected seismic signals generated by the lunar
233 module ascent stage and Saturn IV B booster impacts (Latham et al., 1970a; 1970b; Toksöz et
234 al., 1972). These impacts have known event times, locations, and impact energies, so they could
235 be used to calibrate the relation between the impact energy and seismic energy. Recently, the
236 Lunar Reconnaissance Orbiter Camera (LROC) imaged the actual craters of these artificial
237 impacts in high resolution, which gives another constraint on crater size for a known impact
238 energy (mass and velocity) (Wagner et al., 2017). It should be noted, however, that compared to
239 natural impacts of asteroids or comets, these artificial impactors had very low average densities,
240 low impact velocities, and in many cases highly oblique impact angles. For all of these reasons,
241 the seismic signals produced by the booster impacts may not be representative of natural
242 impacts, but they are some of the best (only) analogs available with known impact parameters.

243
244 On the Moon, natural impacts are all deduced based on seismic investigations. No crater thought
245 to be responsible for specific seismically identified events has been detected to date, a task made
246 nearly impossible by the extremely small fraction of the Moon covered by adequate Apollo
247 orbital imaging and the large location estimate errors for these events (as much as tens of
248 kilometers). Identification of exact source locations through images or other independent

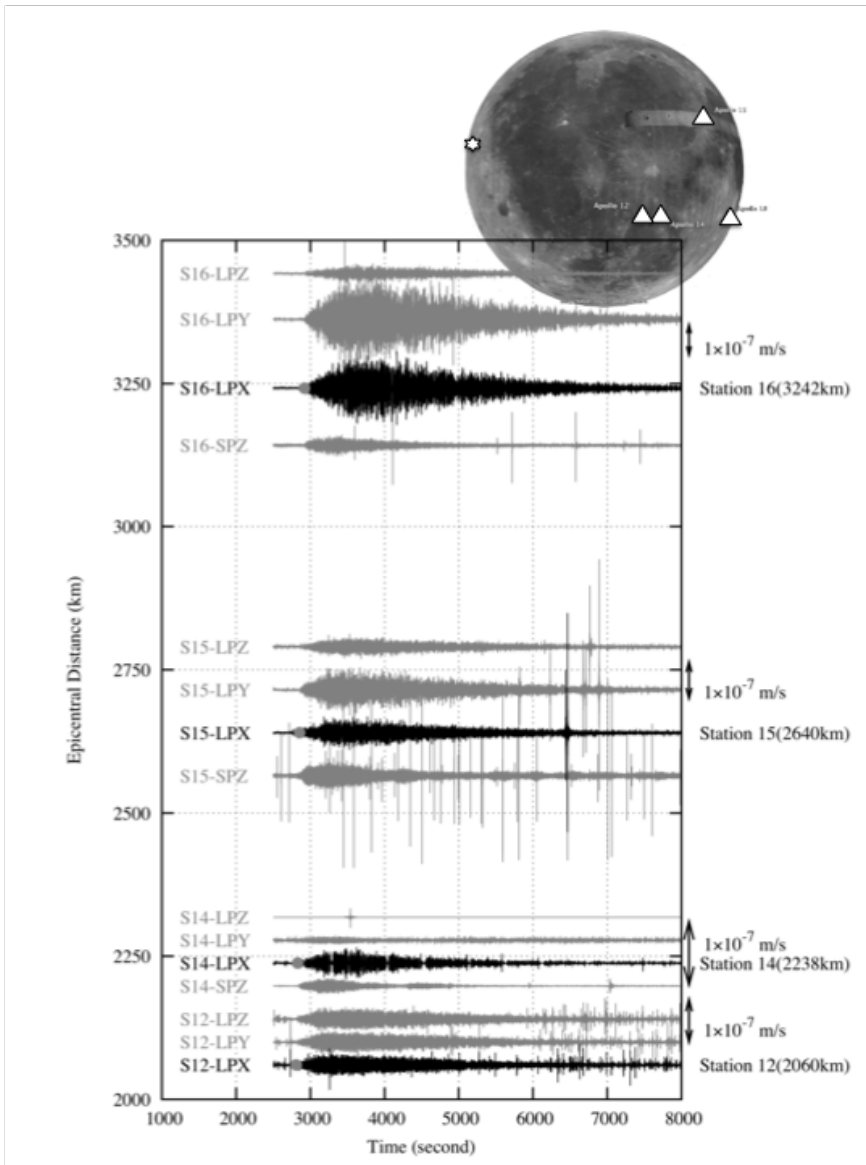
249 observations will thus be very helpful for the seismic investigations of InSight (see Section 7),
250 and the first time this will be accomplished on another planet.

251
252 Presumed impact events with high signal to noise ratios have been located through travel time
253 analyses using the Apollo seismic network. Other impacts with smaller signal to noise ratios
254 were identified through analyses of coda features and epicentral distances. Out of the 1,800
255 events listed in the Nakamura catalogue, very few have been located. One of the largest
256 collections is in Gudkova et al. (2015), with 40 locations. Even fewer natural impacts have been
257 used for lunar structural inversions (14 in Khan et al., 2002; 19 in Lognonné et al., 2003; Chenet
258 et al., 2006).

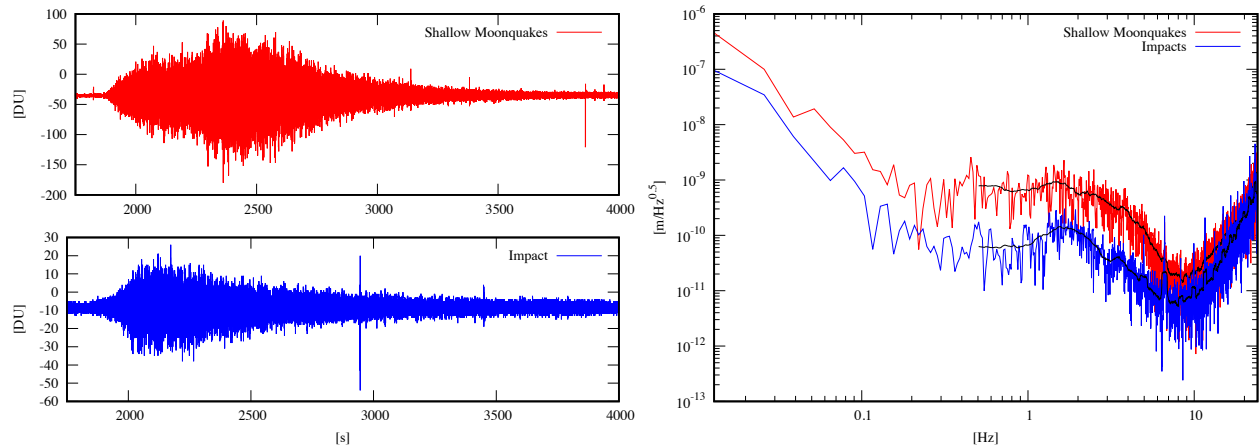
259
260 Despite these limitations, the analysis of the frequency-magnitude collection of seismically
261 detected lunar impacts has been used to estimate of the flux of meteorites in the Earth-Moon
262 system (Oberst and Nakamura, 1989; Lognonné et al., 2009; Oberst et al., 2012). Those
263 estimates were comparable to those obtained from other means.

264
265 Impacts have also provided key data for the determination of the lunar crustal thickness.
266 Surprisingly, an impact provided the deepest direct seismic ray recorded by lunar seismometry
267 (Nakamura et al, 1973). For determining the structure of the lunar crust, the best data are from
268 artificial impacts, for which times and locations are known with high precision. This provided P
269 and S travel times directly useful for structural inversions (Nakamura et al., 1976; Khan et al.,
270 2002; Lognonné et al., 2003; Gagnepain-Beyneix et al., 2006; Lognonné and Johnson, 2007;
271 2015; note corrections for timing problems made by Nakamura, 2011). Natural impacts were
272 also used for these inversions when more than three precise arrival times were measured on the
273 Apollo network. They could also be used to derive estimates of the crustal thickness at the
274 impact sites. Chenet et al. (2006) took advantage of this and carried out joint inversions with
275 seismic and gravity data to construct a 3D crustal thickness map of the Moon.

276
277



278
 279 **Figure 3:**
 280 *Ground velocity records from the Apollo seismic network of a large natural impact occurring on*
 281 *November, 14, 1976. Black seismograms indicate the axes with the best signal to noise ratio,*
 282 *which were used for arrival time readings and seismic velocity models. The mass of the impact*
 283 *has been estimated to about 25-35 tons assuming an impact velocity of 20 km/s (Gudkova et al.,*
 284 *2011). The lunar globe (LROC images; <http://photojournal.jpl.nasa.gov/catalog/PIA14011>)*
 285 *shows locations of the Apollo seismic stations (white triangles) and of the impact (white star).*
 286 *Reprinted from Lognonné & Kawamura, 2015. Note spikes are artifacts of Apollo data*
 287 *acquisition.*



289

290 *Figure 4:*291 *Comparison of waveforms and spectra from a lunar quake (red) and a lunar impact (blue).*292 *Smoothed spectra are also plotted for comparison (black and gray respectively). Both sets of*293 *data are from Apollo Station 16. The time series on the left are from the short period*294 *seismometer, and the spectra on the right are the combined spectra of long and short period*295 *seismic data. The shallow moonquake is from 1975/1/13/00:28 and the impact is from*296 *1976/1/13/7:14.*

297

298

299

300 **3 SEISMIC SIGNALS FROM IMPACTS IN GENERAL**

301

302 Seismic signals from impacts differ in several important ways from seismic signals from internal,

303 tectonic sources. First, the source function for an impact is modeled better by a single source

304 representing an explosive expansion from a point, rather than the double-coupled force typical of

305 a quake. This results in spectra with a different frequency content from an impact. Subsurface

306 material properties have a larger effect in the case of impacts, because a source depth of

307 essentially zero means the signal travels through the shallow subsurface twice, enhancing the

308 effects of e.g. a porous or fractured upper layer. Finally, in the specific case of Mars with its thin

309 atmosphere, atmospheric effects also must be taken into consideration.

310

311 Two different approaches have been developed by the community. The first one uses an

312 equivalent source function of an impact, which can then be used for modeling of synthetic

313 waveforms, in a way comparable to using seismic double couple equivalent forces for quake

314 modeling. This force is generally characterized by its long period dependency and by the

315 frequency cutoff, where that long period dependency breaks. The second approach is based on

316 the seismic energy efficiency of an impact. This is related to the amplitude of the seismic waves

317 and/or equivalent seismic moment of the source generating the waves. Here we present and

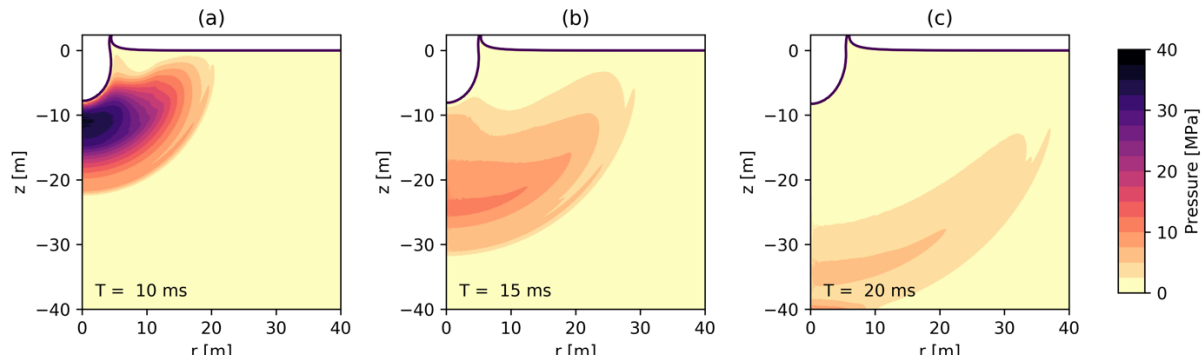
318 compare these two approaches.

319

320 **3.1 IMPACT SEISMIC EQUIVALENT SOURCE TIME FUNCTION**

321

322 An impact is a complex process during which some of the impactor's momentum and energy are
 323 transmitted to the target. For small impacts (impactors < 100 m diameter) on planets with a dense
 324 atmosphere, like Earth or Venus, almost all of the impactor's kinetic energy is deposited in the
 325 atmosphere. For planets lacking an atmosphere, the impactor hits the ground directly, where all
 326 the energy is released (for a general review of impacts in planetary seismology see Lognonné &
 327 Johnson, 2007; 2015). Mars is intermediate, where the kinetic energy of meter-scale impactors
 328 will be released both in the atmosphere during the entry and passage, and on the ground at the
 329 final impact.
 330



331
 332 **Figure 5:**
 333 *An example of an iSALE-2D hydrodynamic simulation showing a 1-m radius basalt impactor*
 334 *striking Mars regolith at 7 km/s; snapshot 10 ms (a); 15 ms (b) and 20 ms (c) after the impact.*
 335 *Note the expansion of the hemispherical shock wave; this is the primary source of seismic signal.*
 336 *The interaction with the free surface is also visible via reduction in the shock pressure close to*
 337 *the surface.*

338
 339 The seismic source, or source time function, $f(t, \mathbf{r})$, represents the associated force field acting on
 340 the planetary surface and subsurface during the impact process. Its mean amplitude will depend
 341 on the energy of the impact, and its time dependency will depend on the shock wave propagation
 342 time, during which the seismic energy is radiated. The impact source has been approximated
 343 using a variety of different methods, ranging from permanent volume injection (Richardson et
 344 al., 2005), full hydrodynamic simulations of particle motions and stress (Ivanov and Artemieva,
 345 2002), scaling laws derived from explosive and low-velocity impacts (Teanby and Wookey,
 346 2011), and as a momentum transfer (Lognonné et al., 2009; Gudkova et al., 2011; 2015). Models
 347 of seismic source time function for impacts proposed by Gudkova et al. (2011; 2015) followed
 348 analysis of lunar Apollo seismic data. Another model proposed by Shishkin (2007) is based on
 349 scaling laws and past nuclear explosion surface tests (e.g. Haskell, 1967; Werth and Herbst,
 350 1963). All of these models are a simplified view of the shock wave propagation, which generates
 351 strength failure and plastic displacements during its strong regime, and nonlinear displacements
 352 during its semi-strong regime before it transitions into an elastic wave. Fig. 5 shows a snapshot
 353 of such a shock wave for a numerical simulation of a 1-m radius impactor striking Mars regolith
 354 at an impact velocity of 7 km/s, 10 ms to 20 ms after the impact.

355
 356 Gudkova et al. (2011, 2015) (referred to hereafter as model GL) proposed that an impact signal is
 357 similar to the one generated by the release in a small shocked volume of a point force density:
 358

359
360
361
362
363
364
365
366
367
368
369
370
371
372
373
374
375
376
377
378
379
380
381
382
383
384
385
386
387
388
389
390
391
392
393
394

$$\mathbf{F}_0(t, \mathbf{x}) = F_0(t)\delta_3(\mathbf{x} - \mathbf{x}_s)Sm\mathbf{v}\frac{dg(t)}{dt},$$

with

$$F_0(t) = Sm\mathbf{v}\frac{dg(t)}{dt},$$

$$g(t) = H(t + \tau_1) H(\tau_1 - t) (1 + \cos(\omega_1 t)), \quad (1)$$

where m and \mathbf{v} are the mass and velocity of the impactor, respectively, and S is an amplification factor related to the ejecta given by Lognonné et al. (2009) as a function of the impact velocity. The source function $g(t)$ is a cosine function over half a period, $\omega_1 = \pi/\tau_1$, and $H(t)$ is the Heaviside function. For an infinite medium, such a source leads to a far field displacement as in the second column of Table 1. For P waves, it has a seismic equivalent moment provided by:

$$M(t) = v_p S m v g(t), \quad (2)$$

where v_p is the seismic velocity of body waves in the vicinity of the impact location. The amplitude of the waves is proportional to the time derivative of this moment (Gudkova et al, 2015). Although matching the Apollo signal in the body waves bandwidth, this source representation is nevertheless not compatible with any static permanent deformation which could occur near the source location, as the mean of $g(t)$ cancels out.

Table 1:

Source models used in this analysis for a homogeneous medium. The second, third and fourth column are those of the impact models of Gudkova et al. (2011; 2015) (GL), Shishkin (2007) model updating Werth and Herbst (1963) (SWH), and a classical Seismic Moment tensor model (Aki & Richards, 2002) (SM). For the SWH model, V_∞ is the volume of the fractured part of the crater and can be estimated as $\frac{4\pi}{3} \frac{\sigma_S}{\mu} \left(\frac{S_0}{\pi}\right)^{3/2}$. A dot indicates the derivative of the function.

	GL model	SWH model	SM model
Far Field displacement	$u(r, t) = \frac{1}{4\pi\rho v_p^2} Smv \frac{\dot{g}\left(t - \frac{r}{v_p}\right)}{r}$	$u(r, t) = \frac{1}{4\pi v_p \tau_0} \frac{\dot{f}\left(\frac{t - r/v_p}{\tau_0}\right)}{r}$	$u(r, t) = \frac{1}{4\pi\rho v_p^3} \frac{\dot{M}\left(t - \frac{r}{v_{pbr}}\right)}{r}$
Equivalent moment	$v_p Smv g(t)$	$\rho v_p^2 V_\infty f(t)$	$M(t)$
Units	m/s kg m/s = Nm	kg/m ³ m ² /s ² m ³ = Nm	Nm

Shishkin (2007), following Haskell (1967) and Werth and Herbst (1963), considered a source function without discontinuities for displacement, velocity and acceleration (referred to hereafter as the SWH model). The source function is defined as:

$$f(\tau) = 1 - \exp(-\tau)(1 + \tau + \tau^2/2 + \tau^3/3 - B\tau^4), \quad (3)$$

395 where τ is a non-dimensional time, defined as $\tau = t/\tau_0$, where τ_0 is the timescale of the shock
 396 wave, comparable to the α^{-1} parameter of the Rayleigh pulse model, and B is a parameter that
 397 depends on the material properties of the medium. Such a source is a generalization of the one
 398 discussed later in Section 3.3. This leads to a displacement in an infinite medium as given in the
 399 third column of Table 1. The seismic moment can then be defined as:
 400

$$401 \quad M(t) = \frac{1}{3} \frac{\sigma_s}{\mu} 4\pi\rho v_p^2 \left(\frac{S_0}{\pi}\right)^{\frac{3}{2}} f(\tau), \quad (4)$$

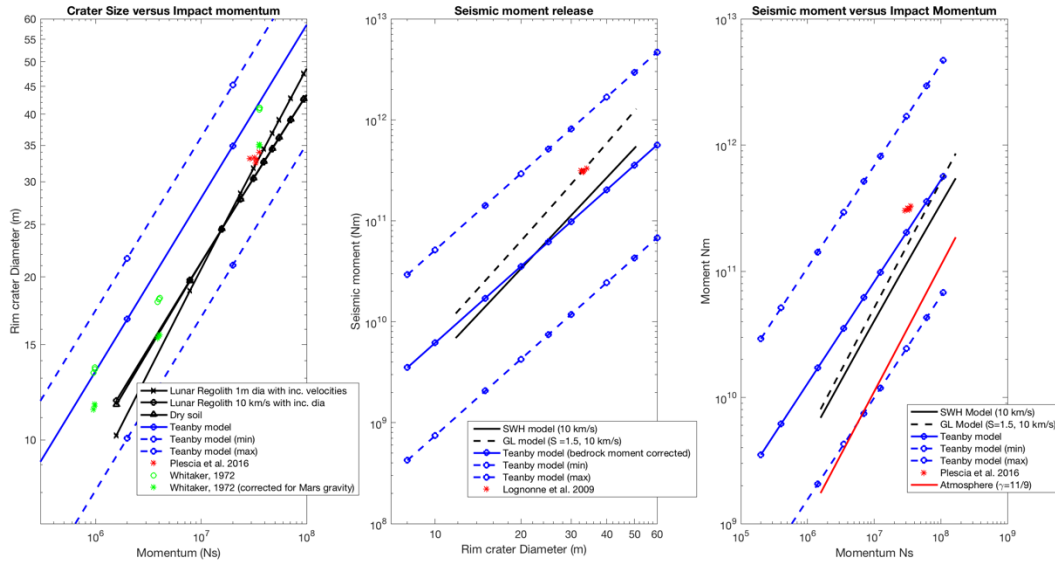
402 where σ_s , μ , and v_p are the strength, shear modulus, and P wave velocity of the impacted surface,
 403 respectively; S_0 is the surface area of the crater, and $f(\tau)$ is the normalized source function. Note
 404 that the mean of $f(\tau)$ is non-zero and that these forces are therefore compatible with a static
 405 deformation.
 406

407 Figure 6 compares the relationships between crater size and momentum, and between seismic
 408 moment and crater size. For the relationship between crater size and momentum (Fig. 6a),
 409 different study cases are shown. The first set have been computed using the Holsapple and
 410 Housen web tool (<http://keith.aa.washington.edu/craterdata/scaling/index.htm>), for different
 411 types of impacted target material (lunar regolith, dry soil and soft rocks) and for impacts with
 412 either a constant impact velocity of 10 km/s and increasing masses, or a constant mass and
 413 increasing velocities. Mars gravity ($g=3.71 \text{ m/s}^2$) and 10 mbar of pressure were assumed, as well
 414 as an impactor density of 3000 kg/m^3 . These models are compared with the diameter of the crater
 415 of the Apollo SIVB and LM impacts, as measured by Whitaker (1972) and Plescia et al. (2016),
 416 as well as with the relationship proposed by Teanby and Wookey (2011). This suggests that the
 417 Teanby and Wookey (2011) relationship tends to over-estimate crater sizes with respect to the
 418 Holsapple model and lunar observations, although the diameters are within the error bars.
 419

420 Figure 6b provides the relation between the crater size and the seismic moment obtained by the
 421 GL and SWH models for different cases compared to those proposed by Teanby and Wookey
 422 (2011). For the GL model, which is shown for the case of 10 km/s impacts in lunar regolith
 423 under Mars gravity, the ejecta amplification is set to $(1 + 0.3 \times v^{0.22})$, with the impact velocity v
 424 in km/s, following Lognonné et al. (2009). This provides an amplification factor of
 425 approximately 1.5. The GL model depends on the target material only through the amount of
 426 ejecta. The SWH model, on the other hand, depends only on the crater surface area and the ratio
 427 between shear strength and shear modulus, taken here to be 0.002. Seismic moments proposed
 428 by Lognonné et al. (2009) for Lunar Artificial SIVB impacts with the GL approach are shown,
 429 assuming for the latter the crater described in Plescia et al. (2016). Moments proposed by Teanby
 430 and Wookey (2011) are also shown but will be discussed later in the section related to seismic
 431 efficiency. As Teanby and Wookey used a moment to energy ratio based mostly on terrestrial
 432 shallow earthquakes, we assume P velocity and density of 5800 m/s and 2700 kg/m^3 for their
 433 source region. For both the GL and SWH models, the regolith density and P velocity are set to
 434 2000 kg/m^3 and 330 m/s respectively. For the three models, we corrected the moment for a
 435 reference layer with P velocity of 1000 m/s and density of 2700 kg/m^3 , which is our reference
 436 model for Mars surface bedrock. We find a relatively good agreement between the different
 437 approaches within a factor of 2 in amplitude, which is ± 0.2 in magnitude unit. All these
 438 approaches confirm that the seismic moment depends on the impactor momentum to the power 1

439 ± 0.1 (Figure 6c), and it is roughly proportional to the momentum, in accordance with the
 440 experimental observations presented in Section 3.4.

441
 442



443
 444 **Figure 6:**
 445 (A) Diameter of resulting crater as a function of impactor momentum. The Holsapple web tool
 446 was used for cases shown in black (<http://keith.aa.washington.edu/craterdata/scaling/index.htm>).
 447 For the cases with constant mass, the velocities increase from 1 km/s to 30 km/s, and a mass of
 448 1571 kg is used, corresponding to a 1 m diameter impactor with density of 3000 kg/m³. For the
 449 case with constant velocity, a velocity of 10 km/s is assumed with increasing mass, all with the
 450 same density of 3000 kg/m³. Different rheologies have been used for estimation of the crater size.
 451 The Teanby and Wookey (2011) relationship is shown in blue. Measurements of artificial lunar
 452 craters are shown in green (Whitaker, 1972) and red (Plescia et al., 2016). (B) Comparison of
 453 the seismic moments from the SWH and GL models (black, solid and dashed lines, respectively).
 454 Note that the moments are very similar and could be adjusted easily with a small change of the
 455 v_p velocity or the shear strength to modulus ratio. The apparent bedrock seismic moment using
 456 the Teanby and Wookey (2011) approach is also shown (blue). All moments are scaled for a
 457 bedrock velocity of 1 km/s and a density of 2700 kg/m³ by using the product of relation (10) and
 458 (11) of section 3.4 (C) Relationship between seismic moment and impact momentum, showing a
 459 dependency close to linear. Note that for Apollo only the vertical component of the impact is
 460 used for momentum. All other examples are assumed to be perpendicular to the surface.

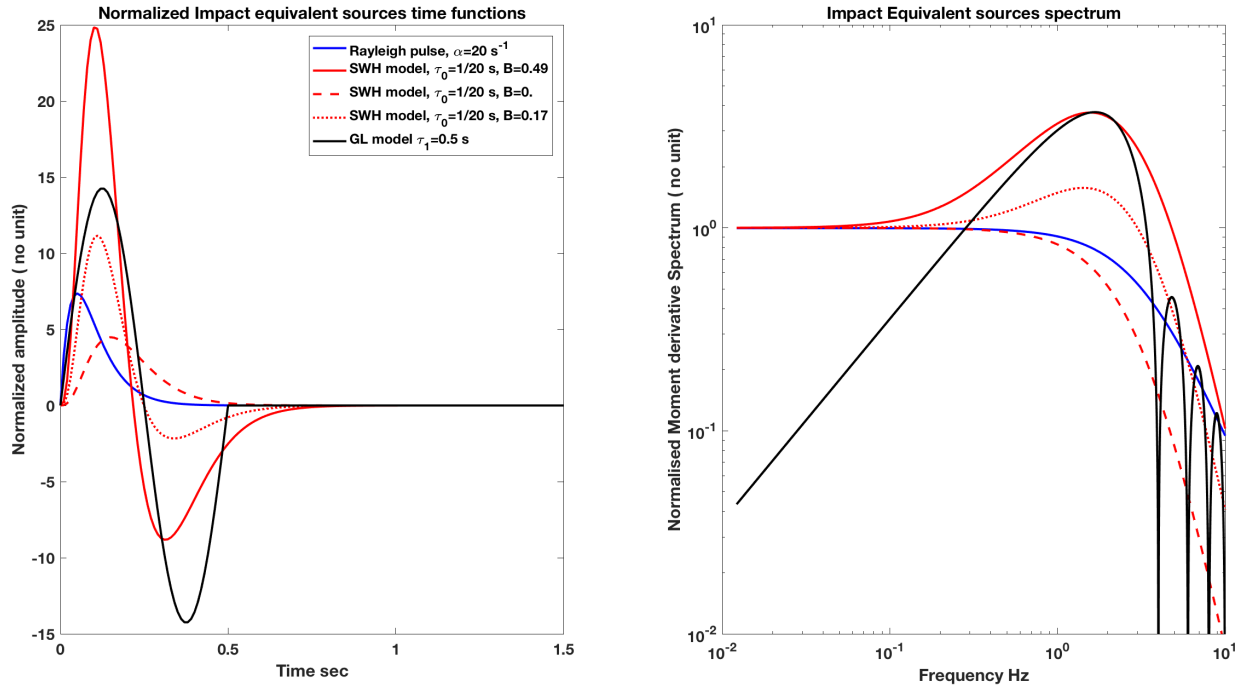
461
 462

463 3.2 SEISMIC SPECTRA, CUTOFF FREQUENCY, AND IMPACT MOMENTUM

464

465 For the three models discussed in section 3.1, Fig. 7 compares the normalized spectra of the
 466 seismic momentum derivative, as well as the displacement pulses. The case of the Rayleigh pulse
 467 of section 3.1 is also shown. All curves represent the displacement seismogram or spectrum prior
 468 to its damping by seismic attenuation. Normalized source time functions and normalized spectra

469 are shown for the GL model and the SWH model. The SWH model is shown with two different
 470 values of B, the parameter in equation 3. Based on experiments with nuclear tests in various
 471 materials (Werth and Herbst, 1963), measured values of B are 0.05 in tuff, 0.17 in rock salt, 0.24
 472 in granite, and 0.49 in alluvium (Shishkin, 2007). Values of B=0.0 and 0.49 are shown in Fig. 7
 473 as they encompass the other results.
 474



475
 476 **Figure 7:**
 477 (Left) Normalized source functions for a Rayleigh pulse $f_R(t)$ (blue), SWH model $\dot{g}(t)$ (red), and
 478 GL model $\dot{f}(t)$ (black). The SWH model is shown with three different values of the parameter B:
 479 $B=0$ (dashed red line), $B=0.171$ (dotted red line), and $B=0.49$ (solid red line). Values of $B=0.24$
 480 and $B=0.49$ correspond to nuclear tests performed in granite and alluvium, with P velocities of
 481 4.08 and 1.71 km/s, respectively. The solid black line is the GL source function. The parameters
 482 α (Rayleigh pulse) and τ_0 are equal to 20 s^{-1} and 0.05 s respectively, while τ_1 is taken as 0.5 s and
 483 has a cutoff frequency comparable to the $B=0.49$ SWH spectrum. (Right) Spectra of the same
 484 functions, which all have a similar cutoff frequency of $\sim 2 \text{ Hz}$. Spectra for earthquakes with both
 485 ω^2 and ω^3 mechanisms will have a flat long-period spectrum comparable to those of the
 486 Rayleigh pulse or $B=0$ SWH models, without the overshoot of SWH when B is not equal to zero.
 487

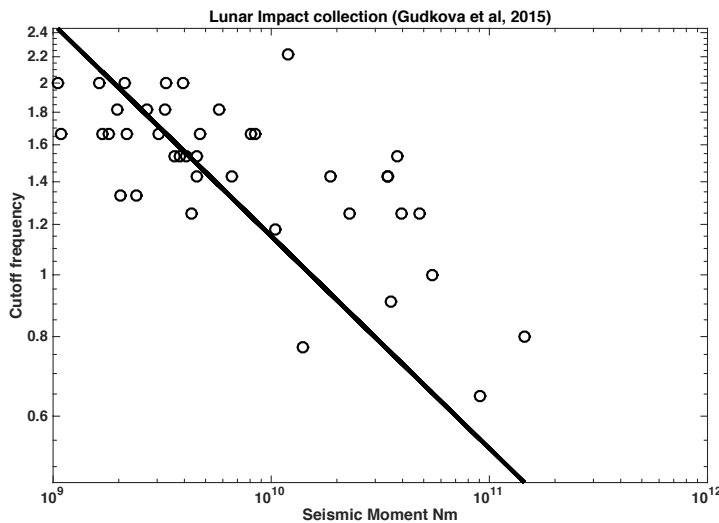
488 The comparison with the GL model is interesting, as within the bandwidth of the Apollo data,
 489 $\sim 0.2 \text{ Hz}$ - 5 Hz , the long period differences between the spectra were likely below the instrument
 490 resolution, and the shape of the spectra are therefore very similar. Note that the SWH models for
 491 large B values have a frequency overshoot at body wave frequencies, which might increase the
 492 amplitudes of 1-2 Hz body waves by a factor of ~ 4 . This is similar to the amplitudes observed in
 493 lunar data. Such overshoot also seems likely on Mars, as low-velocity materials are also expected
 494 in the subsurface (see Section 3.4).
 495

496 The key difference between SWH and GL models is obviously the long period dependency of
 497 the spectrum. SWH spectra are flat at very long periods while the GL has a slope of 20 db per
 498 decade. InSight data will be useful to determine which of the two models is a better match to
 499 observations. A key difference will be whether or not long-period surface waves are generated.

500
 501 The cutoff frequency, which is proportional to the inverse of the time-duration of the seismic
 502 excitation process, is defined for the non-zero B SWH or GL models as the peak of the
 503 displacement spectrum. While for B=0 or more classical tectonic quakes with ω^2 and ω^3 spectra,
 504 it is defined as the frequency for which the spectrum of displacement amplitudes has decayed by
 505 $\sqrt{2}$. This quantity will scale with the energy and propagation speed of the shock waves. From the
 506 scaling law of the elastic stored energy for the same process, we can expect this scaling to be:

$$507 \quad f_{cutoff} = f_{ref} \left(\frac{M}{M_{ref}} \right)^{-1/3} \left(\frac{v_p}{v_{pref}} \right)^{5/3}, \quad (5)$$

508
 509 where M , v_p , and f_{cutoff} are the seismic moment, P-wave velocity, and cutoff frequency,
 510 respectively; and M_{ref} , v_{pref} , and f_{ref} are those quantities for a reference event. We assume that the
 511 v_p/v_s ratio and the σ_s/μ ratio are equivalent for both events. Fig. 8 illustrates this scaling law for
 512 the lunar impact collection of Gudkova et al. (2015), for $v_p=300$ m/s, $f_{ref} = 1.15$ Hz and $M_{ref} =$
 513 10^{10} Nm. Most likely, the shallow subsurface seismic velocities on Mars will be larger than those
 514 of the Moon due to the less well-developed regolith. Larger velocities by a factor of 50% would
 515 shift the frequencies by a factor of two. Thus a 20 meter diameter crater associated with a 2×10^7
 516 Ns impulse and a 10^{10} Nm seismic moment might have a cutoff frequency of 2.3 Hz.
 517
 518



519
 520 **Figure 8:**
 521 *Cutoff frequencies for lunar impacts as a function of the reported impactor momentum (circles)*
 522 *as reported by Gudkova et al (2015). The black line is the best fit scaling law found for $v_p = 320$*
 523 *m/s and a reference nuclear test performed in alluvium (equation 5).*
 524

525 The cutoff frequency of an impact depends not only on the source size, but also on the properties
526 of the impacted target material (e.g., porosity) (Lognonné et al, 2009; Gudkova et al., 2011).
527 Modeling the variation in the cutoff frequency with the regolith porosity in the vicinity of the
528 impact for the Moon shows that the larger the impact, the higher the impact duration, for impacts
529 occurring in the same area of the surface. However, among impacts in different regions, this is
530 not necessary valid. Differences between the source cutoff frequencies for impacts with the same
531 momentum are caused by excitation processes in different geological regions and therefore by
532 acceleration or deceleration of the shock wave associated with the collapse of subsurface
533 porosity. The study by Gudkova et al. (2015) suggests a sensitivity of the cutoff frequency to the
534 regolith porosity: the lower the time-duration of the process, the lower the maturity of the
535 regolith. Similar analysis of future impact seismic data on Mars might enable remote
536 investigation of the lateral variations in the Martian regolith.
537

538 **3.3 SEISMIC EFFICIENCY**

539
540 The second approach developed to estimate the amplitude of seismic waves is based on the
541 energy of the impact. A large portion of an impact's energy will be released as heat, and a small
542 portion will be converted to seismic energy. The seismic efficiency, k , is defined as the ratio of
543 the seismic energy produced by an impact (E_s) to the kinetic energy of the bolide (or the yield of
544 an explosion, E). This parameter describes the fraction of the kinetic energy of the object that is
545 converted into seismic energy in the form of seismic waves (McGarr et al., 1969; Latham et al.,
546 1970b; Patton and Walter, 1993; Walker, 2003; Teanby and Wookey, 2011).
547

548 Empirical quantification of k is very difficult as it requires integration of the entire seismic wave
549 field, and the seismic efficiency differs widely between impacts, surface explosions and buried
550 explosions. Due to the lack of high signal to noise impact events on Earth, k has been estimated
551 from numerical models (Walker, 2003; Güldemeister and Wünnemann, 2017) and scaling laws
552 (Shishkin, 2007), laboratory experiments (McGarr et al., 1969; Richardson and Kedar 2013 and
553 section 3.4), nuclear detonations (Pomeroy, 1963; Patton and Walter, 1993), missile impacts
554 (Latham et al., 1970b), and artificial lunar impacts (Latham et al., 1970a). These events can
555 differ from impacts in their physical processes, temporal and/or spatial scales, and their energies.
556 The derived values span five orders of magnitude from $k = 10^{-6}$ – 10^{-1} . Some of this broad range
557 can be attributed to incomplete coverage of the seismic wavefield or frequency limitations of the
558 recording seismic instruments. However, there is also likely to be a large scenario-dependent
559 component that depends upon the surface material properties and properties of the impactor, such
560 as density and speed.
561

562 Experimental values range from 10^{-5} to 10^{-3} for impacts on bonded sand (McGarr et al. 1969;
563 Richardson and Kedar 2013). On the other hand, the artificial impacts of the Apollo 12 and 13
564 Saturn boosters, which had energy seven orders of magnitude larger, gave smaller values of 10^{-6}
565 to 10^{-5} (Latham et al. 1970a). Underground explosions have much higher seismic efficiencies of
566 10^{-2} to 10^{-1} (Patton and Walter 1993). While explosive sources may approximate some of the
567 processes found in impacts, these phenomena clearly differ in their physics. The seismic
568 efficiencies obtained from chemical and nuclear explosions do not necessarily capture the
569 momentum transfer dominated source mechanisms found in high velocity impacts. Generally,
570 though, seismic efficiency is coupled to target properties: high seismic efficiencies ($k > 10^{-3}$) are

571 typically found in explosions and nuclear tests in bedrock or highly consolidated materials (e.g.,
572 Patton and Walter, 1993), while low seismic efficiencies ($k < 10^{-5}$) are seen in sediments or
573 unbonded sands or soils (McGarr et al., 1969; Latham et al., 1970a). Recent studies for the Moon
574 and Mars have used values of 10^{-6} (Davis 1993) and 2×10^{-5} (Teanby and Wookey 2011).
575 Lognonne et al. (2009) proposed that the seismic efficiency depends on both the seismic velocity
576 at the point where the impact occurs and the duration of the source. They estimated $k = 10^{-5}$ for a
577 duration of 0.35 sec in lunar regolith.

578
579 Shishkin (2007) suggests that the seismic efficiency for impacts is on the upper side for small
580 impacts, with values of 10^{-3} or more for small impacts at Mach 10 with respect to the P wave
581 seismic velocities. The GL model provides the ratio between seismic moment M and the kinetic
582 energy as $k_m = 2S \frac{v_p}{v}$. It is therefore 2-3 times the inverse of the Mach ratio and will be about
583 1/10 for an impact at 10 km/s over a surface with 350 m/s P wave velocity. When combined with
584 the ratio between seismic energy and moment:

$$\frac{E_s}{M} = c \frac{\sigma}{\mu} \quad (6)$$

587
588 with estimated values for c of 0.22, 0.27, and 0.5 for impacts, explosions, and quakes,
589 respectively, and a ratio $\frac{\sigma}{\mu} = 2 \times 10^{-3}$, we get a seismic efficiency of $k = 4 - 5 \times 10^{-5}$. This is
590 comparable to experimental values (Latham et al., 1970b; McGarr et al., 1969). This ratio might
591 be smaller on the Moon than on Mars, as impact velocities are larger and subsurface velocities
592 are smaller, leading to a higher impactor Mach number.

593 594 **3.4 EXPERIMENTAL DETERMINATION OF SEISMIC SOURCE TIME FUNCTION** 595 **AND SEISMIC EFFICIENCY**

596
597 To experimentally measure some of these parameters, it is necessary to simulate the seismic
598 signals expected from meteorite impacts on the Martian surface. Richardson and Kedar (2013)
599 carried out a series of high velocity (1-6 km/s) impact experiments at the NASA Ames Vertical
600 Gun Range (AVGR) facility. The experiments spanned a variety of projectile impact velocities
601 and angles and were carried out in near-vacuum to mimic Martian atmospheric conditions.
602 Seismic sensors were embedded in target material analogous to the Martian surface, and they
603 were digitally recorded at over 100,000 samples per second with seismic data loggers and high-
604 speed cameras. A detailed experiment description will be summarized in a future paper. Here we
605 summarize the key results and specific implications to the InSight mission.

606
607 In the experiment, 15 accelerometers were embedded in rows horizontally along the surface of a
608 sand target, as well as below the impact point. These were used to measure signals from the
609 impacting glass projectiles, which were used to derive both the seismic velocity ($V_p = 250$ m/s)
610 and quality factor ($Q \sim 5$) of the medium. We used the record from an accelerometer placed 0.2
611 m below the impact point to determine the source time function of the impact process. This was
612 done by deconvolving the impulse response of the medium with the above properties from the
613 seismic record. Once a source time function, $F(t)$ (force as a function of time), was determined, it
614 was integrated and compared with the known momentum of the projectile, whose mass and
615 speed were accurately measured for each shot. Table 2 compares the measured projectile

616 momentum and the momentum estimated from the accelerometer records. In addition, seismic,
 617 efficiency was estimated from seismograms of three sensors at 0.2, 0.4, and 0.6 m below the
 618 impact point.

619

620 *Table 2*

621 *Experimental results for various projectile velocities. Comparison between projectile momentum*
 622 *measured in the lab and estimated from seismograms, and the resulting seismic efficiency*
 623 *estimates.*

624

Projectile velocity (km/s)	Measured projectile momentum (kg·m/s)	Estimated projectile momentum (kg·m/s)	Seismic Efficiency, k
0.95	0.28	0.37	$3.1 \times 10^{-3} \pm 0.7 \times 10^{-3}$
2.23	0.66	0.68	$1.3 \times 10^{-3} \pm 0.7 \times 10^{-3}$
2.68	0.80	0.82	$1.3 \times 10^{-3} \pm 0.7 \times 10^{-3}$
4.68	1.39	1.43	$1.4 \times 10^{-3} \pm 1.0 \times 10^{-3}$
5.47	2.05	2.05	$2.1 \times 10^{-3} \pm 2.0 \times 10^{-3}$

625

626 The generally good agreement between the measured and estimated projectile momentum serves
 627 as an independent confirmation of the measured material properties (V_p and Q), and lends
 628 credence to the estimated source time function, $F(t)$.

629

630 Other impact experiments (e.g., Gueldemeister and Wuennemann, 2017) worked in the same
 631 impact speed range as in Table 2 but impacted quartz ($k=3 \times 10^{-3}$), sandstone with 20% porosity
 632 ($k=2.56 \times 10^{-3}$), and tuff with 43% porosity ($k=2.02 \times 10^{-3}$). They used numerical impact
 633 hydrocodes to reproduce these impact events and calculate the seismic efficiencies.

634

635 The large uncertainty in impact seismic efficiency is due to the difficulty in accurately estimating
 636 E_s from a seismogram. This requires assumptions about poorly known seismic energy flux,
 637 which depends on source geometry and material properties. However, once $F(t)$ is determined
 638 with a high degree of confidence, it can be used to estimate E_s . We do this, using a method
 639 routinely employed in the analysis of seismic waves emanating from an explosion source
 640 (Helmberger and Hadley, 1981), in which a simple yet integrable mathematical function is used
 641 to represent $F(t)$.

642

643 We can represent $F(t)$ by a function known as a Jeffreys Pulse:

644

$$645 \quad f_J(t) = cte^{-\alpha t} \quad (7)$$

646

647 Where c is a constant of integration with units of force per unit time, and α is a characteristic
 648 decay time estimated from $F(t)$. By definition, the impact impulse is

649

$$650 \quad P \equiv \int_0^{\infty} F(t)dt = mv \quad (8)$$

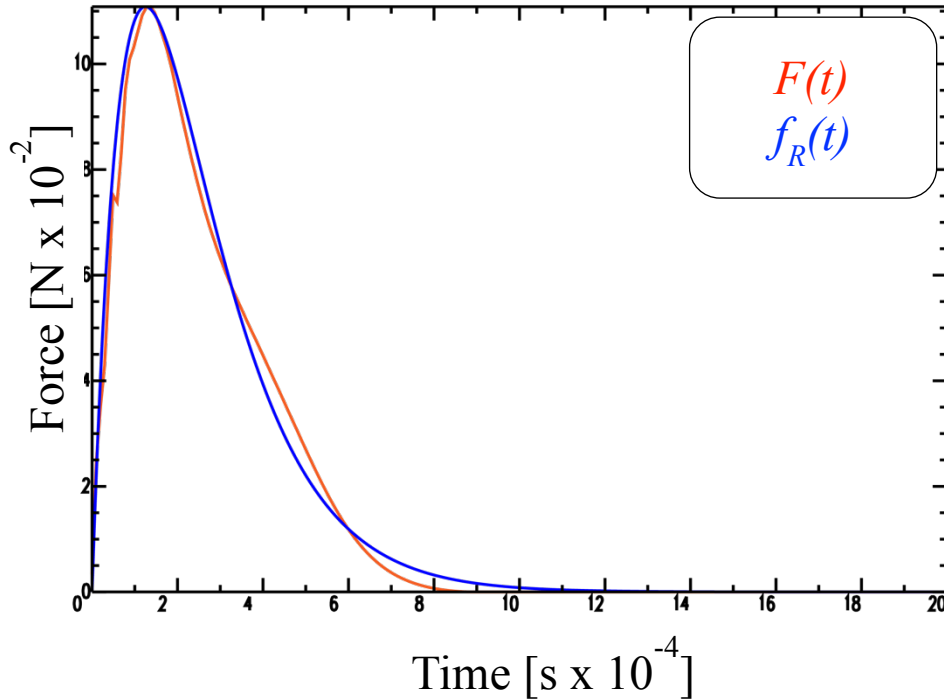
651

652 where m is the mass of the projectile and v is its velocity. Substituting $f_J(t)$ for $F(t)$, it can be
 653 shown that

654
655
656
657
658
659

$$c = \alpha^2 P \quad (9)$$

Figure 9 shows a comparison between the estimated $F(t)$ and its representation as a Jeffreys pulse $f_J(t)$, showing the close match between our estimated source time function and that measured in the experiment.



660
661
662
663
664
665
666
667
668
669
670
671
672
673
674
675
676
677
678
679
680

Figure 9: A comparison between the estimated source time function (red) for a vertical 1000 m/s shot and its mathematical representation (blue) as a Jeffreys pulse.

The seismic efficiency values summarized in Table 2 are a few times larger than the in-crater estimates (5.7×10^{-4}) obtained in laboratory experiments by Yasui et al (2015). As pointed out by Yasui et al (2015), however, estimates of the seismic efficiency from measurements outside the crater rim are substantially lower, which to some degree accounts for the wide range of seismic efficiencies quoted in the literature. As a result, the use of seismic efficiency in modeling of impacts introduces a substantial uncertainty. Using the source time function enables a more accurate estimate of the impact force time history based on a known empirical crater-size – momentum relationship (Melosh, 1989), and so eliminates the need to rely on the highly variable seismic efficiency factor. Using this strategy, we anticipate that newly discovered Martian impacts by InSight could be more accurately used for inverting for Martian interior properties.

When attempting to link seismic moment to the observed seismic efficiencies from tests, it is important to take into account that impact sources are not usually located in bedrock, but in brecciated material with low seismic velocities. For the same seismic moment, this leads to amplitudes larger by a factor of

681
$$T_m = \frac{\rho_{br} v_{pbr}^3}{\rho v_p^3}, \quad (10)$$

682
 683 where ρ_{br} and ρ are the densities of the bedrock and regolith, respectively, and v_{pbr} and v_p are the
 684 P-wave seismic velocities in each. On the other hand, only a fraction of the amplitude of the
 685 wave will be transmitted to the underlying bedrock and thus could be detected remotely. The
 686 transmission coefficient for this is approximated as

687
 688
$$T_m = \frac{2\rho v_p}{\rho_{br} v_{pbr} + \rho v_p}. \quad (11)$$

689
 690 When compared to quakes occurring in bedrock, the moment above shall therefore be multiplied
 691 by the two conversion factors, equations 10 and 11. The amplitude then depends only on the
 692 bedrock density and on the regolith and bedrock velocities. For a ratio of e.g. 10 between the
 693 surface velocity and that in the seismic crust, this will lead to magnitudes a factor of 1.5 larger.
 694 For example, a typical 10^{10} Nm moment impact associated with a 20 m crater would only be a
 695 magnitude 0.65 event. This would be comparable to a quake of magnitude 2.15 in terms of
 696 seismic amplitudes, with a possible overshoot at 1-2 Hz of 4 ± 1 leading to body waves at 1 Hz,
 697 close to those from a magnitude 2.5 seismic event. This type of effect is illustrated in Fig. 6b,
 698 where we compare the three models of seismic sources with the seismic moment provided by
 699 Teanby and Wookey (2011), all scaled for bedrock properties comparable to those of the Moon
 700 ($v_{pbr} = 1000$ m/s and $\rho_{br} = 2700$ m/s). With these modifications, the two seismic source-based
 701 models, SWH and GL, and the seismic efficiency-based model (Teanby and Wookey 2011) then
 702 agree well with the Apollo recorded observations.

703
 704 As the exact value of the seismic efficiency remains by its nature uncertain, we will use a fixed
 705 value of 5×10^{-4} in InSight impact detection studies when needed. We judge this to be the current
 706 best estimate of k . It is within an order of magnitude of most other literature estimates and the
 707 AVGR impact experiments by Kedar and Richardson (2013) described in this section. As further
 708 evidence that this value is appropriate, it brings disparate methods into rough agreement: Teanby
 709 and Wookey (2011) use a modelling approach to impact detection, whereas Teanby (2015) uses
 710 an independent empirical based scaling relation. Agreement between the two methods is
 711 obtained if $k=5 \times 10^{-4}$ is used, suggesting this value is a good estimate. There is still likely to be an
 712 order of magnitude error in those results, though, due to scatter in the data used by Teanby
 713 (2015). Given the variations between values found by various authors, we still consider this
 714 value to have an order of magnitude uncertainty, because the efficiency is expected to depend on
 715 properties of the impact (momentum, velocity, impact angle, etc.) and the seismic properties of
 716 the impacted surface material.

717
 718 **3.5 SHALLOW SUBSURFACE EFFECTS**

719
 720 Much of the above theory was developed assuming a perfect medium in which the seismic waves
 721 travel from the source (impact site) to the detector (SEIS deployment location at the InSight
 722 landing site). However, the specific material properties of those two locations, as well as the path
 723 between them, will also affect the seismic signals received. This is true for impacts as well as for

724 tectonic events, with the difference being that with impacts, we have a chance of identifying the
725 precise source and then investigating the local geology at that location.

726
727 Understanding the material properties at the landing site are important for interpretation of any
728 received signals. The presence of a surface layer of fragmented, loose regolith will both amplify
729 and trap seismic waves; and the relatively high porosity of the regolith will affect the seismic
730 efficiency. In comparison to earthquakes or marsquakes, these effects might be further amplified
731 by the fact that the body waves from impacts will likely be relatively high frequency. When they
732 are detectable, they will be in a frequency bandwidth of 0.5 to 5 Hz (Section 3.2), leading to
733 possible site effects at high frequencies due to the expected low seismic velocities in the shallow
734 subsurface (Delage et al., 2017).

735

736 **3.5.1 MATERIAL EFFECTS AT DETECTOR SITE**

737

738 In general, geophysical knowledge of *a priori* subsurface structure of Mars is based on a
739 combination of orbital and *in situ* observations: HiRISE (High Resolution Imaging Science
740 Experiment; McEwen et al., 2007), CTX (Context camera; Malin et al., 2007) and CRISM
741 (Compact Reconnaissance Imaging Spectrometer for Mars; Murchie et al., 2007) images from
742 the Mars Reconnaissance Orbiter (MRO), the radar and thermophysical properties of the surface
743 materials, including albedo, thermal inertia and radar reflectivity (and inferred bulk density)
744 (e.g., Golombek et al., 2008). Our knowledge of the material properties of the local InSight
745 region come from remote sensing data studied extensively when selecting the InSight landing
746 site (Golombek et al., 2017). The selected landing site is located in western Elysium Planitia at
747 4.5°N, 136.0°E at an elevation of -2.6 km. This is just north of the global dichotomy boundary
748 between elevated heavily cratered southern highlands and lower standing, less cratered, northern
749 plains. The landing site is on Hesperian basaltic lava plains that are ~200 m thick and are
750 underlain by sediments. Moderately low thermal inertia and measurement of rocks in high-
751 resolution images show the regolith has few rocks and is composed of dominantly cohesionless
752 sand or very weakly cemented soils (Golombek et al., 2017). Impact and eolian processes have
753 created a fragmented regolith 3–17 m thick, which grades into coarse, blocky ejecta overlying
754 strong, jointed bedrock (Warner et al., 2017). This bedrock is a ~200 m thick stack of layered
755 lava flows, possibly interbedded by ash and sedimentary deposits (Golombek et al., this issue).
756 Knapmeyer et al. (2017) used this stratigraphy, along with laboratory measurements (Delage et
757 al., 2017), to develop a model of elastic properties with a rapid stepwise increase in seismic
758 velocity and seismic attenuation Q with depth. See also Morgan et al. (this issue) for a pre-
759 landing assessment of regolith properties at the landing site. Data from the HP³ hammering
760 (Kedar et al., 2017; Spohn et al., this issue) will tightly constrain local regolith properties and
761 subsurface geology before science monitoring begins.

762

763 **3.5.2 MATERIAL EFFECTS AT IMPACT SITE**

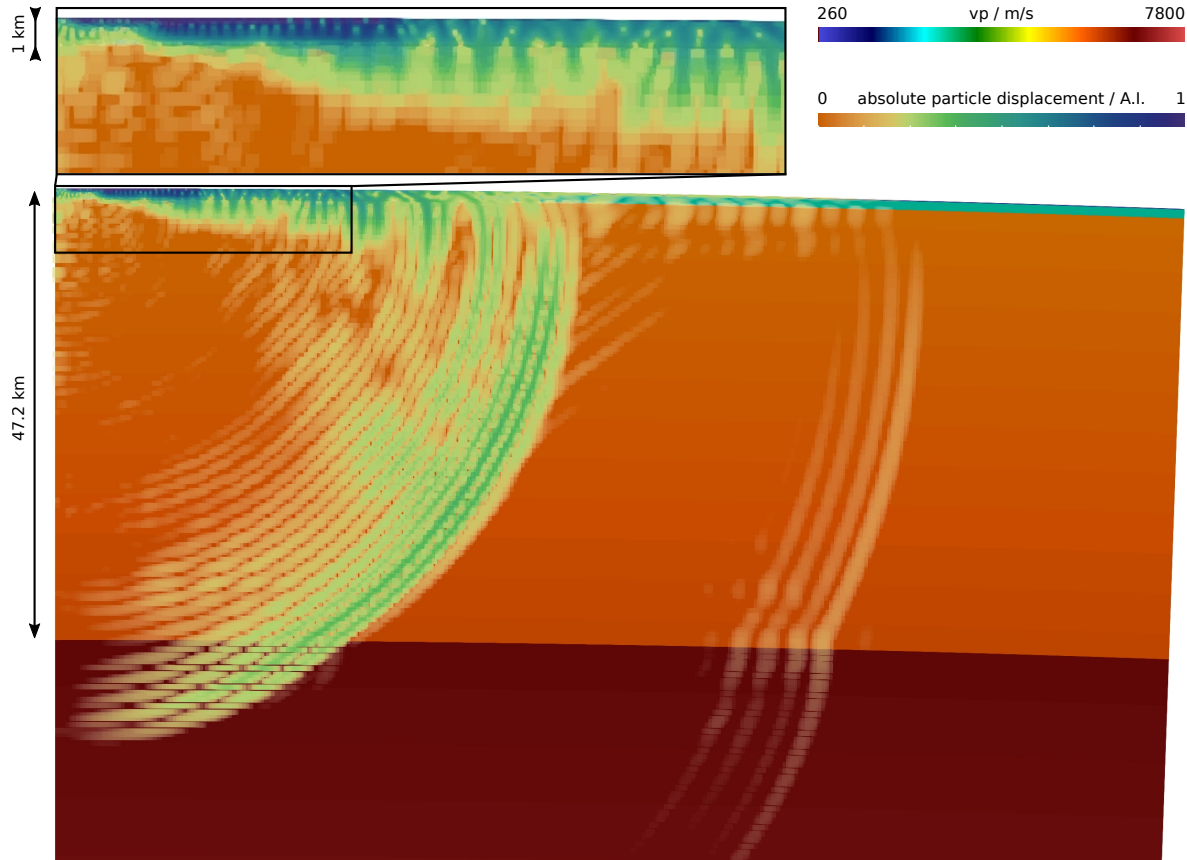
764

765 ***Influence on seismic amplitudes***

766

767 As noted in Section 3.1 and in Table 1, all source models generate seismic amplitudes that are
768 proportional to the inverse of the seismic velocities where the source associated with the impact
769 is released. This amplification effect due to the regolith is essential in the modeling of the

770 amplitudes of the waves. In addition, the regolith will trap seismic waves (Fig. 10). This trapping
771 will not only generate shallow layer surface waves, but also a ringing/reverberation effect of the
772 direct body waves.
773
774



775
776 **Figure 10:**
777 *Wavefield simulation for a short period of 1 Hz for a vertical impact in a 1D model with regolith*
778 *(80 m, $v_p=265-600$ m/s), bedrock (1 km, $v_p=2700$ m/s) and a crustal layer (47.2 km, $v_p=5400-$*
779 *5730 m/s). The color scale in the background indicates the p-wave velocity; the color scale in the*
780 *foreground the absolute particle displacement. The shallow layers lead to complex waveforms in*
781 *the body waves due to reverberation, and they trap energy due to total reflection acting as a*
782 *wave guide. Furthermore, large amplitude short period surface waves with very low phase*
783 *velocities are excited, though these can be considered an artifact due to the unrealistic*
784 *homogeneity in the shallow layers.*

785

786

787 ***Influence on seismic efficiency***

788

789 The large variation in empirical estimates of seismic efficiency k is likely to be partially
790 attributable to differences in surface and subsurface material properties. However, the variability
791 in scale, source, and material type makes it difficult to isolate the influence of specific material
792 properties. A notable exception is the influence of porosity and water saturation on k , which were
793 investigated numerically by Guldemeister and Wnnemann (2017). Compaction of dry and wet

794 porosity close to the impact site absorbs energy from the shock wave, reducing the energy
 795 available to be radiated as seismic waves. Numerical simulations of 12-mm diameter iron
 796 impactors striking sandstone targets of various degrees of porosity and water saturation at 4.6
 797 km/s showed a factor of two reduction in seismic efficiency when porosity was increased from 0
 798 to 40%. An order of magnitude reduction in efficiency was seen when the pore space was filled
 799 with water. The rather modest reduction in k with dry porosity may have been influenced by the
 800 model assumption that the shear strength of the sandstone targets was independent of porosity. A
 801 decrease in strength with increasing porosity would likely amplify the observed reduction in k ,
 802 and may explain, in part, the low seismic efficiency inferred from impacts in the porous lunar
 803 regolith (Latham et al., 1970b). We expect the InSight region to be covered in fractured regolith,
 804 but not as porous as the upper layers of the Moon.

805

806 3.6 SEISMIC SIGNALS FROM AIRBURSTS AND ASSOCIATED SEISMIC SOURCE

807

808 If an impactor's mass is comparable to or smaller than the mass of atmosphere it encounters, it
 809 will decelerate, ablate and potentially disrupt. This process rapidly transfers a large proportion, if
 810 not all, the impactor's kinetic energy to the atmosphere, producing a so-called airburst. Airbursts
 811 release the impactor energy into heat and therefore atmospheric over-pressure with a much larger
 812 efficiency than the seismic efficiency discussed in section 3.3. From Sedov shock wave theory
 813 (Landau & Lifshitz, 1982) and for the Shoemaker-Levy 9 impact on Jupiter, Lognonné et al
 814 (1994) estimated the seismic efficiency of an impact releasing its thermal energy in the
 815 atmosphere as larger than $(\gamma-1)$, where γ is the adiabatic index. For high temperature CO₂, this
 816 produces a seismic moment of more than 0.2 times the impactor energy, and therefore several
 817 orders of magnitude larger than the one associated with the ratio between seismic moment and
 818 energy. For v_p , this is equal to $2v_p S v$ for the GL model described in section 3.2, where v_p , v and S
 819 are the P wave's velocity, impactor velocity, and ejecta amplification, respectively. However,
 820 only a fraction of the airburst is converted to coupled seismic waves, with transmission
 821 coefficient $C = \frac{2\rho c}{\rho c + \rho_g v_p}$ (see section 3.3). For body waves, the ratio between the amplitude of
 822 the seismic waves excited by the impact on the surface and by the airburst near the surface can
 823 then be estimated as:

824

$$825 \frac{\frac{(\gamma-1)mv^2}{4\pi\rho c^3} T}{\frac{Smv}{4\pi\rho_g v_p^2}} = \frac{(\gamma-1)}{2S} \frac{v}{v_p} \frac{\rho_g v_p^3}{\rho c^3} T = \frac{(\gamma-1)}{S} \frac{v_p v}{c^2}. \quad (12)$$

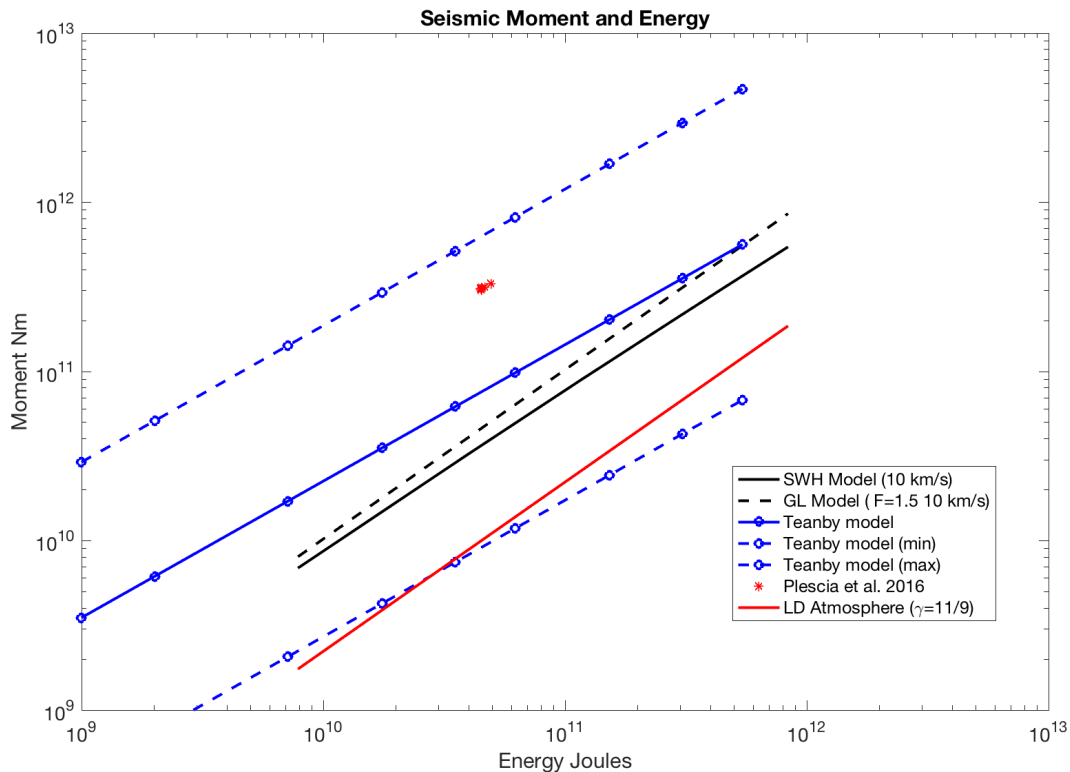
826

827 With v_p 2-3 times larger than the sound speed and an impact velocity of Mach 40 (~14 km/s),
 828 this leads to a ratio larger than 10. The amplitudes of seismic waves generated by the airburst as
 829 seismic sources are expected to be at least one order of magnitude larger than those of the
 830 surface impact itself, leading to ~10x as many detections of these phases, as proposed in section
 831 4.5.

832

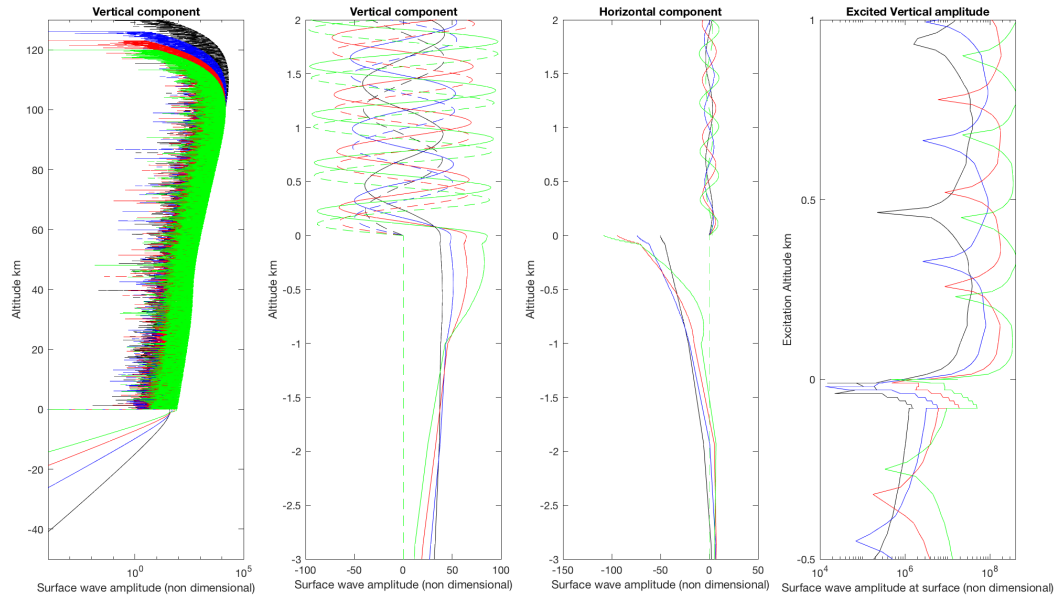
833 The same is valid for surface waves. This can be shown by comparing the excitation processes
 834 for seismic moment release either below or above the surface. Figure 11 compares these
 835 moments for the different approaches described in sections 3.1-3.2 and compares them to the
 836 moment, as estimated by Lognonné et al (1994) for atmospheric release. This suggests the latter

837 is smaller than those of the SWH and GL by a factor of 2 to 4, respectively. On the other hand,
 838 the amplitudes of surface waves for a pressure glut source associated with an explosion will be
 839 proportional to $u_\ell(r_0) \text{div}(\vec{u}_\ell(r_s))$ where r_0 is the radius/altitude measured at the surface, r_s the
 840 radius/altitude of the source, div the divergence operator, \vec{u}_ℓ the vector displacement field of
 841 surface wave mode of angular order ℓ , and u_ℓ the vertical component. Figure 12 shows the
 842 amplitude of the fundamental Rayleigh mode ${}_0S_{2000}$, ${}_0S_{3000}$, ${}_0S_{4000}$ and ${}_0S_{5000}$, with periods of 4.08
 843 sec, 2.87 sec, 2.28 sec, and 1.95 sec, respectively, as well as the excitation amplitude for a
 844 seismic moment located at a given altitude, either in the solid planet or atmosphere. The seismic
 845 model used is EH45TcoldCrust1 (Rivoldini et al. 2011) with a regolith layer and is described
 846 with more detail by Smrekar et al. (this issue), while the acoustic model is the LD model
 847 described by Lognonné et al. (2016), together with the viscosity and molecular relaxation model
 848 described above. Computations of normal modes are made following Lognonné et al. (1998) and
 849 detailed in Lognonné et al. (2016) for Martian air-coupled Rayleigh waves and modes. Due to
 850 the almost free surface boundary condition, a large drop of the amplitude divergence is observed
 851 at the surface. For the same moment release, the near-surface atmospheric pressure glut
 852 associated with airbursts can be 25-100 (at 4 sec) to 10 (at 2 sec) times larger, depending on the
 853 frequency and altitude. This makes the excitation of surface waves by airbursts in some cases
 854 more effective than moment release in the subsurface.
 855



856
 857 **Figure 11:**
 858 *Comparison of the relation between Seismic Moment and released energy for the Teanby (blue*
 859 *lines), Shishkin-Werth and Herbst (SWH) (black solid line), and Gudkova-Lognonné (GL) (black*
 860 *dashed line) models for release in the subsurface, and Lognonné-Dahlen (LD) model (red solid*
 861 *line) for release in the atmosphere. See text for details of models. For all models based on*

862 *moment release, the atmospheric moment (red) is expected to be 2-4 smaller than the solid*
 863 *moment (black and blue). The bedrock correction is made with relations (10) and (11) of section*
 864 *3.4 with the same densities and velocities as for Fig. 6.*
 865



866
 867
 868 **Figure 12:**
 869 *Amplitude of the fundamental Rayleigh mode ${}_0S_{2000}$, ${}_0S_{3000}$, ${}_0S_{4000}$ and ${}_0S_{5000}$, with periods of 4.08*
 870 *sec, 2.87 sec, 2.28 sec, and 1.95 sec, respectively, in black, blue, red and green. Solid lines are*
 871 *the real part, while dashed lines are the imaginary parts of the normal mode eigenfunctions. (a)*
 872 *shows the amplitude of the vertical component from a depth of 50 km (depths are negative on the*
 873 *y axis) to an altitude of 130 km. Note the attenuation due to viscosity and molecular relaxation,*
 874 *occurring only at an altitude of ~ 100 km. (b) is the real and imaginary part of normal modes*
 875 *close to the surface. Note the quadrature structure of the real and imaginary components of the*
 876 *vertical component, showing the upward propagative aspects of the normal modes, as well as the*
 877 *continuity of displacement near the surface. (c) is the same as (b) for horizontal components. (d)*
 878 *is the amplitude of a mode at the surface of Mars, when the moment release is made at a given*
 879 *altitude. Note that at 4 sec, the amplitude for a release at 250 m altitude is larger by a factor of*
 880 *25 than if the same moment is released at 80 m depth.*

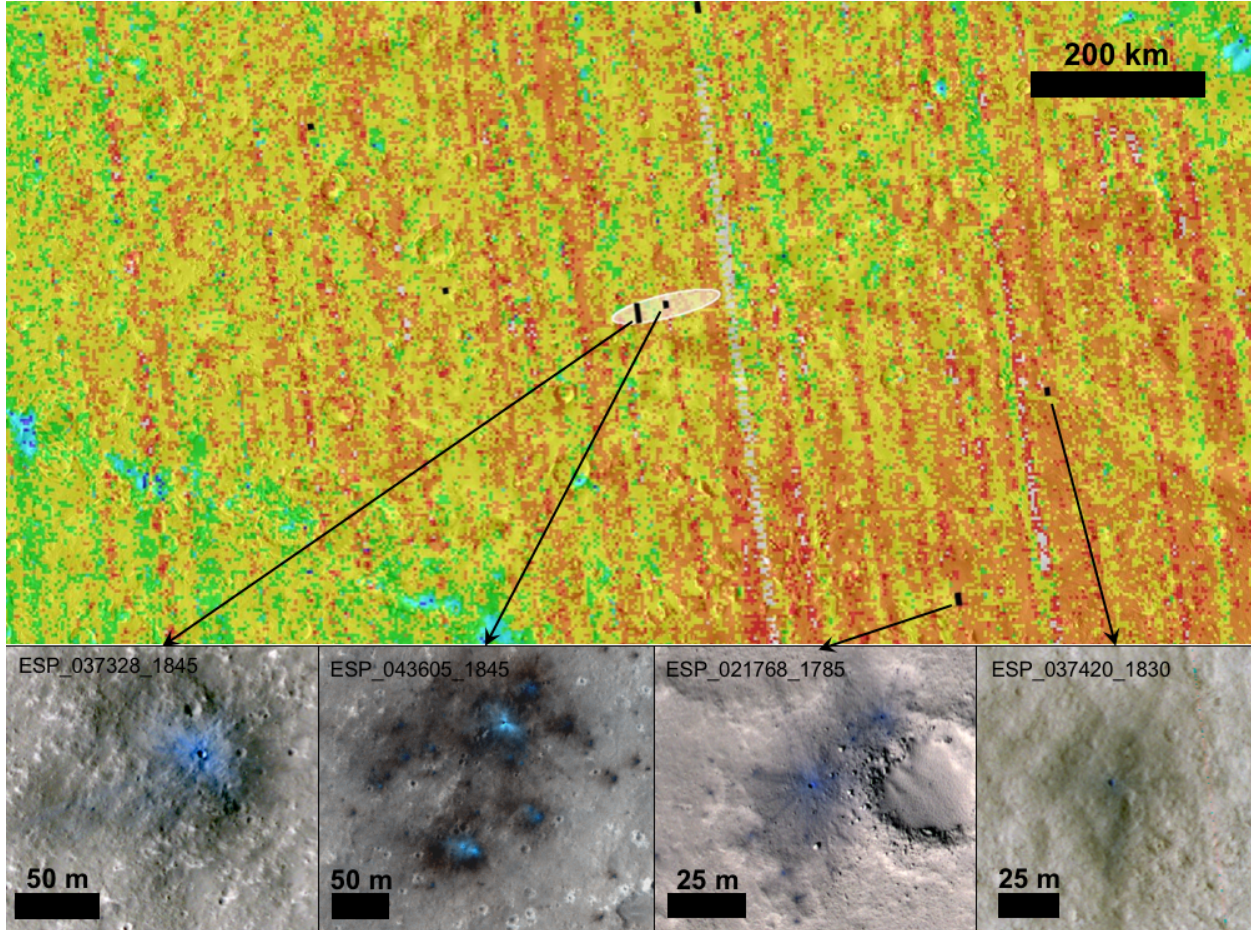
881
 882
 883 **4 IMPACTS ON MARS**

884
 885 **4.1 CURRENT MARTIAN IMPACT FLUX**

886
 887 Predictions of the Martian impact rate are based on lunar crater densities, which have been tied
 888 to absolute ages with radiometric ages of returned samples (e.g. Hartmann, 1966; 1977; 2005;
 889 Neukum and Wise, 1976; Neukum and Ivanov, 1994; Ivanov, 2001). The calibrated lunar impact
 890 flux can then be extrapolated to Mars, taking into account estimates of the effects of the different

891 impacting populations (size distribution and velocities of impactors), differing gravity that
892 affects the final crater size for a given impactor, and atmospheric blocking at Mars. Until
893 recently our understanding of the current Martian impact flux depended largely on the
894 Mars/Moon cratering ratio, a value which was merely estimated based on these models.

895
896 Starting in the last decade with long-lived, high-resolution orbital imaging, new impacts have
897 been detected appearing between successive images of the same area (Malin et al., 2006; Daubar
898 et al., 2013). Using this technique, several hundred new, dated impacts have been discovered on
899 Mars, several of which are very close to the InSight landing site (Daubar et al., 2015; Fig. 13).
900



901
902 **Figure 13:**
903 *Several new, dated impact craters discovered close to the InSight landing site. The final*
904 *reference landing ellipse is shown in white (4.5°N, 135.9°E) (Golombek et al., 2017). HiRISE*
905 *footprints containing new impact sites dated by before and after images are shown in black.*
906 *Basemap is the THEMIS Day IR 100 m global mosaic v.11.5 (Edwards et al. 2011) overlain with*
907 *the TES Dust Cover Index (Ruff and Christensen 2002), where red is high dust cover and blue is*
908 *low; lower dust cover to the southwest is likely contributing to fewer craters being found there.*
909 *HiRISE cutouts are from enhanced false color RDR products with North up; HiRISE images*
910 *credit NASA/JPL/University of Arizona.*
911

912 The before- and after-imaging technique measures an impact rate of 1.65×10^{-6} craters/km²/yr
913 with an effective diameter ≥ 3.9 m (Daubar et al., 2013). Below this size, a drop-off in the
914 impact rate is seen, which could be due to resolution effects, atmospheric filtering, observational
915 biases, or other factors.

916
917 In general, this technique allows for a direct measurement of the current impact rate at Mars.
918 However, that measurement is biased by the limitations of imaging, such as spatial resolution
919 and coverage. For these new impacts, there is also a detection bias that allows for discovery of
920 new impacts only when there is a strong albedo contrast in an impact blast zone many times
921 larger than the crater itself (Daubar et al., 2013). Fading of those low-albedo blast zones may
922 also contribute to lack of small crater detections (Daubar et al., 2016). A seismic measurement of
923 the current impact rate would be free of such biases, although there will be different biases in
924 such a measurement, as discussed in Section 8.4. Lognonné et al. (2009) made such a
925 measurement for current lunar impacts, and the seismically determined impact flux on the Moon
926 was found to be within $\pm 50\%$ of that at the top of the Earth's atmosphere.

927

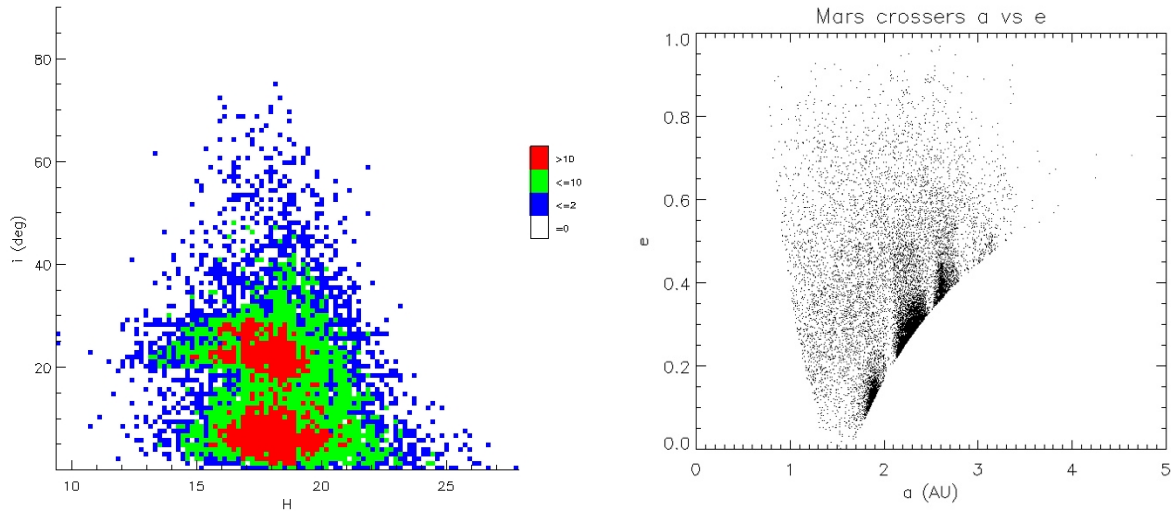
928 **4.2 MARTIAN IMPACTOR CHARACTERISTICS**

929

930 The impactors responsible for forming these new dated craters are presumably represented by the
931 population of Mars-crossing objects (MCOs). This group of objects was studied in the past
932 (JeongAhn & Malhotra, 2015 and references therein) by selecting a subset of known asteroids
933 from the Minor Planet Center orbital catalog¹. This set of MCOs was chosen to be those with
934 $Q > q_{\text{Mars}}$ and $q < Q_{\text{Mars}}$ (where q is the perihelion distance, and Q is the aphelion distance).
935 Additionally, the selection was limited to objects that have been observed for more than one
936 opposition. This leads to a population of 13,355 MCOs, whose orbital distribution is shown in
937 Fig. 14. Note that if we include the MCOs that have been observed during one opposition only,
938 the total number of MCOs increases to 31,207. That population has similar general trends as
939 the downselected population. The two populations highlighted by previous studies, below and
940 above $i=18^\circ$, are clearly visible in Fig. 14. The absolute magnitude distribution shows that most
941 of known MCOs are in the range 12-24 mag. Additional fainter MCOs are expected from future
942 surveys, such as LSST (Large Synoptic Survey Telescope; LSST 2018).

943

¹ <http://www.minorplanetcenter.org/iau/MPCORB/MPCORB.DAT>, download performed on Oct. 30th 2017



944

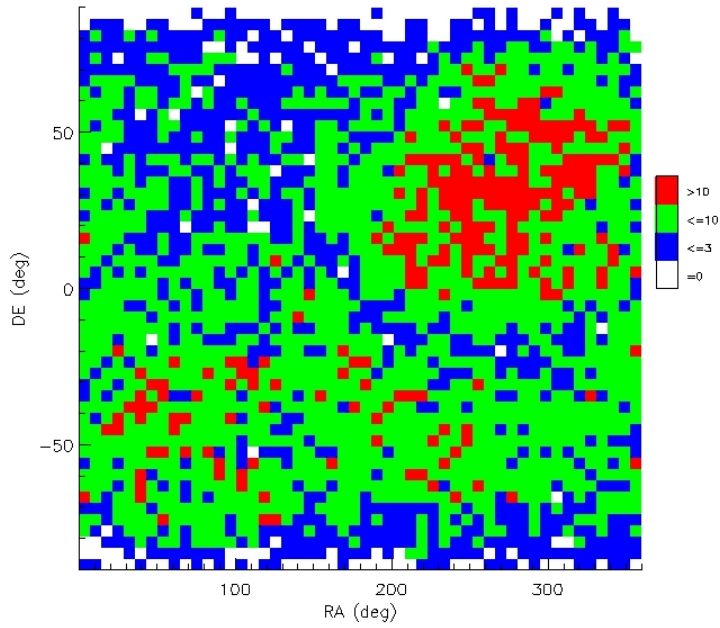
945 *Figure 14:*

946 *Left: Distribution of inclination (i) vs absolute magnitude (H) of the population of Mars-crossing*
 947 *object (MCOs), selecting based on perihelion and aphelion. Colors represent the number of*
 948 *objects with those values. Right: Semi-major axis (a) vs eccentricity (e) of the same population.*
 949 *Gaps caused by resonances with Jupiter near $a=2.06$, 2.5 , and 3.27 AU can be recognized.*

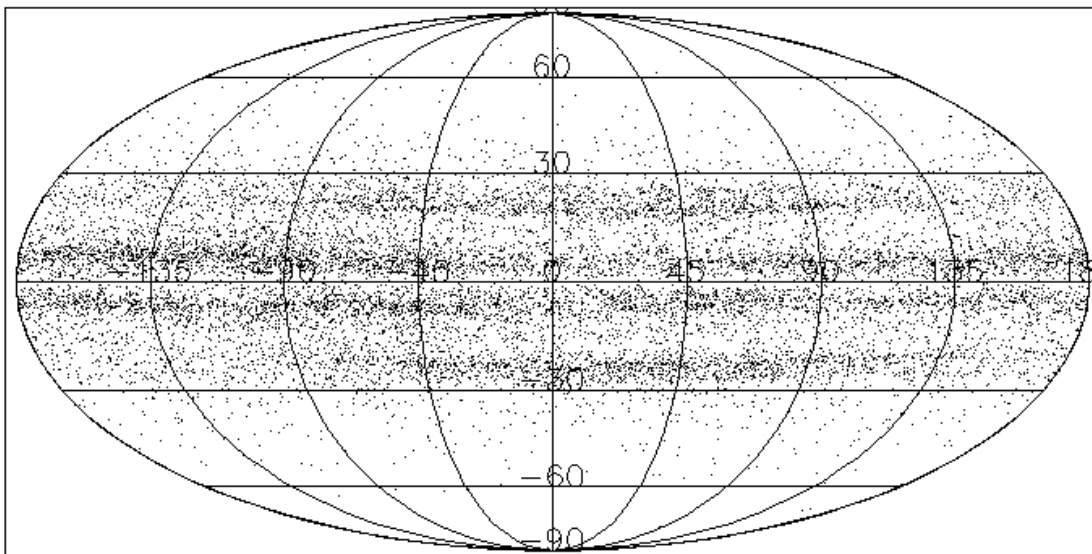
950

951 The impact velocities and directions of MCOs are computed using the Neslusan et al. (1998)
 952 method, the source code for which was kindly provided by the authors. We modified the code to
 953 apply it to Mars. The advantage of this method is that it not only computes relative velocities, but
 954 also the location of the radiant (position of the sky where the impacting MCOs seem to come
 955 from), as well as the Solar Longitude (L_S ; ecliptic Longitude + 180° ; a measure of Martian
 956 season) of the planet at the time of the closest approach. The distribution of the radiants and L_S
 957 are showed in Figs. 15 to 18.

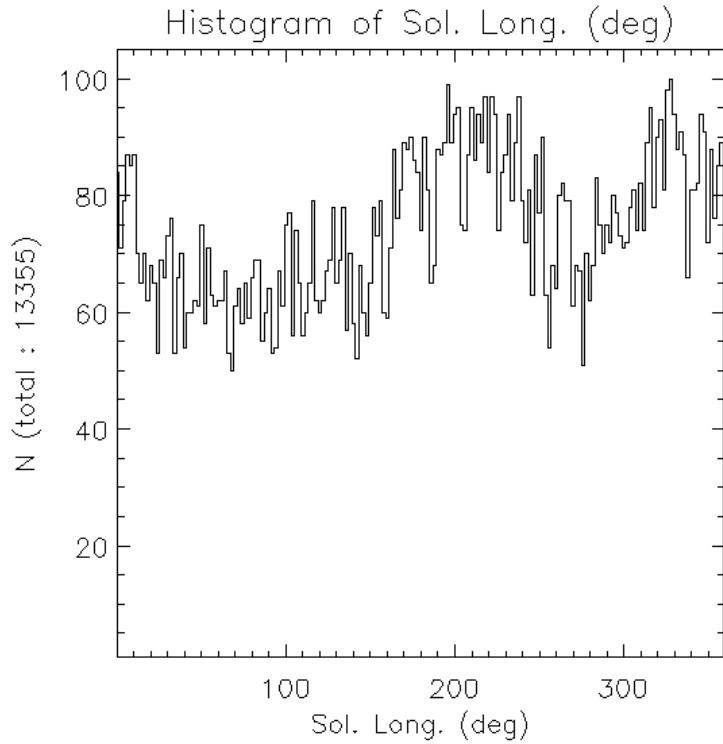
958



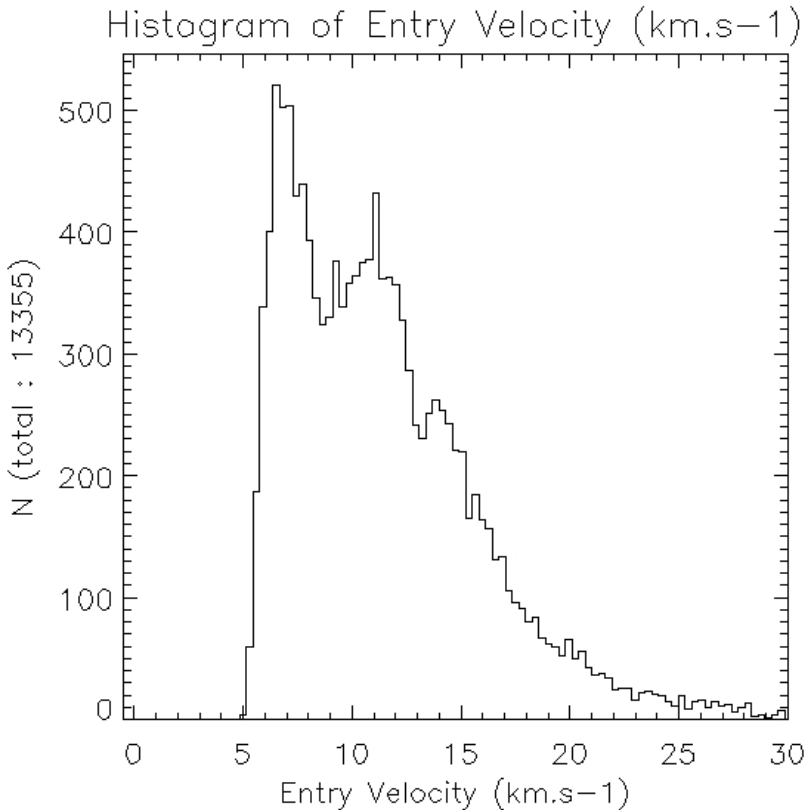
959 *Figure 15:*
 960 *Distribution of radiant of MCOs at Mars. RA: right ascension, DEC: declination (J2000). The*
 961 *colors represent the number of bodies with those parameters. A concentration of radiant can be*
 962 *recognized near RA~280°, DEC~30°.*
 963
 964
 965
 966



967 **Figure 16:**
 968 *The vector directions of relative velocities of MCOs as seen from Mars. The point at [0;0] is the*
 969 *Mars apex. The Sun is at [-90;0] and anti-Sun at [+90;0]. Bands can be recognized, as a*
 970 *consequence of low and high inclination populations.*
 971
 972
 973
 974



975 **Figure 17:**
 976 *Histogram of Mars Solar Longitude (L_S) at the time of closest encounter with each MCO. The*
 977 *maximum around $L_S=200^\circ$ is more pronounced if the criterion selection on the number of*
 978 *observed oppositions is relaxed.*
 979



980 *Figure 18:*
 981 *Distribution of the velocity of MCOs at the top of the Martian atmosphere. The median is located*
 982 *at 10.9 km/s and the mean at 11.7 km/s. Two peaks can be seen at ~6 km/s and ~11 km/s.*
 983

984 **4.3 MARTIAN CRATER MORPHOLOGY**

985
 986 Impact craters formed during the lifetime of the InSight mission are expected to be small (<100
 987 m) simple craters. These will be similar to primary craters formed on Mars during recent
 988 monitoring by spacecraft (Daubar et al., 2013; 2014). These simple craters are bowl-shaped
 989 depressions, with a breccia lens accumulated at the bottom of the crater, and a depth-diameter
 990 ratio of ~1:5 (Melosh, 1989; Daubar et al., 2014). New small Martian craters seldom have an
 991 appreciable raised rim (Daubar et al., 2014), perhaps due to impacting a more porous upper layer
 992 of the Martian crust. In most cases, any morphological complexity in craters of this scale
 993 originate from inhomogeneities in the target, such as variable strength, density or porosity (e.g.,
 994 Quaide and Oberbeck, 1968; Senft and Stewart, 2007). Features resulting from these
 995 inhomogeneities include irregular rims, flat floors, and “benches” or concentric craters (Daubar
 996 et al., 2014). At the InSight landing site, fresh rocky ejecta craters and nested craters indicate a
 997 fragmented regolith 3-17 m thick (Warner et al., 2017) and initial depth/diameter ratios about
 998 half that expected (Sweeney et al., 2016; Golombek et al., 2017), similar to other poorly
 999 consolidated targets on Mars (Watters et al., 2015).

1000
1001 Approximately half of such impacts form a single simple crater, while the other half form crater
1002 clusters, owing to the meteoroid fragmenting in the atmosphere before reaching the ground
1003 (Daubar et al., 2013). Given the prevalence of crater clusters, it is possible that a significant
1004 fraction of single craters also form by impact of a fragmented body, where fragments did not
1005 separate sufficiently to form separated craters (e.g., Miljkovic et al., 2013). The crater produced
1006 by such an impact would exhibit a shallower depth than if formed by a single consolidated
1007 impactor (Artemieva and Pierazzo, 2009). This could account for some of the variation in depths
1008 of newly formed craters on Mars (Daubar et al. 2014), if shallower craters were created by this
1009 process.

1010

1011 **4.4 MARTIAN CRATER SCALING**

1012

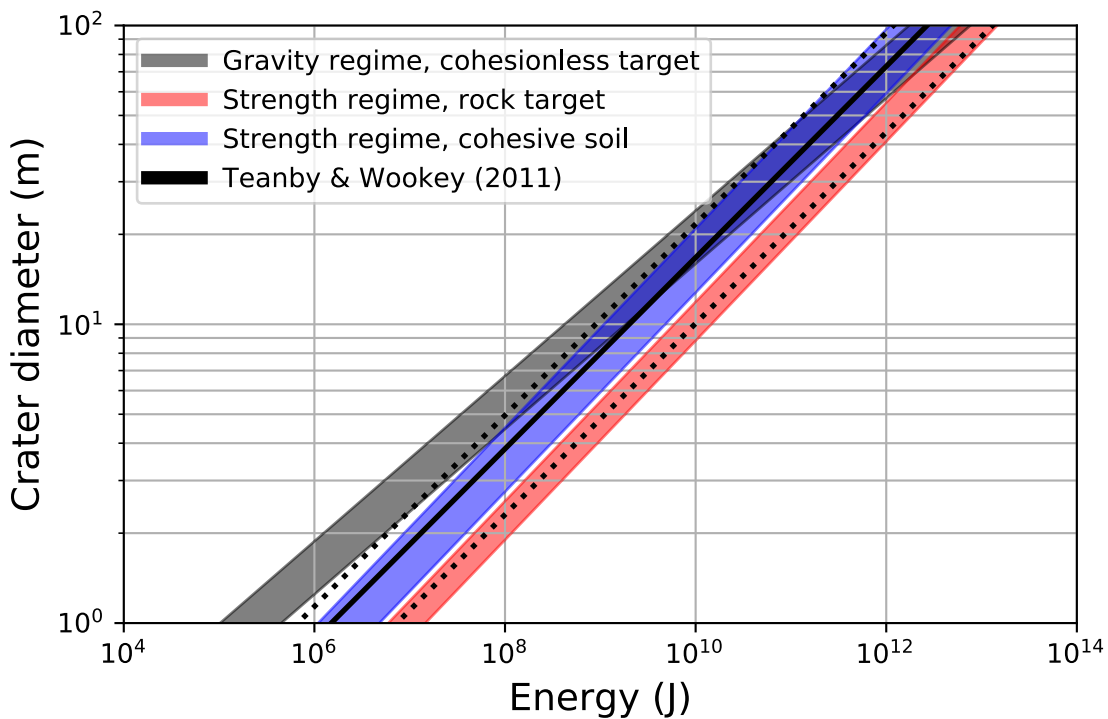
1013 To connect the impactor energy and the crater diameter produced, Teanby and Wookey (2011)
1014 proposed a simple scaling equation relating crater size to the kinetic energy of the impactor,
1015 based on large-scale impact and explosion experiments. This formulation has the advantage of
1016 directly linking the observed crater size to seismic energy through the seismic efficiency.
1017 However, laboratory impact experiments and numerical simulations have shown that crater
1018 diameter does not scale simply with impact energy (e.g., Schmidt and Housen, 1987; Holsapple
1019 1993; Wünnemann et al., 2011). The most widely-used and successful crater scaling approach,
1020 commonly known as pi-group scaling, instead relates crater size to a combination of impactor
1021 energy and momentum, known as the coupling parameter (Holsapple and Schmidt, 1987). The
1022 implication is that two impacts with the same kinetic energy but different combinations of
1023 impactor mass and velocity produce craters of different size. Moreover, the form of the scaling
1024 equation depends on the gravity, density, and cohesive strength of the target surface. In a
1025 cohesionless material, such as a dry granular regolith with negligible cohesion, crater size is
1026 limited by gravity; that is, the weight of the displaced material. In a cohesive soil or rock, on the
1027 other hand, crater size is limited by both gravity and the strength of the material. In small craters,
1028 strength is dominant and the effect of gravity can be ignored, but in larger impacts gravity begins
1029 to dominate and strength effects can be neglected.

1030

1031 Figure 19 compares the impact energy-crater diameter scaling equation proposed by Teanby and
1032 Wookey (2011) with pi-group crater scaling equations (Schmidt and Housen, 1987; Holsapple
1033 and Housen, 2007) for the range of crater size most likely to be observed during the InSight
1034 mission. Pi-group scaling results are shown for three target approximations: a cohesionless
1035 regolith-like target with a density of 1.5 g/cc and Martian gravity; a cohesive soil/regolith of the
1036 same density, but with a small cohesive strength of 100 kPa; and a dense (3 g/cc) rocky surface
1037 with a cohesive strength of 10 MPa. Gravity is neglected in the latter two scenarios. In kinetic
1038 energy-crater diameter space, the pi-group scaling equations for each target approximation plot
1039 as a line only for a specific combination of impactor density and velocity. We therefore show a
1040 band of possible outcomes, bounded above by a slow, dense impactor scenario defined as an iron
1041 impactor (7.9 g/cc) striking at Mars' escape velocity (5 km/s). This is bounded below by a fast,
1042 low-density impactor scenario defined as an icy impactor (1 g/cc) striking at 20 km/s. The
1043 analysis assumes vertical impact, neglects any deceleration during atmospheric entry, and
1044 accounts for a 30% difference between the crater diameter at the preimpact level and the final
1045 rim diameter (Holsapple, 1993).

1046
1047
1048
1049
1050
1051
1052
1053
1054
1055
1056
1057
1058

The comparison of scaling approximations illustrates that there is nearly a two order of magnitude range in impact energy required to produce a given crater size depending on the properties of the Martian surface and the density and speed of the impactor. The range of uncertainty reduces for larger craters or impacts known to be formed in regolith. Despite its simplicity, the energy scaling equation derived by Teanby and Wookey (2011) lies near the middle of the range of more conventional scaling approximations and the uncertainty attached to it is a good approximation of the variability in crater size scaling from anticipated variations in impactor and target properties. We also note that the pi-group scaling equations for cohesionless and cohesive soil/regolith intersect at a crater size of approximately 50 m, implying that the cohesive strength of the upper tens of meters of the Martian surface will have an important control on the size of craters likely to be formed during the InSight mission (<50 m).



1059
1060
1061
1062
1063
1064
1065
1066
1067
1068
1069
1070
1071

Figure 19.

Comparison of crater size scaling relationships for impact craters on Mars shown as a function of kinetic energy of the impactor. Pi-group crater scaling equations are shown as bands bounded above by a slow, dense impactor scenario and below by a fast, low-density impactor scenario. Bands are shown for three target surface approximations: a cohesionless regolith-like target with a density of 1.5 g/cc and Martian gravity (grey); a cohesive soil/regolith of the same density, but with a small cohesive strength of 100 kPa (blue); and a dense (3 g/cc) rocky surface with a cohesive strength of 10 MPa (red). Gravity is neglected in the latter two scenarios. Black lines show the impact energy-crater size scaling equation (dotted lines show minimum and maximum bounds) derived by Teanby and Wookey (2011).

4.5 FRAGMENTATION IN THE MARTIAN ATMOSPHERE

Unlike the Moon, Mars has enough of an atmosphere for it to be a factor when considering impacts and their seismic effects. When cometary or asteroidal material encounters a planetary atmosphere, aerodynamic resistance causes deceleration of the impacting body (meteoroid). If aerodynamic stresses are high enough, the meteoroid may experience ablation and/or fragmentation. Ablation occurs when sufficient heat is generated to vaporize or melt material from the surface of the meteoroid. In the thin Martian atmosphere ablation is near insignificant for all but very small meteoroids (sub-cm scale) entering at high speeds. Fragmentation is often assumed to occur when the stagnation pressure, $P = \rho_a v_m^2$, in front of the meteoroid is approximately equivalent to the meteoroid's bulk strength. Thus fragmentation is sensitive to entry velocity. After fragmentation, the effective surface area of the meteoroid increases as the fragments separate, dramatically increasing the rate of deceleration and energy loss to the atmosphere. Depending on the nature of fragmentation and rate of separation, such events can result in an airburst (a catastrophic disruption in the atmosphere) and/or near-simultaneous surface impact of a swarm of fragments to form a cluster or strewn field of craters. If fragmentation does not occur or occurs at very low altitude, the meteoroid will strike the ground as a basically coherent mass and form a single crater (e.g., Collins et al., 2005; Miljkovic et al., 2017).

In the absence of ablation and fragmentation, the deceleration of a single intact meteoroid is principally controlled by characteristics of the meteoroid (i.e. mass, shape, density) and its trajectory (i.e. velocity, angle of entry, atmospheric densities), and is well described by a simple drag equation (e.g. Baldwin and Sheaffer, 1971). However, the fate of the meteoroid after fragmentation is much more complex to analyze and depends on highly-variable meteoroid strength (Popova et al., 2011), style of fragmentation (catastrophic vs. progressive), and the interaction between fragments and wake behaviour (Passey and Melosh, 1980; Ivanov et al., 1997; Chyba et al., 1993; Hills and Goda, 1993; Register et al., 2017; Wheeler et al., 2017).

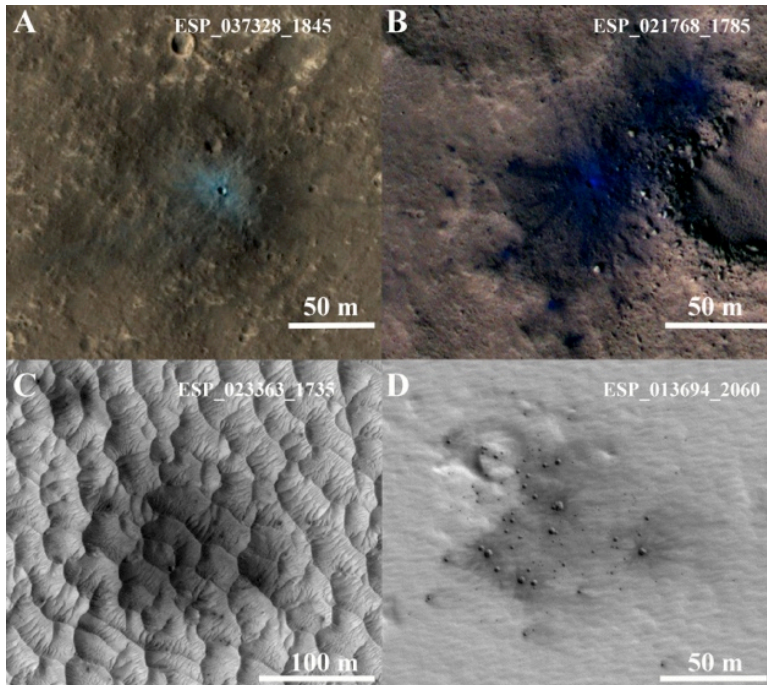
Of particular relevance to InSight is the fate of meter-scale meteoroids as seismic sources (Teanby and Wookey 2011; Stevanović et al. 2017). Forming decameter-scale craters, these are able to deliver the energy necessary for seismic detection (tens to hundreds of tons of TNT equivalent energy; 1 kton TNT = 4.185×10^{12} Joules), whilst also being frequent enough that several to tens of events are expected throughout the mission (Teanby and Wookey 2011; Teanby 2015; Stevanović et al. 2017; Section 6.2). Observations of recently formed craters on Mars reveals that approximately half of current impacts of this scale result in single craters, while the other half undergo fragmentation in the atmosphere and form crater clusters (Daubar et al. 2013; 2018). This proportion of fragmentation events suggests a median effective strength of approximately 1 MPa for meter-scale objects entering Mars' atmosphere, which is consistent with estimates of bulk meteoroid strength from terrestrial fireball observations (Popova et al., 2003; 2011), although a significant fraction of them seem to be weaker than this (Hartmann et al., 2017). For an approximately 1-m diameter ordinary chondrite meteoroid, a bulk strength of 1 MPa would imply a fragmentation threshold entry speed of 8 km/s, assuming a trajectory 45° from vertical at atmospheric entry. Meteoroids entering Mars's atmosphere between this speed and Mars's escape speed (5 km/s) would tend to remain intact, losing less than 5% of their initial speed prior to forming a single crater. Meteoroids entering at higher speeds on the same

1118 trajectory would fragment at altitudes up to 30 km for an entry speed of 30 km/s. The most likely
1119 entry speeds for Mars are evenly distributed around peaks at 6.5 km/s and 11.5 km/s (Le Feuvre
1120 and Wieczorek 2011; Fig. 18). A ~8 km/s breakup threshold, between these two peaks, is
1121 therefore roughly consistent with the near-equal numbers of single and clustered impacts
1122 observed by Daubar et al. (2013). However, the mass, momentum and kinetic energy of the
1123 fragments before they strike the ground is highly dependent on the assumed model of
1124 fragmentation. If fragmentation is catastrophic, no sizeable fragment may strike the ground, but
1125 the resulting airburst may still be able to deliver seismic and acoustic signals to the SEIS detector
1126 depending on its altitude and the rate of energy deposition in the atmosphere (Stevanović et al.,
1127 2017). Hence, three classes of impact-related seismic sources might be recorded by the SEIS
1128 instrument: (i) surface impact of a single mass (no fragmentation); (ii) near-simultaneous surface
1129 impact of a swarm of meteoroid fragments, separated by a few tens to hundreds of meters; and
1130 (iii) airburst caused by catastrophic disruption and rapid energy deposition in the atmosphere.
1131 The first of these, single impacts, is the canonical case discussed primarily in Section 3 on
1132 impacts in general, and is nominally assumed in the rest of the paper. In the next sections we
1133 discuss the physical processes and expected seismic signals from clustered impacts and airbursts.
1134

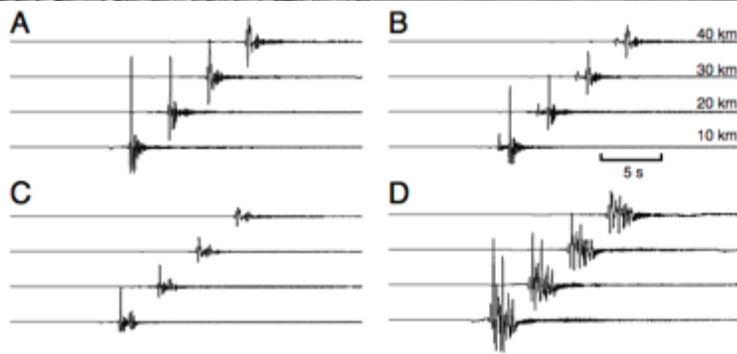
1135 **4.5.1 IMPACT CLUSTERS ON MARS**

1136

1137 The seismic source for a cluster would behave differently than a singular impact; the energy of
1138 the impacts will be distributed over a larger area, typically between 10-1,000 meters (Daubar et
1139 al., 2018). The source will be partitioned amongst craters of different sizes, and presumably
1140 bolides of various sizes. Schmerr et al. (2016) have built a seismological model for the predicted
1141 seismic signatures that would be recorded by seismometers deployed on Mars (Fig. 20). These
1142 source predictions are created using the measured crater properties from Daubar et al. (2018),
1143 along with a crater diameter scaling law for the strength regime (Holsapple and Housen, 2007)
1144 and momentum-driven source model after Gudkova et al. (2011, 2015) to relate the expected
1145 magnitude of the seismic source to the observed crater properties (See also Sections 3.1 and 4.4).
1146 The magnitude prediction is then combined with 3-D wave propagation modeling, using the
1147 Serpentine Wave Propagation Package (Peterson et al., 2010). The resulting theoretical Martian
1148 models are used to investigate the effect of a distributed source on the expected amplitudes of
1149 body and surface waves that will be essential for studying Martian internal structure.
1150



1151



1152

1153

Figure 20:

1154 *Examples of new, dated impact sites with various numbers of individual craters: A) single*

1155 *crater; B) 3 craters; C) 6 craters; D) >100 craters. HiRISE observation IDs are indicated on*

1156 *images. For all: North is up; sun is roughly to the west. A and B are from enhanced false color*

1157 *RDRs; C and D are from red RDRs. Lower panels show vertical component synthetic*

1158 *seismograms for these distributions of craters at various distances, using the model of Schmerr*

1159 *et al. (2016) and an impact force transfer source. Clustered impacts are spread artificially over*

1160 *2 seconds to simulate non-simultaneous impacts. This spread in time is longer than expected for*

1161 *most cases (should typically be «1 second; Daubar et al., 2018), but is used as an extreme upper*

1162 *bound here for comparative purposes. Note that background noise is not included in this model,*

1163 *so the overall detectability of these events cannot be inferred from these plots. Image credit:*

1164 *NASA/JPL/University of Arizona. (Banks et al., 2015; Schmerr et al., 2016)*

1165

1166 The resultant source time function was found to be dependent upon the total moment release of

1167 the multiple impacts, relative timing of impact events, and geographic closeness (dispersion) of

1168 the clustered impacts. It was found that clusters have smaller peak amplitudes and more short-

1169 period energy in their source spectra compared to single crater impacts. While more numerous

1170 smaller craters in clusters contribute insignificant energy to the source function, they add to the

1171 complexity of recorded seismic energies and produce a more diffuse seismic signal (Fig. 20).
1172 With such diffuse signals, it will be more difficult to identify P wave arrivals and thus will
1173 add uncertainty to the identification of source location. However, being able to differentiate
1174 between seismic signals from single crater impacts and the more diffuse and complex signals
1175 from crater clusters will allow us to predetermine some general characteristics of the impact and
1176 inform the orbital image search: what to look for and how detectable the impact will be in
1177 images. Overall, the seismic signal of more dispersed clusters will be less detectable than
1178 the impact of an intact bolide, and this will reduce the overall number of impacts InSight can
1179 expect to detect at Mars.

1180

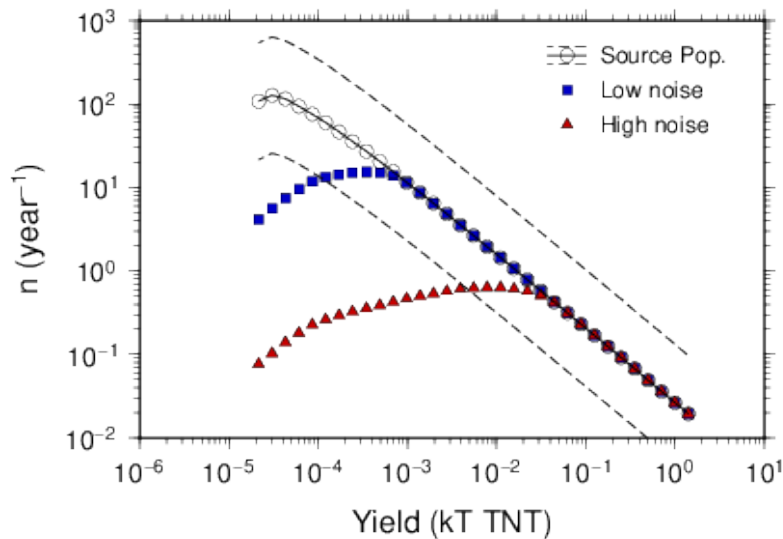
1181 **4.5.2 AIRBURSTS ON MARS**

1182

1183 On the far end of the fragmentation spectrum lie airbursts. Surface effects of martian airbursts
1184 have been observed in the form of thousands of small dust avalanches distributed asymmetrically
1185 around new dated craters (Burleigh et al., 2012). The number of airburst events that will be
1186 detected by InSight seismometers will depend on three main factors; the incident impactor
1187 population, the process of generating an airburst (which may be said in turn to depend on
1188 atmospheric and material properties), the Martian acoustic properties, and finally on the
1189 detection capability of SEIS.

1190

1191 The total overall incident bolide population at Mars is different from that at the Earth due to the
1192 proximity of the asteroid belt and Jupiter family comets. Other potentially impacting objects may
1193 be long-period comets sourced from the Oort cloud. By scaling the known size-frequency
1194 distribution (SFD) from Earth according to differences in impactor source population, planetary
1195 surface area and impact velocities, we can derive a flux SFD for Mars to be $\log_{10}(N) = a - b_{\oplus}$
1196 $\log_{10}E$, where N is the cumulative number of impactors per year incident on the Martian
1197 atmosphere of energy E and a and b_{\oplus} are empirically fitted constants (see Stevanović et al., 2017
1198 for more details). This can be compared to observed current cratering SFD on Mars to verify the
1199 relationship (Malin et al., 2006; Daubar et al., 2013). Fig. 21 shows the predicted airburst
1200 population on Mars along with predicted detection rates. Stevanović et al. (2017) predicted ~10-
1201 200 seismically detectable events, depending on the noise level of SEIS. This estimate contains
1202 an order of magnitude error resulting mainly from uncertainties in the air-ground coupling
1203 efficiency factor, atmospheric attenuation of the shockwave, amounts of seismic attenuation, and
1204 source population estimates. However, seismic signals from airbursts will allow detection of
1205 many more events than the generation of seismic waves by the impact to the surface alone.



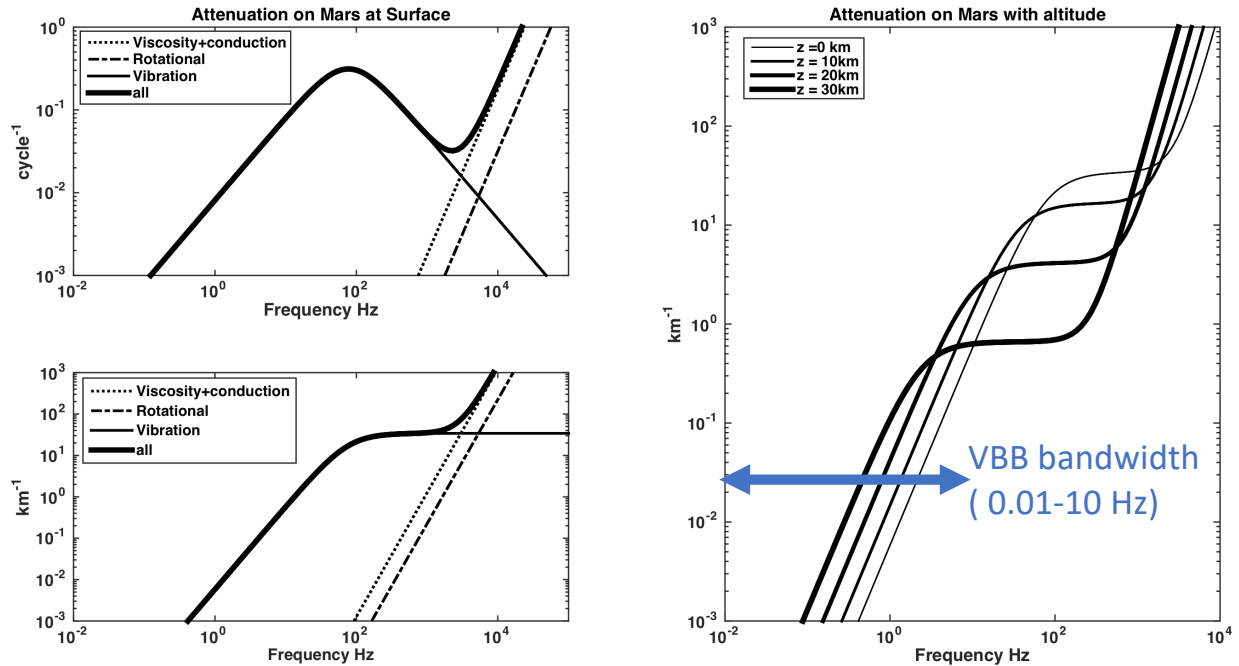
1206
1207
1208
1209
1210
1211
1212
1213
1214
1215
1216
1217

Figure 21:

Predicted airburst population and InSight detections. Based on observations of new impact craters by Daubar et al. (2013), Stevanović et al. (2017) estimated the number of events that would be seismically detectable to be 10 and 200 per year, integrated over the $\sqrt{2}$ incremental yield bins plotted here, for high and low noise cases respectively. This estimate contains an order of magnitude error, indicated by the dashed lines. Figure modified from Stevanović et al. (2017). Note that airbursts are only predicted to occur for yields between 2×10^{-5} –2 kiloTons TNT; larger events always penetrate the atmosphere and impact the surface, and smaller impactors are ablated or are slowed by drag to terminal velocity. Note these are based on the air-coupled seismic wave.

1218
1219
1220
1221
1222
1223
1224
1225
1226
1227
1228

Compared to Earth, very large differences in the acoustic attenuation occurs because of the CO₂ composition of the Martian atmosphere. As pointed out by Bass and Chamber (2001) and Williams (2001), molecular relaxation is the largest source of attenuation for infrasound waves at Mars. This is in contrast to Earth, where this attenuation source can be neglected. This results in very large attenuation, as illustrated by Fig. 22, which shows the attenuation factor of acoustic waves as a function of both altitude and frequency. The attenuation factor is defined as the inverse of the distance over which the amplitude decays by e . At 5 Hz, an attenuation factor of $\sim 1 \text{ km}^{-1}$ will likely prevent remote observations of acoustic waves. At 1 Hz, attenuation factors are $\sim 1/200 \text{ km}^{-1}$, thus these frequencies will have more potential for regional airburst detections. Short period surface waves (5-10 s) will be weakly attenuated further.



1229

1230

Figure 22:

1231 *Acoustic attenuation in the Martian atmosphere as a function of frequency. Left top: Attenuation*

1232 *per cycle. Left bottom: Attenuation factor in km^{-1} . Attenuation due to atmospheric viscosity and*

1233 *conduction (dotted line), molecular rotation (dashed line), molecular vibration (thin solid line),*

1234 *and the sum of all sources (thick solid line). This illustrates that molecular relaxation has a*

1235 *major effect in the upper part of the bandwidth of the APSS sensor (e.g. above 1 Hz) and is*

1236 *dominating attenuation; it causes almost 3 orders of magnitude more attenuation than*

1237 *atmospheric viscosity at these frequencies. Generally, from 1 Hz to 10 Hz the attenuation is*

1238 *significant, with attenuation lengths less than 100 km limiting likely detections of signals from*

1239 *purely atmospheric propagation to only those generated in the immediate region of the lander.*

1240 *Below 1 Hz, remote detection will be possible, as there is much less attenuation. Right: Total*

1241 *attenuation factors at different altitudes (shown with different line thickness), showing*

1242 *attenuation is ~ 20 times larger at 30 km than at the surface.*

1243

1244 The previously described modeling by [Stevanović et al. \(2017\)](#) shows that most airbursts occur

1245 at altitudes below 10 km. Therefore, the final airburst will occur close enough to the ground that

1246 acoustic waves incident on the surface will only be moderately affected by atmospheric

1247 attenuation before they are converted into seismic phases that will propagate through the

1248 planetary body to the seismometer. [Stevanović et al. \(2017\)](#) estimated this attenuation effect to

1249 be 0.7 for a moderate airburst and considered it negligible for the largest ones. Fig. 22 shows that

1250 this is likely a reasonable assumption, at least in the VBB bandwidth, assuming the shock cone

1251 of the airburst is smaller than 1 km, and the SEIS signal is recorded below 10 Hz.

1252

1253 These phases will travel much more quickly than the airwave, so they are likely to be observed

1254 as precursor phases of the acoustic waves described in Section 4.5.3. Importantly, they are likely

1255 to have larger amplitudes than the seismic waves excited by the direct impact on the surface. See

1256 section 6.2 for further discussion.

1257
1258
1259
1260
1261
1262
1263
1264
1265
1266
1267
1268
1269
1270
1271
1272
1273
1274
1275
1276
1277
1278
1279
1280
1281
1282
1283
1284
1285
1286
1287
1288
1289
1290
1291
1292
1293
1294
1295
1296
1297
1298
1299
1300
1301
1302

4.5.3 POTENTIAL FOR ACOUSTIC WAVE DETECTION FROM IMPACTS ON MARS

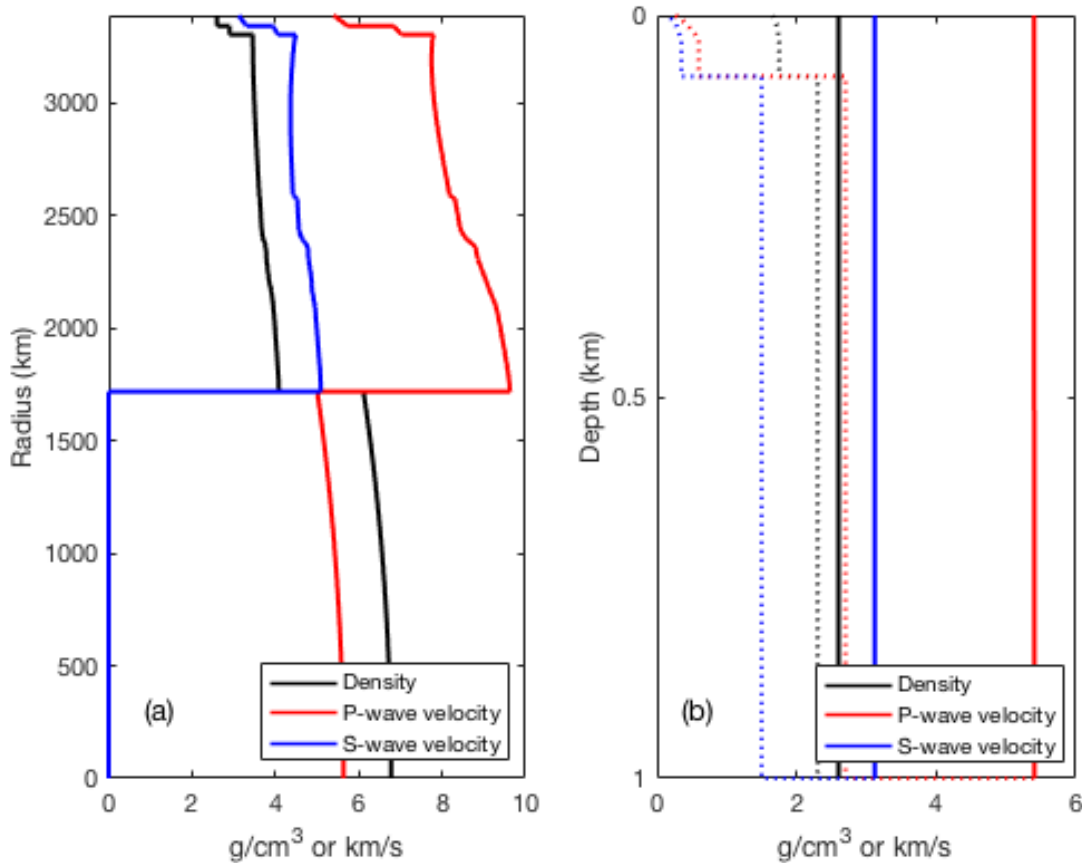
As described in this paper, many meteorite atmospheric entries will produce surface impacts generating acoustic waves at the impact site. In most cases, the continuous sound speed decrease with altitude in the Martian atmosphere will not allow these acoustic waves to propagate back to the surface. However, various wind jets in the atmosphere may duct back these waves in specific directions (Garcia et al., 2017). Moreover, during the night, the surface temperature gradient generates a wave guide close to the surface that may allow detection of these acoustic signals far from the impact source (Garcia et al., 2017). The acoustic waves created by seismic waves following the impacts will also face similar propagation constraints. In addition, their amplitude is predicted to be much smaller than the acoustic waves created by the explosion, due to the large impedance contrast between the Martian ground and atmosphere (Lognonné et al., 2016). In the absence of positive identification of an impact (see section 7.2), it will be challenging to definitively identify these signals as acoustic waves associated with an impact. InSight team members and associates are hopeful that direct acoustic signals from impacts will be detectable by the pressure sensor, if they are large enough and in band for the sensor, once the background noise level of the APSS sensors have been characterized.

5 BENCHMARKING IMPACT SEISMIC WAVEFORMS

5.1 COMPARING MODELS OF SYNTHETIC SEISMOGRAMS

We performed a benchmarking study of different codes being used by members of the InSight team to compute synthetic seismograms. The primary objective of this study was to compare the results of the various methods in the case of modeling meteor impacts on Mars. This comparison leads to a cross-validation of the techniques and a better understanding of their respective advantages, limitations, and weaknesses. Secondly, the synthetics provided for the benchmark can be used as a catalogue to estimate detection thresholds and characterize impacts as seismic sources.

To obtain comparable results, we selected one of the InSight interior structure reference models (Panning et al., 2017; Smrekar et al., 2018). This is a realistic one-dimensional model of the interior structure of Mars, the EH45TcoldCrust1 model (Rivoldini et al. 2011). The density and velocity profiles of the model are shown in Fig. 23a. In the case of impacts, which are seismic sources occurring at the very surface of the planet, it is of major importance to consider the shallow interior structure. For this reason, we also used a modified version of EH45TcoldCrust1 that differs from the original in the top 1 km. This modified model includes an 80 m-deep layer of regolith and unconsolidated material overlying fractured bedrock (Fig. 23b). The regolith layer is characterized by low density and low seismic velocities, which can significantly modify the waveforms and amplitudes of seismic signals. Attenuation is also taken into account: we use a quality coefficient (a quantity that describes energy loss due to attenuation) for shear waves of 600 in the crust and 143 in the mantle. Bulk attenuation is neglected. In the regolith layer the quality coefficient increases linearly with depth from 100 to 300 over the first 80 m, as proposed by Morgan et al. (2018).

1304
1305

1306

Figure 23:

1307 *Interior structure models used in the benchmark. (a) Density (black) and velocity profiles (red*
 1308 *and blue for P-wave and S-wave, respectively) of the EH45TcoldCrust1 model (Rivoldini et al.,*
 1309 *2011). (b) Zoom in on the upper 1 km of the EH45TcoldCrust1 model (solid lines) and the*
 1310 *modified version including fractured bedrock and regolith (dotted lines).*

1311

1312 Two different seismic sources were used. The first was an impulsive explosion at the surface,
 1313 described by a diagonal moment tensor with each component equal to 5×10^{10} Nm. The second
 1314 source was a vertical point force of 4×10^7 N applied at the surface. For both sources, a Dirac
 1315 delta function was assumed for the source time function. These sources were selected to be
 1316 representative of meteor impacts generating craters with diameters 25-40 m (Fig. 6). For both
 1317 sources, synthetic seismograms were computed at epicentral distances of 50, 100, 500 and 2000
 1318 km, with and without the regolith layer.

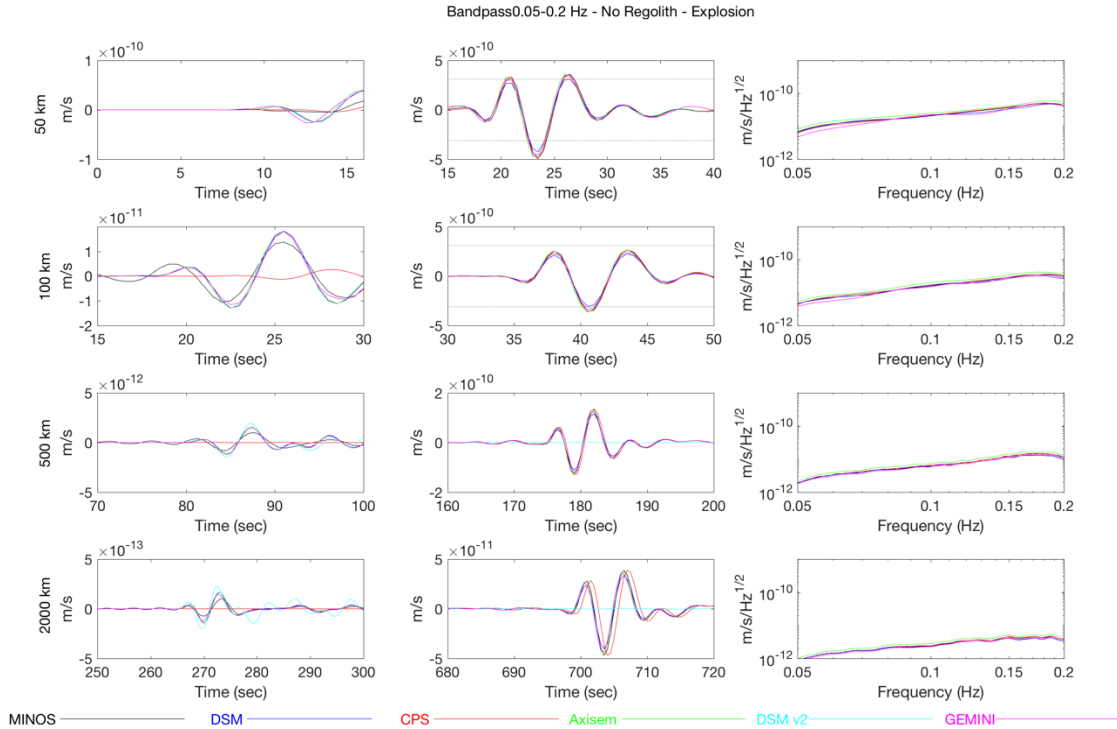
1319

1320 Here we briefly describe the different codes used in the benchmark; for details, see the respective
 1321 references. *Minos* is a normal-mode summation code based on the classical Mineos (Gilbert and
 1322 Dziewonski (1975), updated by Woodhouse (1988) and rewritten by Masters) and developed as
 1323 the 1D version of HOPT (Lognonné and Clévéde, 2002; Clévéde and Lognonné, 2003). *Direct*
 1324 *Solution Method (DSM)* is a technique used to compute synthetic seismograms (Geller and

1325 Ohminato, 1994; Geller and Takeuchi, 1995), recently adapted to the case of Mars. Two versions
1326 of the DSM code were used in the tests, which were independently modified for Mars. These
1327 codes are denoted by DSM and DSMv2. DSM requires computation of high-angular order
1328 coefficients even for low frequencies when we need to calculate the seismograms near the
1329 surface (e.g. Kawai et al., 2006). DSM automatically truncates the angular order by measuring
1330 the convergence of coefficients at the surface and is efficiently parallelized for this purpose, but
1331 with a 0.1 km depth source. DSMv2 manually fixes the angular order and puts the source at 23
1332 km depth. *Herrmann's Computer Programs in Seismology (CPS)*, Herrmann 2013) is a package
1333 for the computation of synthetics in a flat, layered planet. *AxiSEM* (Nissen-Mayer et al., 2014) is
1334 a spectral-element based method allowing the computation of seismograms for axisymmetric
1335 models. *GEMINI* is a numerical method to compute ground motion through integration of an
1336 appropriate system of ordinary differential equations (Friedrich and Dalkolmo, 1995).

1337
1338 Not all the methods, however, were used for all computations. This depends on the
1339 characteristics of each technique and of the targeted synthetics. In particular, DSMv2 was used
1340 only for the model without regolith and for epicentral distances of 500 km or larger. More
1341 precisely, due to limits on computational run time, the synthetics were generated with a
1342 maximum of 18000 radial grid points (~200 m spacing), which precluded resolving the 80 m
1343 regolith layer. In addition, convergence of the method was affected by the source depth, with
1344 shallower depths requiring computation to higher angular orders to reproduce the near field
1345 terms (see discussion in Kawai et al., 2006). For this reason, a source depth in the middle of the
1346 top layer was used (23 km depth) as a compromise. The far field body-wave wavefield is
1347 unaffected by this depth shift (see Teanby and Wookey, 2011), and the synthetics beyond about
1348 500 km converged. However, as a result of this non-zero depth the surface waves are not
1349 representative of an impact, and a small time lag correction is required. CPS, instead, was used
1350 only with modal summation, and therefore only surface waves were modeled. Although
1351 wavenumber integration can be used with this package, the required computation time would
1352 increase significantly. Finally, for the model with regolith, GEMINI exhibited numerical issues
1353 at short epicentral distances (50 and 100 km) with unphysical wraparound phases.

1354
1355



1356

1357 *Figure 24:*

1358 *Results of the benchmarking study for the explosive source and the original structure model*
 1359 *without regolith, using six different techniques as described in the text. In each row, from left to*
 1360 *right: zoom on the P-wave, zoom on the highest amplitude surface waves, and spectra. The rows*
 1361 *are at increasing epicentral distances of 50, 100, 500 and 2000 km. All seismic data are in*
 1362 *vertical velocity and bandpass filtered between 0.05 and 0.2 Hz. The root-mean square noise,*
 1363 *based on the InSight requirements, is represented by dashed lines whenever smaller than, or*
 1364 *comparable to, the signal.*

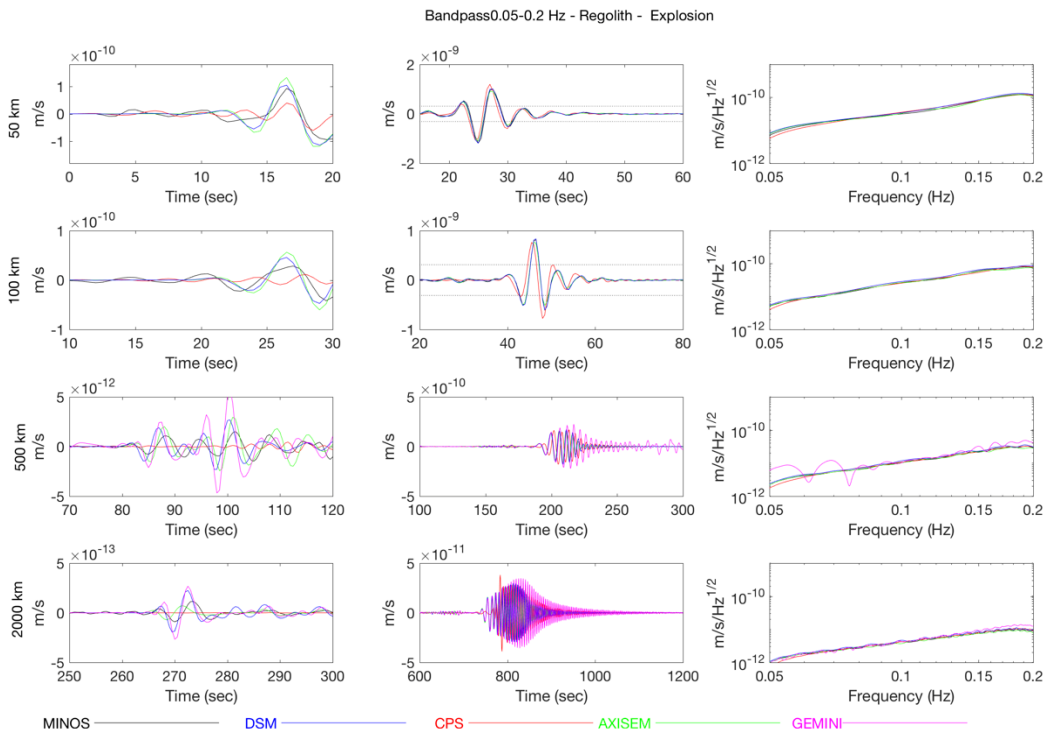
1365

1366 The results for the explosion source and the structure model without regolith are shown in Fig.
 1367 24. The synthetic seismograms represent vertical ground velocity and are bandpass filtered
 1368 between 0.05 and 0.2 Hz with a fifth-order Butterworth filter. Results for the radial component
 1369 are not shown, but they are similar to the vertical case. The codes give very similar results in
 1370 terms of amplitudes and waveforms at all epicentral distances, with a few exceptions. CPS was
 1371 used to compute surface waves only, so no P-wave arrival is present. Moreover, at large
 1372 epicentral distances (i.e. 2000 km) a time shift appears relative to the other models, which is due
 1373 to the equivalent flat planet used. As described above, DSMv2 used a source at depth and thus
 1374 surface waves are significantly smaller; also, a difference in the P-wave arrival is produced and
 1375 the synthetics were time-shifted by 3 s. Finally, the GEMINI synthetics needed to be scaled in
 1376 amplitude by a factor of two, which requires further investigation.

1377

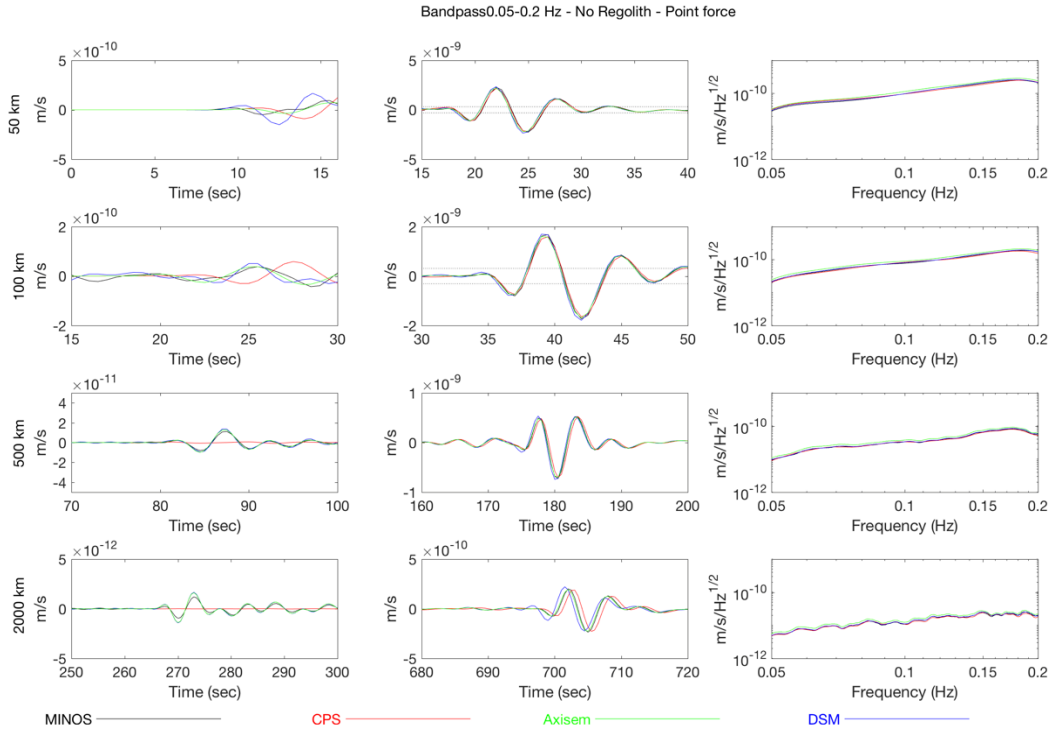
1378 For the structure with regolith, we can still observe good agreement between DSM and AxiSEM
 1379 compared to MINOS, which could have suffered from long-period noise before the first arrivals.
 1380 CPS uses Earth flattening, so it is not surprising to have phase delays at large distances. Another
 1381 observation on the comparison will be later phases calculated with Gemini. Since Gemini uses
 1382 the strong form of equation of motion, whereas DSM and AxiSEM use the weak form, the

1383 treatment of boundary conditions can be ad-hoc (c.f. Geller and Ohminato 1994; Komatitsch and
 1384 Vilotte 1998). This will cause accumulation of numerical errors at some conditions. If we look at
 1385 the frequency content, there are some significant discrepancies between Gemini and the pair of
 1386 DSM and AxiSEM at certain frequencies. We can explain this phenomenon by introducing
 1387 optimal accuracy of numerical operators: numerical errors in operators will result in a large error
 1388 only in the vicinity of the eigenfrequency of the mass and stiffness matrices, due to a zero
 1389 division of the error propagator of the operator to the resulting waveforms (e.g. Geller and
 1390 Takeuchi 1995).
 1391
 1392
 1393

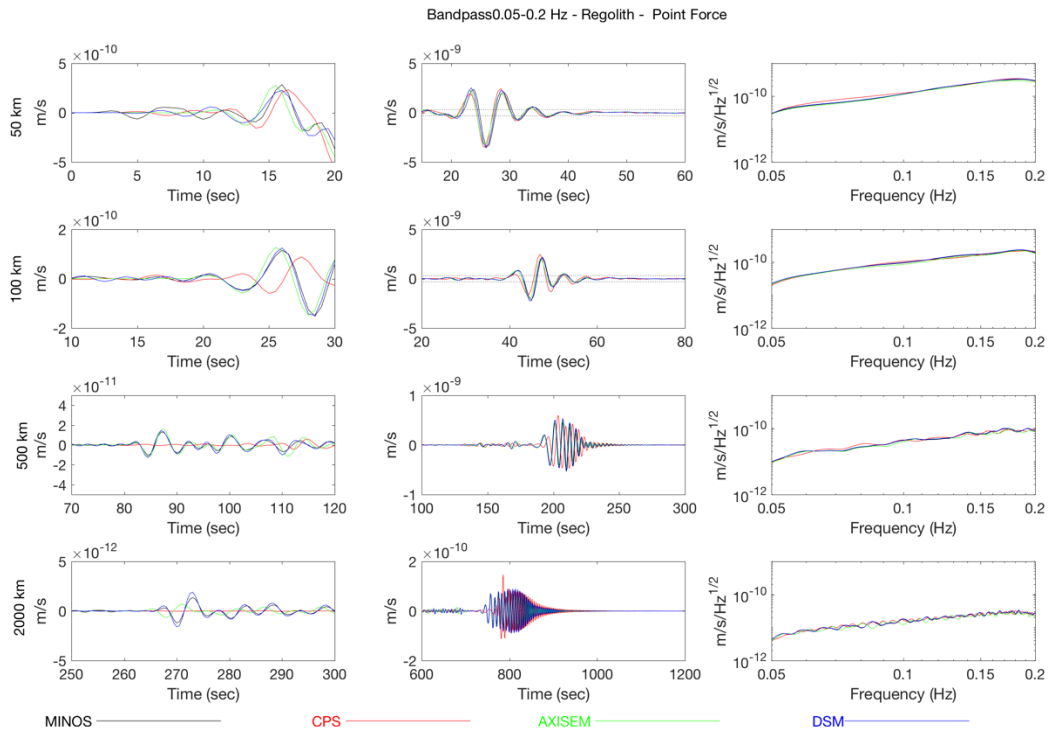


1394
 1395 **Figure 25:**
 1396 *Same as Fig. 24, using the modified structure model that includes a regolith layer.*
 1397

1398 For the structure model with regolith (Fig. 25), the agreement between the different techniques is
 1399 still good for surface waves, especially for epicentral distances below 2000 km. Body waves
 1400 instead exhibit larger differences between the methods, which show the difficulties of accounting
 1401 for this very-low velocity layer right below the surface. The fit for first P-wave arrivals (time and
 1402 amplitude) is, however, satisfactory. The case of the vertical point force gives analogous results
 1403 (Figs. 26 and 27 for the model without and with regolith, respectively).
 1404
 1405



1406
 1407 *Figure 26:*
 1408 *Same as Fig. 24, but for a vertical point force.*
 1409



1410
 1411 *Figure 27:*
 1412 *Same as Fig. 24, but for a vertical point force and the structure model including a regolith layer.*

1413 To summarize, this benchmarking study enables us to better understand the use of standard
1414 numerical methods to model the seismic signals generated by meteor impacts. In the simple
1415 example of a planet without regolith, all the techniques able to describe a surface source give
1416 very similar outputs up to 0.2 Hz in frequency. If this is interesting especially for surface waves,
1417 it should be noted that most of the body-wave energy is expected to be at higher frequency,
1418 above 1 Hz. When using CPS, a more careful correction for the flattened models should be taken
1419 into account to avoid a small time-shift at large epicentral distances. The more realistic case with
1420 regolith is more complicated: the decay of the signal and the body-wave reverberations are not
1421 reproduced in exactly the same way by the different codes. However, the maximum amplitudes
1422 of the signals, as well as their arrival times, compare well. In this respect, it is interesting to note
1423 that, for the same source, amplitudes are larger in this case: the detection of impacts on Mars will
1424 most likely be possible thanks to the regolith layer and its behavior in terms of seismic energy
1425 conversion (see Sections 3.1, 3.3 and 3.4 for more discussion).
1426

1427 **5.2 SEISMIC AMPLITUDE AS A FUNCTION OF DISTANCE**

1428
1429 The detectability of impacts on Mars is affected by the size of the source (source magnitude), the
1430 distance of the station from the source (geometric spreading), and the transmission properties of
1431 the Martian subsurface (intrinsic attenuation and seismic scattering). The seismic amplitudes
1432 from the impact itself are dependent upon the efficiency of momentum transfer in the impact,
1433 including the energy lost to damaging of the target materials, removal of ejecta, and heat, and
1434 efficiency of conversion of impact momentum into seismic ground motion (discussed in Section
1435 3.3). For a given size impact source, we can estimate the seismic amplitude as a function of the
1436 epicentral distance of the source using a 1-D wave propagation simulation.
1437

1438 These synthetic wave propagation simulations require the assumption of a background structure;
1439 here we assume Model-A of Sohl and Spohn (1997) updated with the model from Rivoldini et al.
1440 (2011) and add a simple 1-layer crust of 50 km thickness, with a S-wave velocity of 3200 m/s
1441 and P-wave velocity of 5000 m/s. We chose to keep this model simple as the details of the
1442 Martian interior are not yet constrained. We vary the attenuation structure within these models,
1443 assuming three background reference levels, high-Q ($Q=500$), intermediate ($Q=100$), and low-Q
1444 ($Q=50$) to investigate the effect of attenuation structure on wave propagation and detectability
1445 (Fig. 28).
1446

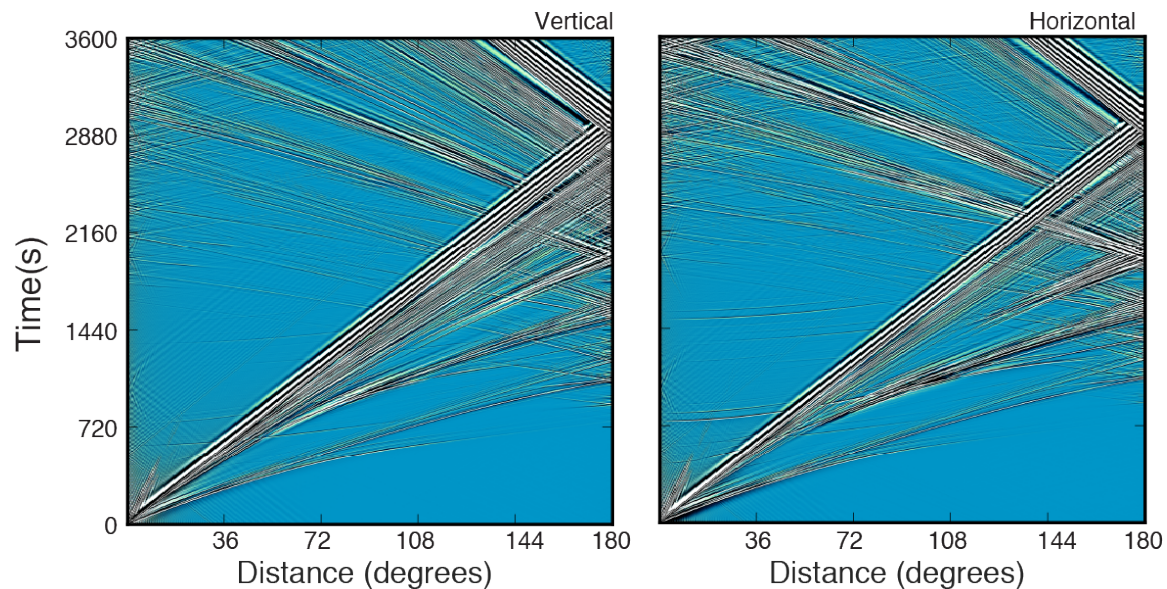
1447 The highest amplitude waves produced in a seismic event are typically the surface waves.
1448 Surface waves don't show up in the lunar data owing to the high degree of scattering in the lunar
1449 regolith and megaregolith (where they primarily propagate; see Section 2.2). Impact sources
1450 should generate Rayleigh waves through P-SV coupling (as demonstrated in the synthetics for an
1451 impact-like source), but not Love waves. The surface waves are quite susceptible to scattering
1452 and attenuation effects that are particularly strong near the surface, meaning they are lost more
1453 readily than the body waves that travel below the surface.
1454

1455 In our modeling, the highest amplitude waves produced by impacts are the surface waves. On
1456 Mars, it is an open issue how these surface waves will be affected by the scattering associated
1457 with crustal heterogeneities and impact-associated faults. If Mars is Moon-like, we can indeed
1458 expect the surface waves to be strongly affected by scattering and to have amplitudes

1459 significantly smaller than those modeled in 1D cases, as shown by modeling done by Gudkova et
1460 al. (2010). In addition to the poor long-period sensitivity of the Apollo seismometer when
1461 operating in the most used peaked mode, this led to no observations of surface waves on the
1462 Moon. On the other hand, observations of surface to near-surface explosions on the Earth allow
1463 the recording of both surface waves and body waves (e.g. Hedlin et al., 2002).

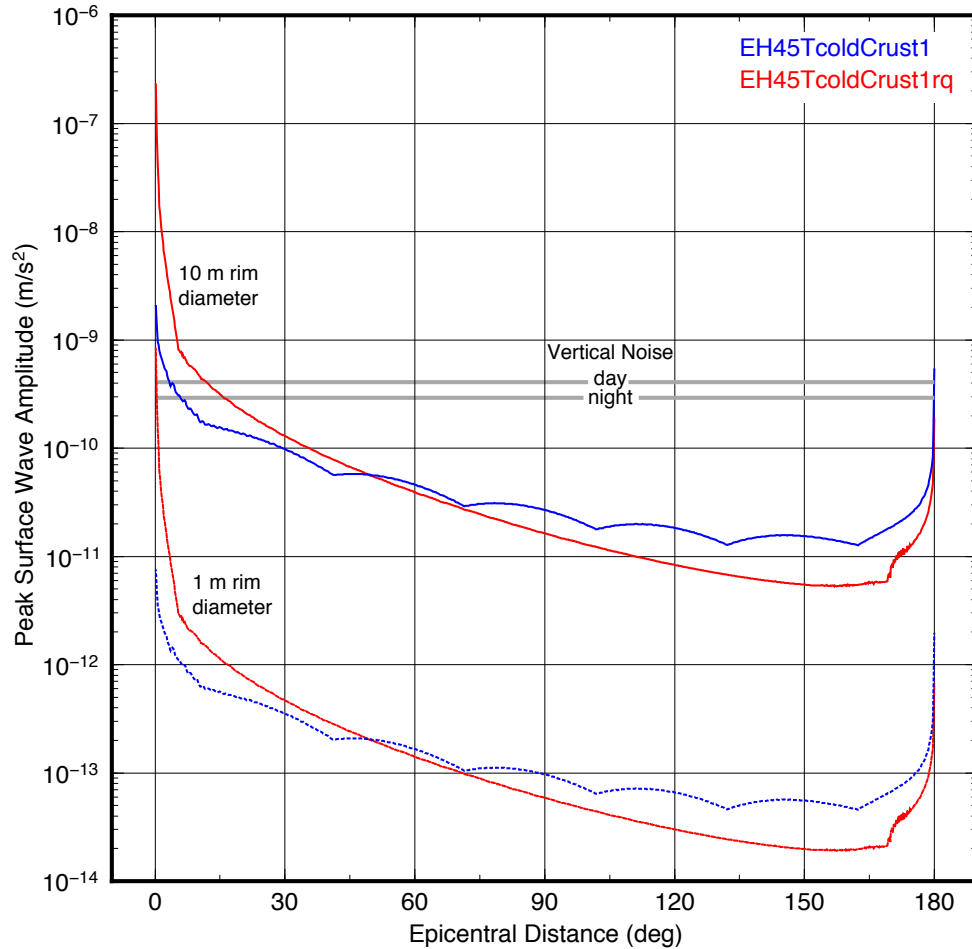
1464
1465 To determine the detectability of surface waves as a function of distance, we find their maximum
1466 amplitude occurring within one hour of the impact source. This is repeated for each epicentral
1467 distance and attenuation value. Here we assume a 10 m diameter crater-forming impact as our
1468 reference source. In the near vicinity of the impact, ground acceleration is high and decays
1469 rapidly with distance from the source. At high frequencies (1 Hz) this effect is large (Fig. 29)
1470 with 1 Hz waves falling below the expected overall noise level at 15° from the source for
1471 intermediate attenuation values ($Q=100$). At longer periods, the waves from a 10 m diameter
1472 crater should propagate globally with a relatively high signal to noise ratio. For this reference
1473 source, the amplitude is below the noise requirement for an epicentral distance of 15°, or ~900
1474 km. Within this distance from the landing site, we can expect reasonable homogeneities in the
1475 Martian crustal structure. The younger northern terrain, which might be less fractured than the
1476 lunar crust, might provide more Earth-like than Moon-like conditions for surface waves.
1477 Therefore surface wave detection from sources to the north may be more likely than on the
1478 Moon.

1479
1480



1481
1482 **Figure 28:**
1483 *1-D wave propagation simulation of impact energy propagating within the interior of Mars.*
1484 *Amplitudes are scaled to the peak ground motion in the time/distance window. Positive*
1485 *amplitudes are white, negative amplitudes black. Wave propagation is calculated using GEMINI*
1486 *(Friederich and Dalkolmo, 1995), scaled in amplitude to match the amplitudes found with all*
1487 *other benchmarked modeling techniques.*

1488
1489



1490

1491 *Figure 29:*

1492 *Estimated seismic amplitudes from impacts and the sensitivity of the InSight SEIS-VBB to*
 1493 *detecting waves generated for a seismic efficiency of 0.005 by A) a 10 m diameter crater*
 1494 *(moment= 1.922×10^{10} Nm), and B) 1 m diameter crater (moment= 5.801×10^7 Nm). Synthetics are*
 1495 *generated using GEMINI (Friederich and Dalkolmo, 1995), scaled in amplitude and corrected*
 1496 *from surface amplification as explained in the text, for a 0 km explosive moment tensor source.*
 1497 *The background models used are from Rivoldini et al., 2011 (described in Section 5.1). The*
 1498 *seismic moment is calculated for each crater size using the crater scaling of (Teauby and*
 1499 *Wookey, 2011) and corrected for regolith effects using a scaling factor of 18.2 (as defined in*
 1500 *Section 3.4, equations 10 and 11, with values from Section 3.2). Data are bandpass filtered from*
 1501 *0.2 to 0.05 Hz. We measure the peak amplitude of the Rayleigh wave using the first hour of the*
 1502 *simulated seismogram after applying the bandpass filter. The expected diurnal variation in the*
 1503 *SEIS-VBB noise floor for our frequency band is indicated in gray to indicate the detectability of*
 1504 *the impacts (Mimoun et al., 2017).*

1505

1506 **6 IMPACT DETECTIONS BY INSIGHT**

1507

1508 Recognizing impacts in the seismic data from InSight will be challenging at first. For one thing,
 1509 empirical seismic recordings from terrestrial and lunar impact events are limited (Section 2).
 1510 Another source of uncertainty is the largely unknown nature of the shallow and deep structure of

1511 Mars. With so many unknowns, we expect an exploratory period early in the mission, during
1512 which candidate possible impact signals will be identified based on various criteria. If several of
1513 these events can be confirmed to be impacts with orbital imaging of new craters (Section 7), the
1514 characteristics of impact-induced seismic signals will be better known, and identification and
1515 discrimination of these signals will become routine. Prior to data collection, we can plan on these
1516 various approaches to analyzing the data.

1517

1518 **6.1 SEISMIC DISCRIMINATORS OF IMPACTS**

1519

1520 Seismic signals from impacts differ in several important ways from interior, tectonic quake
1521 sources. An important feature of impacts is that they are exogenic, superficial events. This will
1522 be an important *a priori* constraint for the source location, as the depth is always near zero. Here
1523 we present several other features of seismic records such as this, which can be used to
1524 discriminate between tectonic and impact generated seismic events in the InSight SEIS data
1525 streams. This will no doubt evolve during the mission as our understanding of Mars and impact-
1526 generated seismic signals increases. To help with developing these impact diagnostics, we have
1527 drawn on the extensive work undertaken to monitor the nuclear test ban treaty. However, we
1528 note that most of the methods developed to discriminate nuclear explosions from earthquakes
1529 rely on a global network of seismometers, dense arrays, and infrasound detectors. With InSight,
1530 we will be limited to a single seismic station, necessitating a different strategy.

1531

1532 We have developed the following set of diagnostics that can be used to reject the hypothesis of
1533 an impact. These will be used in operations to reduce the number of candidate impact events for
1534 further analysis, event data requests, and orbital image crater searches. These diagnostics are
1535 based on first principles, explosive analogs, and lunar impacts.

1536

1537 *Diagnostics to reject an impact hypothesis:*

1538

- 1539 • **First motion:** An impact event will create a positive pressure impulse at the source, which
1540 will result in a positive first motion (away from the source) for the P-wave. Therefore, in
1541 principle, a negative first motion can be used to rule out an impact event. However, in
1542 practice, this is unlikely to be effective. Even on the Earth, where there are typically many
1543 stations available at various distances, this is considered unreliable because seismic noise can
1544 obscure the very first arrival, and so the direction of motion can be wrongly identified. Also,
1545 earthquakes or marsquakes can produce either a positive or negative first motion depending
1546 on the source mechanism as well as the back-azimuth and take-of angle defined by the source
1547 / station geometry and structure.
- 1548 • **S wave energy:** Impacts are likely to produce stronger P-waves relative to S-waves when
1549 compared to tectonic events, so high S-wave energy could be used to reject an impact source.
1550 However, the P/S amplitude ratio is also a strong function of fault orientation and source/
1551 station geometry, which will introduce uncertainty in this diagnostic.
- 1552 • **Magnitude ratio:** On Earth, one of the most reliable diagnostics for explosive versus natural
1553 sources is comparing the body wave magnitude, m_b , to the surface wave magnitude, M_s . An
1554 earthquake (or marsquake) will produce more surface waves than an explosion (or impact).
1555 Therefore, a plot of M_s versus m_b can potentially be used to diagnose source type.

- 1556 Unfortunately, body wave magnitude will be difficult to estimate accurately from a single
1557 station due to the radiation pattern effect.
- 1558 • **Frequency content:** Impacts and quakes clearly differ in terms of their source mechanisms.
1559 Quakes, which commonly occur as slip on a fault, are typically expressed as a double
1560 coupled force, while impacts are better explained with a single force (Section 3.1). This
1561 results in different frequency content of the seismic signal (Section 3.2). The source time
1562 function of faults is expressed with a step function. The spectrum is flat up to a certain corner
1563 frequency and then rolls off above the corner frequency. The spectrum is commonly
1564 expressed using 2-model, which the spectral power decay with power of -2 (e.g. Aki and
1565 Richards, 2002). The model well explains terrestrial quakes as well as deep moonquakes
1566 (Aki and Richards, 2002; Kawamura et al., 2017). On the other hand, Section 3.1 shows that
1567 source time functions of impacts, either from the GL or SWH models, are expected to be
1568 either derivative or with a high frequency overshoot. This difference in the seismic spectra is
1569 shown in Fig. 7. The spectrum of a quake is flat at low frequencies, similar to those with
1570 $B=0$, while that of an impact has an increase in the power in $\sim 1-2$ Hz. Fig. 4 also shows an
1571 example of spectra from shallow moonquakes and impacts, showing the much smaller cutoff
1572 frequency of the impact spectrum compared to the quake. If these characteristic spectral
1573 features can be observed in the data, we can discriminate impacts from quakes through
1574 spectral analyses as we are locating the source.
 - 1575 • **Depth phases:** For deep marsquakes, in addition to the direct wave, there should be
1576 reflections from the underside of the surface that are sufficiently separated in time to be
1577 identified. For example, the P phase will be followed by the pP phase. If these phases can be
1578 identified in an event, then an impact source can be rejected.

1580 It should be noted these discriminating criteria can be effective if Martian seismograms prove to
1581 be impulsive, like on Earth. If we observe more Moon-like seismograms (Section 2.2, Fig. 3),
1582 where scattering in the regolith produces very emergent long duration signals, it is highly
1583 unlikely any discriminator that relies on clear phase identification can be used. This only leaves
1584 the frequency content analysis (Fig. 4).

1585
1586 When applying these criteria, the usefulness of requested high frequency “event data” in addition
1587 to the continuous 2 samples/sec data (Section 7.1) will depend largely on the event size. For very
1588 large distant impacts, the continuous data should be adequate, as phases will be well separated
1589 and frequency content would be quite low (higher frequencies will be attenuated). In any case,
1590 such a large signal would no doubt be prioritized highly for downlink of event data, whether it
1591 was thought to be a quake or impact. For the more numerous regional events (<1000 km range),
1592 event data would be needed. The most diagnostic positive trait is likely to be the frequency
1593 content. This is likely to be >1 Hz for small events, so event data would be necessary.

1594
1595 With only a single station on Mars, each of these diagnostics alone will have limited use, but by
1596 combining multiple diagnostics, many candidate impact events should be able to be rejected.
1597 Also, once a substantial catalog of marsquakes and impacts has been built up, some of the
1598 uncertainty associated with the fault double couple radiation pattern orientation could be
1599 mitigated if the event can be located and some estimate of regional stress could be incorporated
1600 to predict the mostly likely fault strike orientation. These diagnostics will naturally be refined
1601 during the mission, as more is learned about the seismic characteristics of a Mars impact.

1602
1603 Once a seismic event is determined to be a candidate impact based on these diagnostics, an
1604 estimate of its location will be necessary to find it on the surface. The Marsquake Service (MQS)
1605 will determine, whenever possible, locations and sizes of meteorite impacts from the seismic
1606 signals by applying methodologies and magnitude scales developed by Böse *et al.* (2017) and
1607 Böse *et al.* (in review). Locations will be determined using independent approaches for distance
1608 and azimuth which are subsequently combined. Distance estimates include methods that use 1)
1609 identified body and surface wave phases and 2) multi-orbit surface waves. The latter will only be
1610 available for the largest events, and hence will almost certainly not be used for impact events.
1611 Errors can be included in the single-station event body phase-based distance estimates, as there
1612 are challenges in correctly identifying seismic phases, and there are significant model
1613 uncertainties. Additional errors stem from pick uncertainties. Wrong phase identification can
1614 lead to large errors in locations that are difficult to quantify and are typically not included the
1615 location uncertainty. The probabilistic framework of Böse *et al.* (2017) quantifies the remaining
1616 uncertainties as probability density functions. The key distinguishing features of impacts will be
1617 their spectral content and their shallow depth. It is extremely challenging to constrain event
1618 depth at distance using a single station, but a general indication can be provided by comparing
1619 the relative amplitudes of body and surface waves (Böse *et al.* in prep.). As discussed above,
1620 crustal reflection/depth phases play a critical role in constraining event depth, and these markers
1621 will be identified if possible.

1622
1623 Preliminary tests (Böse *et al.*, 2017) indicate that the errors in the estimated event locations are
1624 small enough to meet the Level 1 requirements of the InSight mission, if multiple clear body and
1625 surface phases are identified. These requirements specify that epicentral distances and back
1626 azimuths are to be determined to accuracies of $\pm 25\%$ and $\pm 20^\circ$, respectively (Banerdt *et al.*,
1627 2013). Very large (and thus very rare) impacts that generate identifiable multi-orbit surface
1628 waves could result in location accuracies as small as 1° (60 km) in distance and 10° in azimuth
1629 (Panning *et al.*, 2015); however, this size impact is exceedingly unlikely to be seen by InSight.
1630 The successful identification and location of meteorite impacts in orbital images is crucial to
1631 generate ground truth locations that will strongly constrain structural models of Mars.
1632 Approximate locations of suspected meteorite impacts will be used as targets for the collection of
1633 high-resolution orbital images to enable visual identification and determination of exact impact
1634 locations (Section 7). The iterative refinement of Mars interior models with every meteorite
1635 impact and marsquake observed during the InSight mission will lead to improved event locations
1636 and reduced uncertainties (Khan *et al.*, 2016).

1637
1638 Airbursts will be even more challenging to detect in seismic signals. When recorded at a seismic
1639 station, the most distinctive feature of an airburst is the arrival of the acoustic airwave. To
1640 distinguish an airwave arrival from other parts of the coda, it is necessary to examine the group
1641 velocity of the arrival. This should correspond to the local atmospheric sound speed. One
1642 potential difference between detection of an airwave on the Earth and Mars is the higher rate of
1643 attenuation in the Martian atmosphere, which may mean that it is difficult to detect this signal
1644 over large distances (Section 4.5.2). It is therefore imperative that the seismically coupled energy
1645 is well understood. If the airburst is large enough, acoustic energy will couple into the ground
1646 and propagate as seismic waves. These will be recorded as precursor signals before the arrival of
1647 the direct airwave. This air-to-ground coupling may produce an emergent waveform, due to the

1648 nature of the coupling along an extended raypath and not simply a point source. The precursor
1649 seismic signals are subject to all of the same principles as impacts, because acoustic-to-seismic
1650 coupling will have a similar effect as a direct surface impact. Further discussion of likely airburst
1651 characteristics can be found in Stevanović et al. (2017).

1652
1653 To detect acoustic waves from impacts, we will examine data from the pressure sensor data on
1654 InSight. The pressure sensor will be continuously sampled at 20 samples per second (SPS), and
1655 its instrument response should cover the infrasonic frequency range. The sensor will have good
1656 response to signals $< \sim 5$ Hz. The sampling limits it (with Nyquist sampling) to < 10 Hz. The
1657 plumbing on the inlet, and a low-pass filter in the sensor electronics, both limit it to $< \sim 5$ Hz. We
1658 were unable to verify this in the laboratory, as the calibration system only successfully
1659 modulated the tested pressures at up to ~ 1 Hz. The precise cutoff frequency will be assessed
1660 after landing. Consequently, this sensor may detect acoustic waves created by impacts. However,
1661 only data at 2 SPS will be sent back to Earth continuously. To monitor pressure signals at
1662 frequencies above 1 Hz, the energy of pressure variations in the 1-10 Hz frequency range will be
1663 computed on the lander and sent back to Earth at 1 SPS. This energy channel, named ESTA for
1664 Energy Short Term Average, will be analyzed by the science team to detect high frequency
1665 infrasound signals. Then, a request for high rate data will be sent to the lander to recover the time
1666 windows containing candidate infrasound events.

1667
1668

1669 **6.2 EXPECTED FREQUENCY OF SEISMIC IMPACT DETECTIONS**

1670
1671 The frequency of impact seismic signals InSight will detect is based on several factors: the
1672 incipient bombardment rate (Section 4.1); the efficiency of partitioning the impact energy of
1673 those impacts into seismic energy (Section 3.3); the nature of an impact's source time function
1674 (Section 3.1); propagation effects between the impact and the SEIS location and associated
1675 amplitude reduction due to geometrical spreading, attenuation, and scattering; and, last but not
1676 least, the amplitude of the resulting signals compared to the noise level of SEIS (Section 5.2).
1677 Large uncertainties on all of these factors makes it very difficult to determine the efficacy of
1678 InSight's monitoring of natural impacts. However, general trends can be predicted. For example,
1679 the larger the impact, the farther away it will be able to be detected. Using an overall impact rate
1680 and taking these factors into account, a detection rate can be estimated.

1681
1682 Teanby (2015) and Daubar et al. (2015) use independent approaches to estimate the relationship
1683 between seismic detectability and crater size. Teanby (2015) use empirical scaling laws based on
1684 lunar/terrestrial impacts, missile tests, and explosions to determine a relation between impact
1685 energy and seismic amplitude as a function of distance. Daubar et al. (2015) use estimation of the
1686 amplitude from Apollo impact observations, corrected for *a priori* differences between Mars and
1687 the Moon. See Lognonné and Johnson (2015) for details. The predictions of the two methods are
1688 compared in Table 3 and Fig. 30. These two approaches differ from the modeling hypothesis.
1689 These preliminary estimates are dependent on various unknown parameters such as the noise
1690 levels of the SEIS instrument, seismic efficiency, and attenuation in the Martian interior, so have
1691 large uncertainties. In any case, small impacts will only be detectable within a very limited range
1692 of the InSight landing site. Only impacts producing craters $> \sim 30$ -40 m in diameter will be
1693 detected at very far distances.

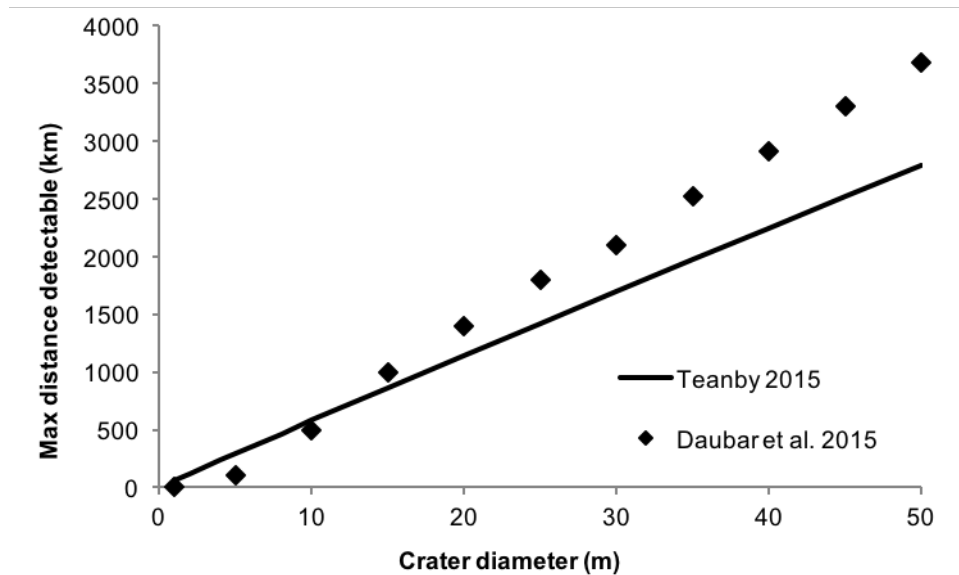
1694
1695
1696
1697
1698
1699
1700

Table 3:

Distance at which an impact forming a crater of a given diameter is estimated to be detectable by SEIS, using two different methods of estimation. These preliminary estimates are dependent on various unknown parameters such as the noise levels of the SEIS instrument, seismic efficiency, and attenuation in the Martian interior.

Crater diameter (m)	Distance (km), Teanby 2015	Distance (km), Daubar et al. 2015
1	61	10
5	295	100
10	580	500
15	862	1000
20	1141	1400
25	1419	1800
30	1696	2100
35	1971	2523
40	2246	2909
45	2519	3296
50	2792	3682

1701



1702
1703
1704
1705
1706

Figure 30:

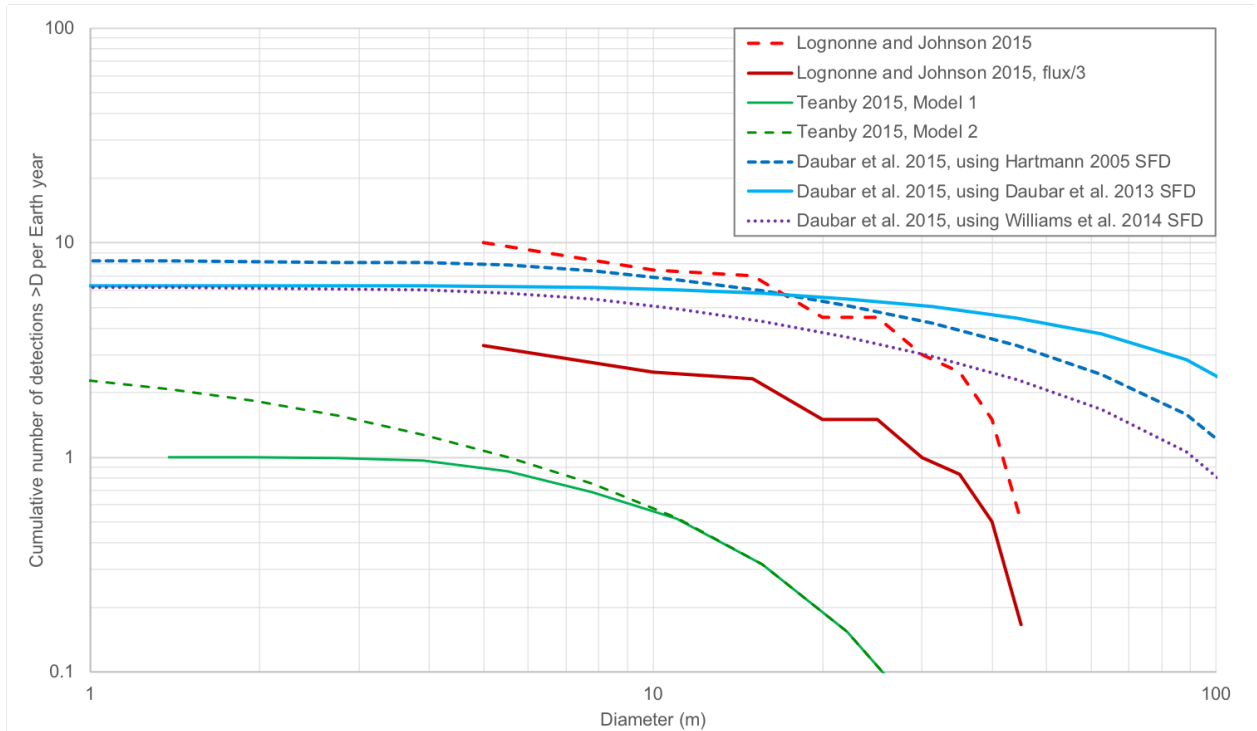
Distance at which an impact forming a crater of a given diameter is estimated to be detectable by SEIS, using two different methods of estimation. See text for details about the two methods. These preliminary estimates are dependent on various unknown parameters such as the noise

1707 *levels of the SEIS instrument, seismic efficiency, and attenuation in the Martian interior, so have*
1708 *large uncertainties.*

1709

1710 When the dependence between size and distance for detectable impacts (Fig. 30) is combined
1711 with the best measurements of the current impact rate (Section 4.1), we can calculate an overall
1712 estimate of the number of impacts detectable by SEIS per year (Fig. 31). Several estimates of this
1713 rate have been published (Davis, 1993; Teanby and Wookey, 2011; Lognonné & Johnson 2015;
1714 Teanby, 2015; Daubar et al., 2015). Results are shown in Fig. 31 for cumulative impact detection
1715 rate per year for various of these models. Two factors balance each other out in the calculation of
1716 total detections. Many small impacts are occurring on Mars, but the detection distance is the
1717 limiting factor. There is very low likelihood that even a small impact will occur very close to
1718 InSight. The chances are also low of forming a crater large enough to detect even at great
1719 distances. In the last decade of monitoring the dusty areas of Mars, only a few craters have been
1720 observed to form that are larger than 30 m in diameter; the largest new impact to be found with
1721 before and after images thus far is 60 m. However, these observations are limited to dusty areas,
1722 and require multiple images spaced in time to capture the event. The Hartmann and Daubar
1723 (2017) production function predicts ~6 craters larger than 30 m occur somewhere on the entire
1724 planet Mars each Earth year, but not all of those are observed in orbital images.

1725



1726

1727 **Figure 31:**

1728 *Predicted number of cumulative SEIS impact detections per Earth year for a given crater*
1729 *diameter, made using various models and published production functions (size frequency*
1730 *distribution; SFD) to estimate the current impact rate. The Teanby (2015) model is for the SP*
1731 *(short period) sensors in SEIS, which has a sensitivity to impacts approximately eight times*
1732 *lower than the VBB (Very Broad Band) sensors, which the other models use. All of these*
1733 *estimates have an order of magnitude uncertainty. See text for more details.*

1734
1735 The models shown here differ in several ways. Lognonné & Johnson (2015) used data from the
1736 Apollo Network (Lognonné et al., 2009) to calculate impact amplitudes as function of the impact
1737 momentum and distance to station. They then corrected these amplitudes for the difference in
1738 seismic attenuation between Mars and the Moon, noting however that the latter is not major, as
1739 the source cutoff of impacts is likely the major frequency cutoff for impacts recorded at several
1740 thousand kilometers. Detections were then modeled with Monte-Carlo simulations using the
1741 impact flux of Lefevre and Wieczorek (2011). Both Teanby and Wookey (2011) and Daubar et
1742 al. (2015) used the impact flux based on the recently occurring impacts observed by MRO. This
1743 flux has been discussed in section 4.1 and is approximately three times smaller than that of
1744 Lefevre and Wieczorek for the size impactors generating observable signals. For this reason,
1745 the Lognonne and Johnson (2015) results are also shown in Fig. 31 divided by a factor of three to
1746 correct for that lower observed rate.

1747
1748 Daubar et al. (2015) used the same relationship between momentum and observed seismic
1749 amplitude as Lognonné & Johnson (2015), but used different published size frequency
1750 distribution (SFD) models of the impact rate. In contrast, Teanby and Wookey modeled the
1751 seismic waves using the Direct Solution Method and then estimated the amplitude of seismic
1752 waves on the seismic efficiency figure. Based on this measured rate of impacts, Teanby and
1753 Wookey (2011) predict a total impact-induced seismicity of Mars of 10^{13} – 10^{14} N m per year.
1754 Teanby (2015) extrapolated this down to smaller impacts, which have not been observed from
1755 orbit, but that may be detectable seismically (their Model 2). Another difference between the
1756 Teanby (2015) model and the other two sets of models is that Teanby (2015) used a noise level
1757 of 10^{-8} m/s²/sqrt(Hz), which is a conservative value appropriate for the SP (short-period) sensors
1758 in SEIS. The Lognonne & Johnson (2015) and Daubar et al. (2015) models use predicted noise
1759 limits for the VBB (Very Broad Band) sensors. At these frequencies, ~ 0.5 – ~ 2 -3 Hz, the VBB is
1760 a factor of ~ 10 better than the SP in detected amplitude and therefore in detected seismic
1761 moment (Mimoun et al. 2017). Thus the VBB may detect ~ 8 times more impacts than the SP.
1762 However, the highest frequencies from these small events will be above 1 Hz, which is
1763 approaching the higher ambient/instrument noise crossover. Explosion/impact data from Teanby
1764 (2015) had peak frequencies ~ 1 –16 Hz. The upper end of this range is not critical, as most of the
1765 data had peaks in the 1–4 Hz range (e.g. the Apollo impacts ~ 2 Hz; Fig. 4). So some degree of
1766 enhanced detection from the VBB over the SP is expected, but drastically lower noise levels may
1767 not be achievable for frequencies ~ 1 –2 Hz. For the ambient noise, this could be challenging.

1768
1769 For this and other reasons, the resulting overall estimates of seismic impact detections (Fig. 31)
1770 are uncertain to several orders of magnitude because of the undetermined seismic properties of
1771 Mars such as attenuation, seismic coupling efficiency, and uncertainty in the current impact rate
1772 itself. Additionally, although the noise levels of SEIS have been modeled (Murdoch et al. 2017;
1773 Mimoun et al. 2017) and tested on the Earth to verify the required noise levels will be met, the
1774 true noise of the system will not be known until the seismometer is deployed on the surface of
1775 Mars. Given those uncertainties, Teanby (2015) estimates somewhere between ~ 0.1 –30 impacts
1776 per Earth year will be detectable at moderate distances of less than $\sim 1,000$ km. Lognonne &
1777 Johnson (2015) predicted ~ 10 impacts per year using the impact flux of Lefevre and Wieczorek
1778 (2011), which would be reduced to ~ 3 per year when using the latest constraints on the impactor
1779 flux. For very large events that could be detected globally, Teanby and Wookey (2011) estimate

1780 these occur only once every 1 to 10 years. Daubar et al. (2015) derived a similar estimate of ~4-8
1781 total impacts would be detected per Earth year (~8-16 in the primary InSight mission).

1782
1783 It should be noted that all of these estimates assume single-crater, unfragmented impactors.
1784 Atmospheric fragmentation leading to clusters of impacts will affect the seismic detectability of
1785 approximately half of current Martian impactors (Daubar et al., 2018; Schmerr et al., 2016)
1786 (Section 4.5).

1787
1788 Another factor that will reduce the number of detections is the low seismic moment associated
1789 with small impacts, and the fact that their high frequency energy is still limited by the source
1790 cutoff, a few Hz for the smallest detected by Apollo (Fig 8). Scaling laws (Fig. 6) predict that the
1791 detectability of an impact drops by a factor of $10^{2.5}$ - 10^3 for every order of magnitude drop in
1792 crater diameter. Even this detectability assumes a relatively quiet background; the Martian
1793 environment is contaminated by abundant wind noise in the 10^{-6} m/s² amplitude range as
1794 detected by Viking 2 on the lander deck (Anderson et al., 1976; Nakamura and Anderson, 1979).
1795 However, this noise level is three orders of magnitude larger than the expected InSight noise
1796 level at 1 Hz (Mimoun et al., 2017), so Viking's non-detection is easy to understand. For InSight,
1797 noise may be even lower than the requirement during the relatively quiet nights. Thus impacts
1798 generating smaller craters could be detected by InSight if they occur nearby, during periods of
1799 low wind activity, or in the night time.

1800
1801

1802 **7 OPERATIONAL PLANS**

1803

1804 **7.1 ROLE OF IMPACTS SCIENCE THEME GROUP**

1805

1806 The Impacts Science Theme Group (STG) has two main tasks: to coordinate scientific analyses
1807 by the InSight team related to impact cratering; and to ensure sufficient and appropriate data are
1808 acquired during the mission to perform those analyses. For the latter task, the Impacts STG will
1809 support surface operations of the InSight mission by participating in the science planning
1810 process. In the science monitoring phase, these operations are on a weekly cycle that is mainly
1811 focused on prioritizing downlink of high temporal resolution SEIS event data. The full
1812 operational process is described in Banerdt et al. (this issue). The Impacts STG will be made
1813 aware of potential impact detections via the Mars Quake Service (MQS, Clinton et al., 2018).
1814 Relative prioritization among candidate impact events will be made at a weekly Impacts STG
1815 telecon prior to the Event Selection meeting. The Impacts STG will then send a representative to
1816 the Event Selection meeting to advocate for our highest priority event data. On a more long-term
1817 strategic timeline, the Impacts STG will have a representative at the Science Operations Working
1818 Group (SOWG) meetings. The Impact theme group's weekly telecons will also be used to
1819 organize and prioritize orbital image requests and collaborate on ongoing research activities.

1820

1821 Certain scientific investigations are desirable for impact science, but they are not part of the
1822 baseline mission plan of operations. For example, imaging at night to search for meteors as
1823 described in Section 7.2 will require additional planning and resources. The Impacts STG will
1824 seek approval for special activities such as these via Science Activity Requests. These requests

1825 will be prioritized by the science team and, based on those priorities, inserted into the tactical
1826 planning process.

1827
1828 During normal operations, the Impacts STG will prioritize event data for candidate impact
1829 events. Data acquired by SEIS is stored and processed by the flight software on board InSight.
1830 Two types of data are treated differently for downlinking:

- 1831
- 1832 1) *Continuous data* are low temporal resolution (i.e. decimated) (2 samples/sec) data
1833 processed and downlinked daily with no time gaps within the data.
1834
 - 1835 2) *Event data* are full-resolution raw scientific data acquired and filtered from the
1836 instrument. Time segments of this full-rate data can be extracted, filtered, compressed,
1837 and then downloaded on request. Those segments are called event data.
- 1838

1839 Because the high-frequency SEIS data cannot all be downlinked due to data volume limitations,
1840 individual events must be identified in the lower resolution continuous data and prioritized for
1841 high-frequency event data retrieval; high-frequency SEIS data is stored on the spacecraft for
1842 approximately one month before it is overwritten. The STGs will prioritize this high-frequency
1843 event data for downlink within the data volume constraints each week.

1844
1845 During routine operations, the SOWG (Science Operations Working Group) and the APAM
1846 (Activity Plan Approval Meeting) meetings lead to the definition of an Activity Plan containing
1847 placeholders for Event Requests. Those placeholders are filled with ERPs (Event Request
1848 Proposals) submitted by the Science team during the week. Any scientist can submit an ERP that
1849 will be reviewed and ranked among others during the Event Selection Meeting.

1850
1851 The Event Selection Meeting is led by the long-term planner (LTP) and chaired by the SEIS and
1852 mission PIs. Participants include PIs from SEIS, Temperature and Wind for InSight (TWINS),
1853 IFG (InSight Fluxgate), and PS (Pressure Sensor), STG leads pertinent to event selection,
1854 representatives from MQS (Marsquake Service), MWS (Mars Weather Services), SEIS
1855 community, and public outreach. See Banerdt et al. (this issue) and Lognonné et al. (this issue)
1856 for more details on these operational meetings. The role of the Impacts STG during this process
1857 will be to prioritize among various candidate impact events identified by the MQS or science
1858 team members, and advocate for the highest-priority event data potentially related to impacts.
1859 Priorities may be based on the estimated size and distance to the impact (larger or closer events
1860 will be a higher priority), or any unusual aspects of the signal as seen in the continuous data.

1861 1862 **7.2 ORBITAL IMAGING**

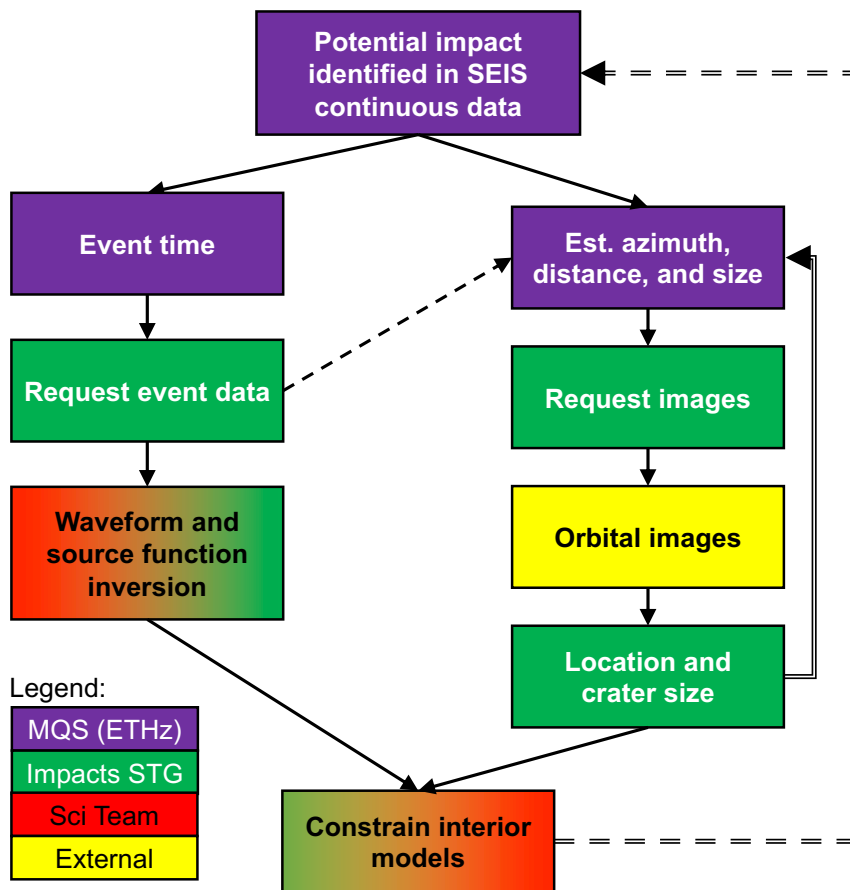
1863
1864 Once InSight detects an impact in seismic data and a location estimate is available, images will
1865 be requested from one of the currently-orbiting spacecraft around Mars with the goal of
1866 pinpointing the exact impact location via visual detection of newly formed crater(s). High
1867 resolution images will allow for characterization of the craters' morphology. Exact locations and
1868 sizes of the new craters will allow for determination of the ray paths and thus calibrate interior
1869 structure models and seismic attenuation. This will drastically reduce the uncertainties in our
1870 knowledge of Martian interior structure. Any successful detections will provide a link between

1871 the crater size (and thus impact energy) and seismic coupling of impacts, calibrating the seismic
1872 efficiency. Each impact site characterized from orbit will additionally reduce the uncertainty on
1873 the crater sizes, distances and azimuths estimated by the Marsquake Service. For these reasons,
1874 orbital imaging of seismically-detected impact sites will be of high scientific importance.
1875

1876 **7.2.1 OPERATIONAL PROCESS**

1877
1878 Using the various techniques described in Section 6.1, suspected impact events will be
1879 distinguished from internal marsquakes in the continuous data from SEIS (Fig. 32). The MQS
1880 will provide the science team the estimated location of the detected event, with uncertainties, as
1881 well as its type (impact vs. quake). Once an impact event is identified, the Impacts STG will
1882 prioritize the downlink of that time period of high-frequency SEIS event data, which is stored on
1883 the spacecraft for later retrieval. The initial detection will be accompanied by an estimate from
1884 the MQS of the location in azimuth (target uncertainty is $\pm 20^\circ$), distance (target uncertainty is
1885 $\pm 25\%$), and the equivalent tectonic magnitude. These uncertainties are conservative and will
1886 improve drastically through the mission using known event locations confirmed in orbital
1887 images. Actual uncertainties will also be provided. These are dependent on the number and
1888 quality (temporal uncertainty) of the identified phases, the signal-to-noise of the various phases,
1889 and the uncertainty in the structural models. The model uncertainty should be reduced as well-
1890 located tectonic and impact events are added to the emerging event catalog. The largest and
1891 closest events will have smaller uncertainties in terms of area. The location uncertainty could be
1892 as small as 10° in azimuth and 1° in distance (Panning et al., 2015) for very large events (~ 1 km
1893 diameter crater). However, impacts this large are exceedingly unlikely to occur within the
1894 InSight primary mission: on average, a 1-km crater is formed on Mars approximately once every
1895 10,000 years (Hartmann and Daubar, 2017). In any case, these uncertainties will be reduced after
1896 just a few well-located events are detected and more is learned about the Martian interior.
1897

1898 If the resulting images can provide a crater location and size, these independently-determined
1899 parameters will be used to improve the algorithms and procedures used by the MQS. When an
1900 impact has been confirmed by orbital images, the known position, elevation, and event type
1901 (impact) will be entered into subsequent MQS catalogs as fixed values. Further, the magnitude
1902 will be recomputed against these location parameters. Most crucially, this fixed and known
1903 impact location can be used by the MSS to constrain interior properties of Mars and hence refine
1904 candidate models of the Martian structure. These improved models will be used to provide
1905 updated seismicity catalogues with improved locations (Section 8.1).
1906



1907
1908

1909 **Figure 32:**

1910 *Schematic of operations planned for impact detection. The color of each step indicates the team*
 1911 *responsible. Once a potential impact is detected by the MQS in the continuous SEIS data, two*
 1912 *separate flows are initiated. The Impacts STG requests the event data through the weekly event*
 1913 *selection process, and also requests orbital images based on the estimated location of the*
 1914 *impact. If event data are required to either confirm an impact, or more precisely estimate its*
 1915 *location, the image requests will follow acquisition of event data (dashed line). The results of*
 1916 *analyzing either the high resolution event data and/or the orbital images will improve estimates*
 1917 *of impact locations (double line), and will be used to provide measurements of cratering*
 1918 *efficiency and interior properties. Likewise, the constraints on interior models will be fed back*
 1919 *into the analysis of new events to improve initial identifications (dashed double line).*

1920

1921 Based on the estimated size of the crater, the appropriate imager will be contacted (Table 4).
 1922 Orbital images will be searched for the extended blast zone around the impact site, which is ~10
 1923 to ~100 times larger than the craters themselves (Ivanov et al. 2010; Bart et al., 2013); the craters
 1924 themselves will not be resolved in these initial search images. Very large impacts will be able to
 1925 be detected in lower-resolution data. The location uncertainty is a percentage of the estimated
 1926 distance; thus more distant events will be less well-constrained in areal extent. However, it
 1927 would be a waste of resources to attempt to search vast areas with many high-resolution images.

1928 The number of images needed to cover the location estimate will also depend on the orientation
 1929 of the region of the location estimate with respect to the spacecraft groundtrack; if the region is
 1930 elongated along-track, for example, it will be easier to cover with fewer images. The location of
 1931 the impact will also be taken into account: dusty areas are known to exhibit extended low albedo
 1932 blast zones around new impacts, aiding their detection in lower-resolution images (Malin et al.,
 1933 2006; Daubar et al., 2013, 2016). The same size impact in a dust-free area will require higher-
 1934 resolution images to detect (see Section 7.2.2 for more details).

1935
 1936 For impacts relatively close to the InSight lander, CTX (6 m/px; Malin et al., 2007) or even
 1937 HiRISE (25 cm/px; McEwen et al., 2007) images will be requested. Impacts that occur very far
 1938 from the InSight lander will necessarily be much larger to produce a detectable seismic signal;
 1939 these may even be detectable in data from Mars Color Imager (MARCI; 1-10 km/px; Bell et al.,
 1940 2009). MARCI has detected new craters before: a ~40 meter crater was discovered that formed
 1941 between MARCI images on subsequent days
 1942 (<https://www.jpl.nasa.gov/news/news.php?release=2014-162>). InSight could also request follow
 1943 up images from THEMIS (THERmal EMission Imaging System on Odyssey; Christensen et al.,
 1944 2004) for intermediate-sized impacts. Images from the Colour and Stereo Surface Imaging
 1945 System (CaSSIS) on the Trace Gas Orbiter (TGO) (Thomas et al., 2017) will also be requested;
 1946 however, that camera's inability to point more than a few degrees off-nadir will limit targeting
 1947 opportunities.

1948
 1949 **Table 4**

1950 *Orbiting camera most appropriate for a given impact crater size and distance. Note that*
 1951 *individual craters are not expected to be resolved in these data, rather the goal will be to detect*
 1952 *the extended blast zone around the impact.*

Imager	Pixel size	Footprint size (approx)	Corresponding crater diameter	Distance range
MARCI	1-10 km	global map	> 40 m	Global
THEMIS	18 m	20 km	~20-40 m	~1500-2500 km
CTX	6 m	30 km x 160 km	~1-10 m	<500 km
CaSSIS ¹	5 m	8 km	~1-10 m	<500 km
HiRISE ²	0.25 m	1.2 km x 10 km	All, follow up	All, follow up

1953 ¹CaSSIS has limited ability to point off-nadir or target observations.

1954 ²HiRISE will be requested as a follow up in all cases to measure exact crater parameters.

1955
 1956 HiRISE images will be requested for follow-up images, after an impact blast zone is detected in
 1957 lower-resolution data (with the possible exception of extremely close impacts estimated to be
 1958 within one HiRISE image width of the InSight lander). Once a new crater is found in lower
 1959 resolution data, a representative of the Impacts STG will create a target in the public targeting
 1960 tool HiWish (www.uahirise.org/hiwish/; McEwen et al., 2010), which is available to any
 1961 member of the scientific or public community. From there, the target will go to the HiRISE team
 1962 for prioritization and acquisition.

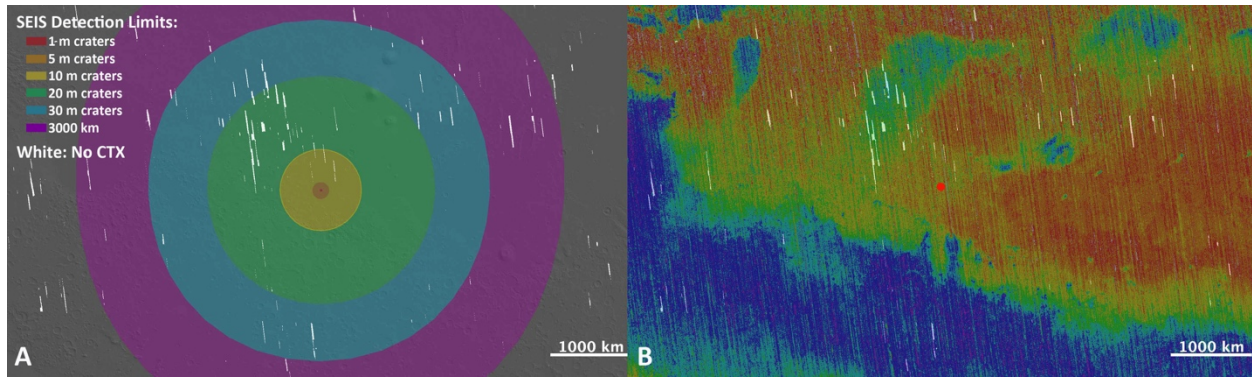
1963
1964
1965
1966
1967
1968
1969
1970
1971
1972
1973
1974
1975
1976
1977
1978
1979
1980
1981
1982
1983
1984
1985
1986
1987
1988
1989
1990
1991
1992
1993
1994
1995
1996
1997
1998
1999
2000

7.2.2 IMAGE ANALYSIS

Currently-forming Martian impact craters are relatively small in size (typically <40 m in diameter) (Daubar et al., 2013). For the most part, these new craters will only be resolved in images from the High-Resolution Imaging Science Experiment (HiRISE, 0.25 m/pixel). However, the initial identification of impacts detected by InSight will likely involve detection of the extended “blast zone,” a low-albedo area of disturbed dust around the impact, as has been used in the past for new impact detection (Malin et al. 2006; Daubar et al., 2013; 2016). These blast zones enable use of a wider range of imagers for detection of these new impacts and comparison to previous surface conditions. The size of a blast zone relative to the crater size varies widely, ranging from ~10 to ~100 times larger (Ivanov et al. 2010; Bart et al., 2013). The InSight landing site is conveniently located in a dusty area (Golombek et al., 2017), the type of surface on which these blast zones form. Dust covers most of area north of InSight, from the northwest to the southeast, but areas to the south and southwest are not dusty (Fig. 33).

Impacts in areas without a surface layer of material with an albedo contrast are much more difficult to detect. Witness the strong bias in detected dated impacts towards dusty areas of Mars (Daubar et al., 2013). Having a relatively high resolution “before” image demonstrating the lack of a crater is thus even more important in dust-free areas. For this reason the number and resolution of images requested, and the thoroughness of search required, will differ depending on whether the estimated location based on seismic data is in a dust-covered or dust-free area.

Previously acquired images will be critical for positively identifying a fresh-looking impact site as new since the most recent image. CTX onboard MRO has covered 99% of the surface of Mars with >90,000 6 m/px images (<https://mars.nasa.gov/news/prolific-mars-orbiter-completes-50000-orbits/>), so there are few gaps where “before” CTX images are not presently available. In support of the landing site selection process, the InSight landing ellipse region has complete CTX and >90% HiRISE coverage (Golombek et al., 2017). Farther from InSight, CTX coverage is nearly complete as well: as of the time of this writing, only a few gaps in coverage remain within a ~3000 km radius of the InSight landing ellipse (particularly to the north and northwest) (Fig. 33). However, some of the acquired images are poor quality due to dust or haze in the atmosphere. Additional orbital image data will be used to fill those gaps due to missing or poor-quality images. These include data from the THEMIS visible and infrared imaging systems, HiRISE, Mars Orbiter Camera (MOC) (Malin et al., 2010), and the High Resolution Stereo Camera (HRSC) (Neukum and Jaumann 2004; Jaumann et al. 2007; Gwinner et al., 2016). As these images are of various ages, the most recent images will be the most valuable.



2001
2002

2003

Figure 33:

2004 *CTX image coverage (PDS-released images available in JMARS (Christensen et al. 2009) as of*
 2005 *January 2018) with (A) detectability of impacts and (B) dust coverage in the InSight landing site*
 2006 *area. White areas indicate gaps in CTX coverage at the time of this writing. (A) Colors indicate*
 2007 *the distance at which a given size impact can be located, using the relationships estimated in*
 2008 *Section 6.2. (B) Thermal Emission Spectrometer dust cover index (DCI) (blue = less dust;*
 2009 *DCI<0.96 = green, yellow, orange, and red) (Ruff and Christensen, 2002). Map centered at*
 2010 *InSight landing site at 4.5°N, 135.9°E (red dot). MOLA shaded relief base courtesy of*
 2011 *NASA/JPL/Goddard.*

2012

2013 Remote sensing data for the InSight landing site in western Elysium Planitia suggests it is
 2014 moderately dusty (Golombek et al., 2017). The relatively high albedo of the InSight landing sites
 2015 (0.24) argues for a thin coating of dust similar to the dusty portions of the Gusev cratered plains,
 2016 which have an albedo of 0.26 (Golombek et al. 2005). The TES dust cover index (DCI) (Fig. 33),
 2017 which includes a more explicit measure of the presence of a thin dust layer (Ruff and Christensen
 2018 2002), of the InSight landing site is similar to the VL2 landing site and only slightly dustier than
 2019 VL1 and Spirit. This value (DCI=0.94) is consistent with a thin coating of dust. The bulk thermal
 2020 inertia limits the dust layer to less than 1-2 mm thick, and it is more likely a very thin but
 2021 optically thick veneer of fine grained (< few micrometers) dust (Golombek et al., 2017). Impacts
 2022 detected in before and after visible images are preferentially found in areas with DCI<0.96
 2023 (Daubar et al., 2013). Maps show that most of the surface within 3000 km of the landing site
 2024 have DCI values < 0.96 (fairly dusty) and a relatively high albedo of > 0.2 (green, yellow, orange
 2025 and red in Fig. 33B). Thus new impacts in these areas should be detectable in visible images
 2026 from orbit because they should form a darkened blast zone around the impact site, based on past
 2027 experiences with new dated impacts on these types of surfaces (Daubar et al. 2013; 2016). Areas
 2028 ~1000 km south of the landing site in (blue in Fig. 33B) have a higher dust cover index and
 2029 lower albedo, both of which imply less dust coverage. This will potentially make orbital
 2030 detection of new impacts more difficult here.

2031

2032 Orbital images will be manually searched for new impacts by the Impacts Science Theme Group.
 2033 In dusty areas, fresh impacts are easily recognizable from the low-albedo "blast zone" (Fig. 13).
 2034 Thus in dusty areas, this search will be fairly straightforward as long as previous images are
 2035 available, as discussed above. In non-dusty areas, the search will need to be more intense. In both
 2036 dusty and dust-free areas, if prior images of sufficient quality and resolution are not available, a

2037 fresh-appearing impact site found in the area will have a high likelihood of being associated with
2038 the event.

2039

2040 **7.2.3 AUTOMATED IMAGE SEARCH**

2041

2042 As a supplement to manual searching, and to assist in difficult searches, software is being
2043 developed to perform automated image searching. This search will use the Mars Impact
2044 Detection Algorithms (MIDA) software developed at Centre National d'Etudes Spatiales
2045 (CNES), USGS Integrated Software for Imagers and Spectrometers (ISIS) (e.g., Becker et al.,
2046 2013), and in-house image processing that integrates MIDA, ISIS, a geoserver, and a front-end
2047 interface. New images of the impact event area will be automatically compared to pre-existing
2048 base maps consisting of previous images at global and regional scales. Image information will
2049 come from HRSC mosaics (20 m/pixel) at global scale, CTX mosaics (6 m/pixel) up to 20°
2050 (~1000 km) from the lander site, and all available observations that may be available from
2051 CaSSIS/TGO (6 m/pixel) and HiRISE (25 cm/pixel) inside a circle 5° (~300 km) around the
2052 lander site. These basemaps are undergoing pre-processing and will be ready for the beginning of
2053 the landed mission in November 2018.

2054

2055 The MIDA software uses these basemaps as the basis of comparison for change detection. To
2056 produce these, raw CTX images are radiometrically corrected to adjust for mean values of
2057 central detectors that are higher than those on the edges of the swath. Each image is
2058 orthorectified, sampled at exactly the same pixel size (5 m), and given an equirectangular
2059 projection. Images are then georeferenced to the 100 m Mars Odyssey THEMIS global mosaic
2060 (Edwards et al., 2011) and mosaicked. Algorithms have been built to detect new impacts relative
2061 to these basemaps, despite changing sun illumination. It is fairly easy for a human to detect
2062 impacts in dusty areas, so the challenge for this software is to detect impacts in non-dusty areas.
2063 Machine learning approaches are under study to enhance the detection rates while reducing the
2064 number of false positives. For more details on this software, see May et al. (2018, submitted.)

2065

2066 The automated image search workflow pipeline will be triggered when new image data are
2067 available, associated with a MQS event alert of a candidate impact. As we intend to continuously
2068 update the basemaps as new orbital observations become available, the MIDA software will also
2069 be able to detect new impact craters and/or surface signature changes, even outside the official
2070 framework of MQS seismic alerts. The workflow can also be triggered on request by team
2071 members.

2072

2073 **7.3 METEOR IMAGING**

2074

2075 Meteoroids come in all sizes, including those small enough to ablate completely in the thin
2076 Martian atmosphere. These may not be large enough to create craters and seismic signals, but
2077 InSight's cameras could still detect the passage of those meteors across the night sky. This would
2078 be a direct empirical measurement of the micrometeoroid flux at Mars, which would constrain
2079 models of the distribution of small particles in the solar system as a function of distance from the
2080 Sun, contributing to constraints on models all sizes of interplanetary bodies.

2081

2082 Night time meteor imaging was first attempted by the MER Rovers, with an initial report of a
 2083 meteor detection (Selsis et al., 2005). Unfortunately, this was later found consistent with the
 2084 morphology and size distribution of cosmic rays (Domokos et al., 2007), thus resulting only in an
 2085 upper limit of the meteoroid flux at Mars. InSight represents another opportunity to pursue this
 2086 scientific goal at the surface of Mars, and the improved camera sensitivity over those used on
 2087 MER makes this a promising pursuit.

2088
 2089 Predictions of Martian meteor showers bright enough for possible detection by the InSight
 2090 mission were performed following Vaubaillon et al. (2005) and Vaubaillon (2017). The results
 2091 are shown in Table 5. The best opportunities result from comets 2004 TG10, 49P, C/1854 L1,
 2092 and 2002 EV11. However, the first two are long period comets, causing the stream to spread
 2093 over huge distances, and therefore reducing the meteoroid spatial density.

2094
 2095 *Table 5.*

2096 *Prediction of meteor showers at Mars. **d**: Closest distance in astronomical units (AU) between*
 2097 *the center of the meteoroid stream and the planet’s path. **Date**: Date of shower (Earth UTC),*
 2098 ***ZHR**: Level of intensity of the shower, i.e. number of meteors a human would witness with the*
 2099 *naked eye each hour, under perfect conditions. **Conf_index**: confidence index as defined in*
 2100 *Vaubillon (2017): a leading “G” for Global indicates that the whole stream is taken into*
 2101 *account; Y for Year indicates all predictions are for specific years indicated; following O for*
 2102 *Observations, the number of observations of the body is compared to the number of simulated*
 2103 *returns; and finally “CUX.XX” provides information regarding the close encounters the parent*
 2104 *body has encountered before it was observed: X.XX=0.00 indicates that the orbit is fairly well*
 2105 *known, and the higher the number X.XX, the higher the uncertainty regarding its past orbit.*
 2106

Parent	d (AU)	Date	ZHR	Conf_index
2004 TG10	-0.01976	2018-12-13T02:14	111	GY00/4CU0.10
4D/Biela	0.01717	2018-11-24T20:10	2	GY03/38CU0.00
LONEOS-2001R1	0.02453	2018-12-24T18:55	1	GY00/28CU0.00
252P/Linear	-0.01940	2019-11-16T08:35	5	GY00/49CU22.58
4D/Biela	0.00074	2019-12-11T21:11	3	GY03/38CU0.00
49P	0.00844	2019-06-11T13:11	112	GY06/6CU0.00
2005 ED318	0.02483	2019-07-24T16:33	1	GY01/21CU0.00
C/1854 L1	0.00655	2019-09-26T22:29	41	GY00/9CU0.00
2002 EV11	0.00122	2019-11-01T23:12	90	GY01/21CU0.00

2107
 2108
 2109 InSight has two cameras that would be available to image meteors (Maki et al., this issue). The
 2110 Instrument Deployment Camera (IDC) and Instrument Context Camera (ICC) on the InSight
 2111 lander are both flight spare units from the Mars Science Laboratory (MSL) engineering camera
 2112 development program (Maki et al., 2012), which are copies of the Mars Exploration Rover

2113 (MER) engineering cameras (Maki et al., 2003). The IDC is a flight spare MSL Navcam, and the
2114 ICC is a flight spare Hazcam. The InSight project has replaced the MSL monochrome detectors
2115 with Bayer color filter array (CFA) detectors, removed the neutral density filters, and replaced
2116 the visible cutoff filters with IR cutoff filters. The color upgrade has resulted in two main
2117 differences relative to the MER/MSL cameras: 1) red, green, and blue bandpasses centered at
2118 wavelengths of approximately 450, 550, and 620 nm, respectively, and 2) a factor of five
2119 increase in responsivity. This puts the InSight cameras on par with the MER Pancam L1 filter,
2120 the most sensitive of the Pancam filters. Other than the color upgrade, the cameras are essentially
2121 identical to the MER/MSL versions. For more information on the InSight cameras, see Maki et
2122 al. (this issue).

2123
2124 Domokos et al. (2007) found that the MER Pancam L1 (broadband visible) filter could be used
2125 to detect meteors to a limiting magnitude of 0.5 to 1.6, corresponding to meteors of 0.1-0.2 g.
2126 For that range, they predict 1.4×10^{-5} to 5.7×10^{-5} meteoroids $\text{km}^{-2} \text{h}^{-1}$ for a limiting magnitude
2127 up to 1.61 and estimate an upper limit value of $<5.4 \times 10^{-6}$ meteoroids $\text{km}^{-2} \text{h}^{-1}$ for a limiting
2128 magnitude up to -4.01. However, because they could not determine that all streaks were cosmic
2129 rays with their methodology, Domokos et al. (2007) caution that the real upper limit may be a
2130 few times higher. The InSight cameras are roughly as sensitive as the Pancam L1 filter, and
2131 should be sensitive to slightly smaller meteors due to the larger IFOV (at the same angular speed
2132 a meteor spends more time within a single IDC or ICC pixel). Due to the larger FOV (FOV of
2133 $45^\circ \times 45^\circ$), an IDC image will cover ~ 8 times more sky compared to Pancam; aimed at the same
2134 elevation (typically $\sim 38^\circ$ in the MER meteor searches) the IDC could reproduce the MER results
2135 with a total exposure time of about 20 minutes (possible in 4 images). Although the wide field of
2136 view ($124^\circ \times 124^\circ$) of the ICC camera offers a larger view of the sky above the horizon, it is
2137 fixed mounted to the lander, nominally pointing to the south and only includes low elevations
2138 due to aiming for workspace context. The arm-mounted IDC offers the possibility of aiming
2139 based on predicted meteor radiants, as well as aiming at elevations with less extinction in dusty
2140 times.

2141
2142 Cosmic ray hits are an important source of confusion for meteoroid detection imaging campaigns
2143 (e.g., Domokos et al., 2007). We will attempt to identify cosmic rays by exploiting the fact that
2144 cosmic rays have no optical point spread function (PSF) as they deposit their energy directly on
2145 the detector (effectively bypassing the camera optics), while meteor trails are imaged through the
2146 lens system and thus have an optical PSF. We note that, instead of discriminating against cosmic
2147 rays via their PSFs, Domokos et al. (2007) relied on pairs of images using two filters of very
2148 different sensitivity, and found no paired detections and statistically equivalent distributions of
2149 streaks between the two images; they could not specifically rule out faint streaks in the sensitive
2150 L1 images if the streaks would not have been detectable in the paired image. Another method to
2151 rule out cosmic rays might be to perform simultaneous observations with two separate cameras,
2152 such as InSight together with MER or MSL. However, such a joint campaign would take
2153 significant multi-mission resources.

2154
2155 The Impacts Science Theme Group intends to submit Science Activity Requests to first
2156 characterize the meteoroid background and then concentrate imaging campaigns on times when
2157 the meteoroid flux is expected to be highest (see Table 5). We will use groups of long exposures,
2158 with the exposure length chosen to optimize the detectability of potential meteoroids in light of

2159 dark current, read noise, system sensitivity, and cosmic ray flux. Based on the camera sensitivity
2160 compared to Pancam, we anticipate that a notional sequence that obtains 20 minutes of
2161 integration time over 4-7 images would typically see 1-3 background meteors and require 16-28
2162 Mb of downlink. It is not yet certain whether enough power and data volume will be available
2163 for such an imaging campaign to be feasible.
2164
2165

2166 **8 IMPACT CHARACTERIZATION AND ANALYSIS PLANS**

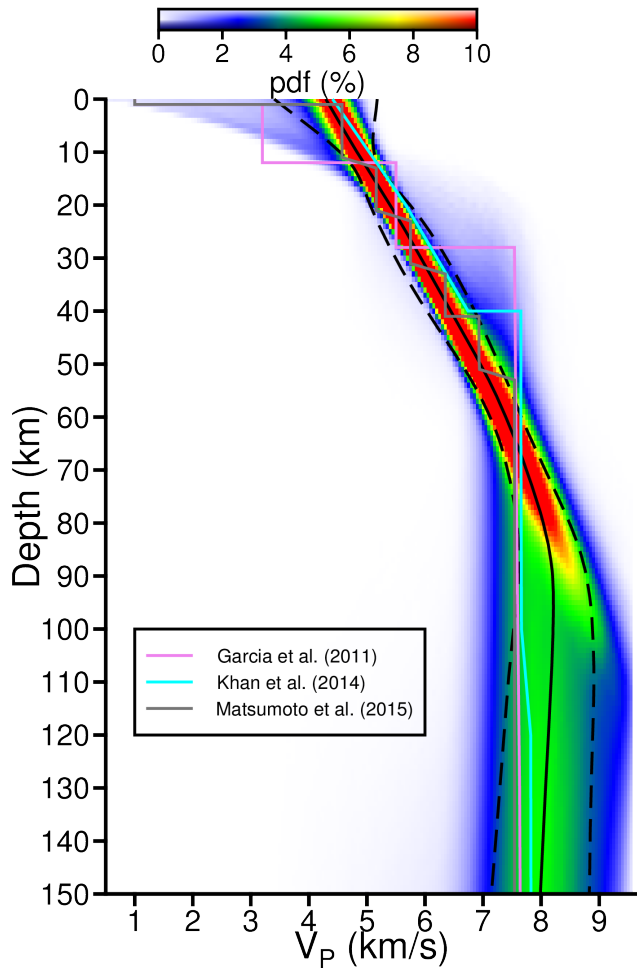
2167 **8.1 VALIDATING INTERIOR STRUCTURE MODELS**

2168 In the framework of the InSight mission, impacts will be located by one of several orbiting
2169 cameras, which will provide a known location. This will enable the direct inversion of all
2170 differential travel times with respect to P arrival times. If we have epicentral distance and origin
2171 time and are able to identify body wave phase arrival times, we have enough information to
2172 perform body wave travel times inversion for one dimensional crust and mantle velocity
2173 structure along the ray path, using very minimal *a priori* information. The known location of an
2174 impact will enable this analysis, compared to marsquakes that will have much less well-
2175 constrained locations.
2176
2177

2178 To test how well an inversion can resolve structure using a limited dataset of only a few impact
2179 events, we first invert for the P-wave velocity profile of the Moon using the travel times from
2180 artificial impacts acquired by the Apollo 12 station. The artificial events were generated by the
2181 impact of the Lunar Modules and the upper stage S-IVB of the Saturn V rockets with the lunar
2182 surface, and most of these impacts correspond to relatively short epicentral distances ($\Delta < 300$
2183 km). Our study uses 6 artificial impacts for which dates, locations and arrival times can be found
2184 in Table 1 of Lognonné et al. (2003). For each ray path, the first P wave arrival is considered.
2185 The reading error attributed to the arrival time estimates is 1 s. Second, to characterize what we
2186 could learn about Mars interior structure with only one station, we performed several inversions
2187 using a synthetic Martian seismic model, and impacts occurring at different epicentral distances.
2188 The Martian model is derived from the Dreibus-Wänke mineralogy profile (Dreibus and Wanke,
2189 1985) using the ‘hot’ end-member temperature profile of Plesa et al. (2016).
2190
2191

2192 The inverse problem consists in a Markov chain Monte Carlo approach, which forms the basis
2193 for most of the planned modeling of the Mars Structure Service (MSS) (Panning et al., 2017).
2194 This technique allows us to investigate a large range of possible models and provides a
2195 quantitative measure of the models’ uncertainty and non-uniqueness. The algorithm that we use
2196 is explained in Drilleau et al. (2013) and Panning et al. (2015, 2017). The reader is referred to
2197 these papers for further details on the practical implementation of the method. The
2198 parameterization is done with Bézier points (Bézier, 1966, 1967), which are interpolated with C^1
2199 Bézier curves. The advantages of such a parameterization are that it relies on a small number of
2200 parameters that do not need to be regularly spaced in depth, and it can be used to describe both
2201 gradients and sharp interfaces. The forward problem consists in a basic ray tracing algorithm
2202 (e.g. Shearer, 2009). The priors on the parameters are uniformly distributed over wide domains.
2203 We chose to invoke as few prior constraints as possible to gauge which particular feature is most
2204 probable.

2205
2206 The results of the Apollo data inversion are shown in Fig. 34. The plot is a probability density
2207 function (PDF) of the accepted models. The v_p profile is well defined down to 150 km depth but
2208 not deeper, due to the short epicentral distances where the artificial impacts occurred. The
2209 maximum of the PDF shows a v_p gradient down to 80 km depth. Below this depth the profile has
2210 a constant value of ~ 8.1 km/s. The change in slope could be interpreted as the base of the crust.
2211 However, this interpretation must be taken with care because here the depth of an interface is not
2212 strictly a model parameter but a useful feature that can be picked in any sampled model. Within
2213 the 80-100 km depth interval, we observe a trade-off between the depth of the slope change and
2214 the v_p value. This trade-off means, unsurprisingly, that the data fit equally well when the crust-
2215 mantle boundary is deeper and v_p is higher, or *vice-versa*. Note that the secondary arrivals, which
2216 are very sensitive to sharp interfaces, were picked with very large uncertainties on Apollo data.
2217 This was due to the intense scattering in the low-velocity, high-Q upper crust (Dainty et al.,
2218 1974) which led to a prolonged, incoherent signal after the initial P arrival. Without the use of
2219 such phases, we can only constrain a smooth averaged profile. For comparison, previously
2220 published Moon internal structure models of Garcia et al. (2011), Khan et al. (2014) and
2221 Matsumoto et al. (2015) are represented in Fig. 34. These three models are made with a layered
2222 parameterization. With the exception of the two crustal interfaces of Garcia et al. (2011)'s model
2223 and the crust-mantle boundary of Khan et al. (2014)'s model, the three profiles matches well
2224 with our recovered v_p distribution within the 1σ uncertainty. Note that between 20 and 50 km
2225 depth, several models show a discontinuity, as shown by the extension of the lower probability
2226 blue region of the PDF to higher velocities in this depth range. They are not the most probable
2227 models, but they are also able to explain the data within their uncertainty bounds.
2228



2229

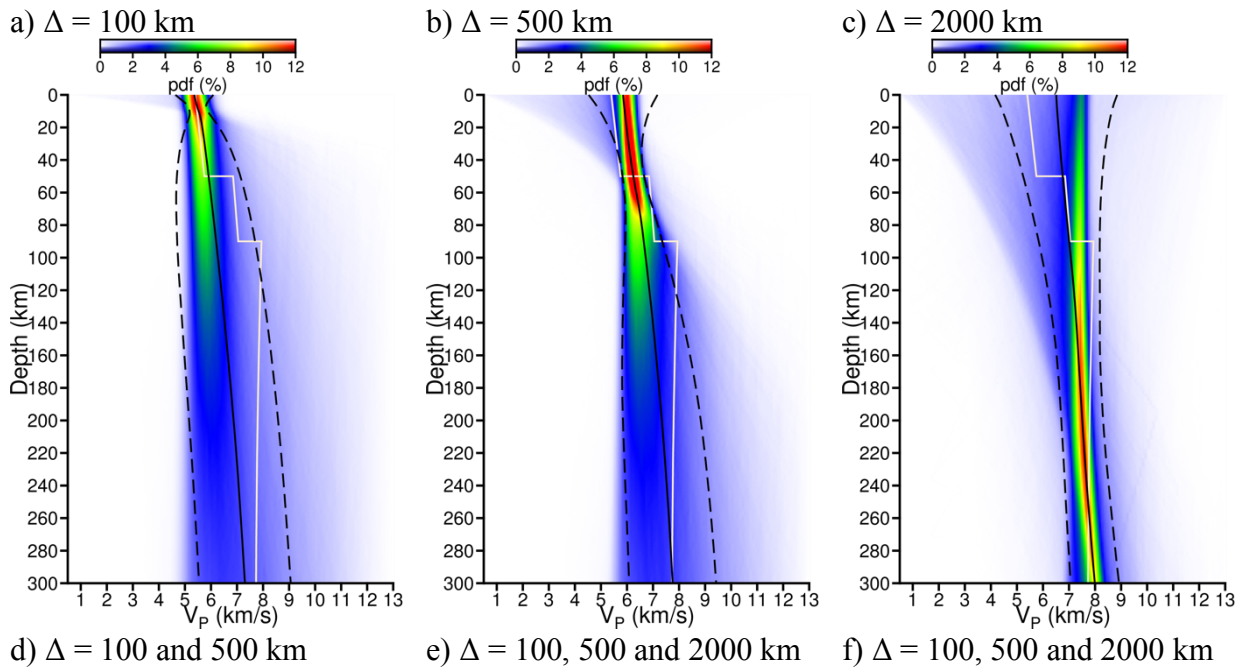
2230 *Figure 34:*

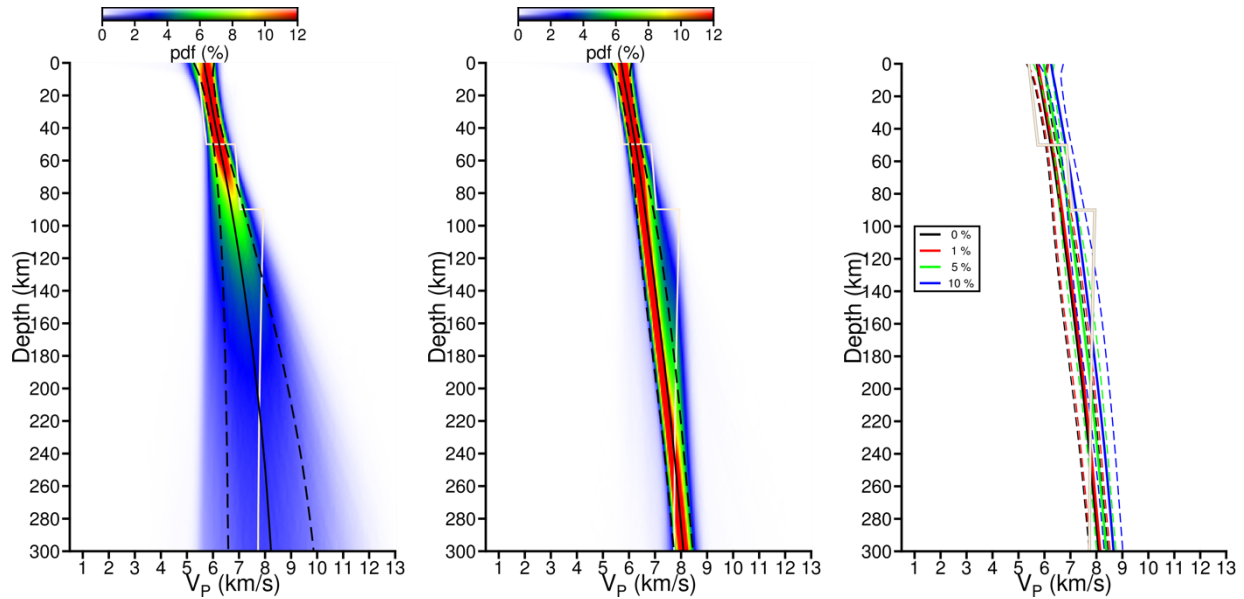
2231 *Inversion results using travel times from artificial impacts on the Moon recorded at Apollo 12*
 2232 *station. Red and blue colors show high and low probability density function (PDF), respectively.*
 2233 *The black line is the median profile of the v_p distribution as a function of depth, and the black*
 2234 *dashed lines represent the interval between $\pm 1\sigma$ standard deviation. Previously published Moon*
 2235 *internal structure models of Garcia et al. (2011), Khan et al. (2014) and Matsumoto et al. (2015)*
 2236 *are shown for comparison.*

2237

2238 The results of the inversion of synthetic P waves travel times to retrieve Mars interior structure
 2239 are presented in Fig. 35. Once the InSight lander is operational on Mars, the strategy will be to
 2240 iteratively improve the interior model as more data becomes available. Considering the case at
 2241 the beginning of the mission, we first show a pessimistic scenario where we investigate what
 2242 could be retrieved using a single impact event, located at $\Delta = 100$ km, 500 km and 2000 km (Fig.
 2243 35a, 35b and 35c). The reading errors are considered to be 1 s, 2.5 s and 5 s, respectively. In the
 2244 three cases, the PDFs are the highest and the 1σ uncertainties are the lowest at the depths of the
 2245 turning point of the ray paths. These depths are approximately 5 km, 55 km and 200 km for $\Delta =$
 2246 100 km, 500 km and 2000 km, respectively. The mode of the distributions and the medians
 2247 (black lines in Fig. 35) match the input model (white lines in Fig. 35) well at these depths. We
 2248 also consider a more optimistic scenario likely later in the mission, where we record several
 2249 impact events located at different epicentral distances. This produces a dataset sensitive to the

2250 structure at different depths. Fig. 35d and 35e show the inversion results for two impact events
 2251 located at $\Delta = 100$ km and 500 km, and three impacts events located at $\Delta = 100$ km, 500 km and
 2252 2000 km, respectively. In Fig. 35d, we observe that the combination of the two events at $\Delta = 100$
 2253 km and 500 km gives a better estimation of the v_p profile from the surface down to 35 km depth,
 2254 compared to the inversion of the $\Delta = 500$ km event alone. With this combination, the model is
 2255 retrieved down to 80 km depth. Below this depth, the PDF is broader due to the lack of
 2256 sensitivity of the data. If a third impact with a larger epicentral distance is added (Fig. 35e), the
 2257 PDF is tightly constrained down to 300 km depth. As for the Moon (Fig. 34), the median profile
 2258 we obtained is smooth compared to the input model, because of the lack of secondary arrivals.
 2259 However, the PDF is broadened between 80 and 140 km depth, which indicates a potential
 2260 change in slope. The good agreement between synthetic and tested data shows here a clear
 2261 potential to resolve a first order velocity structure of the Martian crust and mantle, using P wave
 2262 arrival times of impacts at known locations.
 2263





2264

2265 *Figure 35:*

2266 *Results of v_p probabilistic inversions using travel times computed for a Martian synthetic model.*
 2267 *(a), (b) and (c) show the results performed using only one travel time generated by a single*
 2268 *impact, for an epicentral distance of $\Delta = 100$ km, $\Delta = 500$ km and $\Delta = 2000$ km, respectively. (d)*
 2269 *and (e) show the distributions obtained using 2 impacts at $\Delta = 100$ and 500 km, and 3 impacts at*
 2270 *$\Delta = 100$, 500 and 2000 km, respectively. Red and blue colors show high and low probability*
 2271 *density functions (PDF), respectively. The black line is the median profile of the v_p distribution*
 2272 *as a function of depth, and the black dashed lines represent the interval between $\pm 1\sigma$ standard*
 2273 *deviation. The white line is the synthetic model that was input. (f) shows the median and the $\pm 1\sigma$*
 2274 *standard deviation of the v_p distribution when the error on Δ is equal to 0, 1, 5 and 10%.*

2275

2276 We also investigated to what extent the error on the location would affect the inversion's result.
 2277 As an example, Fig. 35f shows the median v_p profile and the 1σ uncertainties, considering an
 2278 error of 0%, +1%, +5%, and +10% on the locations of the three impacts. To compensate for the
 2279 larger epicentral distances, the v_p values are higher than in the case where the true epicentral
 2280 distance is used (black lines). Errors of +1%, +5%, and +10% on the locations lead to a v_p
 2281 increase between 0.050-0.074 km/s, 0.27-0.33 km/s, and 0.55-0.60 km/s, respectively.
 2282 Consequently, neglecting the complexities of the three-dimensional structure, we consider that
 2283 the Level 1 requirement, which is to determine the seismic velocities in the upper 600 km of the
 2284 mantle to within ± 0.5 km/s, is met when the error on the epicentral distance is less than $\sim 10\%$.
 2285 Low location errors such as these will easily be achievable with impacts that are successfully
 2286 imaged from orbit.

2287

2288 Another benefit of superficial events such as impacts is that inversions such as this can be used
 2289 to constrain the crustal thickness at the impact site. In seismic investigations of crustal thickness
 2290 such as Chenet et al. (2006), the best-constrained location will be the crustal thickness below the
 2291 seismic station, in this case at the InSight landing site. Because the seismic signals from craters
 2292 also penetrate through the crust at the impact site, the data can also be used to constrain the

2293 crustal thickness there. This will yield additional constraints for lateral variation of the crustal
2294 thickness.

2295

2296 **8.2 MEASURING IMPACT-SEISMIC EFFICIENCY**

2297

2298 Impact-seismic coupling is one of the key aspects in understanding impacts as a seismic source.
2299 The seismic efficiency k , is not well constrained, with values in the literature ranging from 10^{-6}
2300 to 10^{-2} (see Section 3.3 for discussion). Given that no artificial impact is expected during the
2301 duration of the InSight mission, we will not be able to calibrate seismic efficiency directly in the
2302 way Apollo boosters were used (e.g. Latham et al., 1970a). On the other hand, we will be
2303 searching for craters associated with seismic events to obtain image data for each impact. This
2304 will give us a relationship between crater sizes and seismic energy. The relationship between
2305 crater size and impact energy is relatively well known (e.g. Holsapple, 1993; Section 4.4), and
2306 thus we will be able to indirectly evaluate the seismic efficiency.

2307

2308 To precisely evaluate seismic efficiency, sufficient knowledge of the attenuation of Mars is
2309 needed. Attenuation is expressed by a quality factor Q . The Q value of Mars will be evaluated
2310 through spectral analyses of seismic signals as an activity of the Mars Structure Service (Panning
2311 et al., 2017). We will be referring to their model for the correction.

2312

2313 **8.4 MEASURING IMPACTOR SIZE FREQUENCY DISTRIBUTION**

2314

2315 If sufficient impacts can be detected seismically and imaged in high resolution to resolve their
2316 diameters, a measurement of the current impact rate can be made. The impact flux (number of
2317 craters of a given size per area, per time) will need to be corrected for the distance at which any
2318 given crater diameter is detectable to SEIS. Estimates of these detection limits are discussed in
2319 Section 6, but will need to be updated with the real performance of the seismometer on the
2320 ground at Mars. For example, noise levels at the time of writing can be estimated, but these will
2321 not be known with certainty until operation of the seismometer on the surface of Mars. Noise
2322 levels will most likely vary with time of day, being lower at night when thermal noise is lower
2323 (Murdoch et al. 2017). Another potential observational bias is reduced detections of clustered
2324 impacts (Section 4.5.1), which comprise half the known impact events at Mars currently (Daubar
2325 et al., 2013). These biases will need to be taken into account in the ultimate detection rate
2326 calculation. This measurement of the impact flux will be independent of previous measurements
2327 that were based on orbital images.

2328

2329 **8.5 MORPHOLOGIC STUDY OF NEW CRATERS**

2330

2331 Images of new craters detected seismically will be used to accurately determine the impact
2332 location in longitude and latitude, then converted to offset and azimuth with respect to the
2333 location of the SEIS instrument. Once the exact location of the new crater is identified, requests
2334 for stereo data will be sent to HiRISE on MRO and CaSSIS on TGO. If stereo images can be
2335 obtained, a digital topographic model (DTM) will be created over the area of interest. This can
2336 be accomplished using several photogrammetric applications including SOCET SET (Kirk et al.,
2337 2003) and Ames Stereo Pipeline (Shean et al., 2016). An estimation of the DTM uncertainties
2338 will be performed, similarly to error analysis done for terrestrial data (e.g., Lucas et al., 2015).

2339
2340 If the crater(s) are large enough to be resolved in the data, high resolution images and DTMs will
2341 permit several analyses. Images alone will yield a measurement of the crater diameter. Three-
2342 dimensional analysis of DTMs will provide the depth, diameter, and excavated crater volume.
2343 (Rim height is unlikely to be resolvable, if it is even significant, for these craters.) If DTMs are
2344 unavailable or cannot resolve the craters, shadow length measurements can be done to measure
2345 the crater depth with less precision (e.g. Daubar et al., 2014). Ejected material and blast zones
2346 can be characterized in visible images (spatial extension, directivity) (e.g. Daubar et al., 2016).
2347 However, directional blast zones indicating the direction of impact are rare (Daubar et al., 2018).
2348 The ejecta is unlikely to be resolved at this scale, thus volume measurements of ejecta will not be
2349 likely. If present as a cluster, the geospatial characteristics of the cluster can be studied to reveal
2350 impact direction and angle (Daubar et al., 2017; 2018). Characterization of the new craters'
2351 morphology and ejecta, together with seismic analyses, may eventually allow an evaluation of
2352 the impact velocity and direction, impact energy, the mass of impactor, and the porosity of the
2353 impacted sub-surface. Geological maps of the area bracketing the position of SEIS and the new
2354 crater will also be used to assess the geological context (type and age of the terrains, crustal
2355 thickness, regolith depth, etc.) of the impact area and the terrains where waves propagated. The
2356 exact location of the impact, the impact direction and energy, and estimation of the sub-surface
2357 porosity will help interpret the seismogram recorded by SEIS, including amplitude and arrival
2358 time, and constrain lithosphere and regolith models for wave propagation (Section 8.1).

2359
2360

2361 **9 CONCLUSIONS**

2362
2363 Detecting and studying impacts with Insight will be a challenge, but the wealth of information
2364 they will provide about Mars make this a worthwhile pursuit. We will use impacts to achieve the
2365 mission goals of measuring the current impact rate at Mars, and also to illuminate the interior
2366 structure. A known source location, something that tectonic seismic sources will most likely not
2367 be able to accomplish, will enable calibration of the models used to interpret all seismic signals,
2368 from marsquakes as well as from impacts. Several impact-specific parameters will be
2369 constrained with real data, for example, the source time function (Section 3.1) and cutoff
2370 frequency (Section 3.2). The relationship between the cutoff frequency and impact momentum
2371 will be assessed using a known crater size that can be connected to impactor momentum. We
2372 will also be able to measure the seismic efficiency (Section 3.3), using scaling relationships
2373 associating the size of the crater to the impact energy. We will then be able to evaluate the
2374 accuracy of our preferred value for the Martian seismic efficiency, 5×10^{-4} .

2375
2376 We have predicted the frequency of impacts (Section 6.2) and the seismic response of Mars
2377 (Section 5.2) based on our observations of terrestrial (Section 2.1), lunar (Section 2.2), and
2378 experimental impacts (Section 3.4). However, the true Martian seismic properties such as
2379 seismic efficiency, seismic attenuation, and subsurface velocity structure will not be known until
2380 we reach Mars, detect an impact seismically, and calibrate our estimates with orbital images.
2381 Enough such detections will also achieve one of the scientific goals of the InSight mission, to
2382 measure the impact flux at Mars. This independent measurement of the current impact rate will
2383 be free of the biases in previous measurements done using orbital images alone, help us to better
2384 understand the chronology of Mars, and clarify the impact hazard to future exploration. Based on

2385 current estimates of the Martian impact rate, we predict this measurement will be possible within
2386 the timeframe of the prime mission (one Mars year) with the detection of ~a few to several tens
2387 of impacts. Similar measurements of the airburst frequency may also be possible to compare to
2388 the predictions we present here (Section 4.5.2). Detection of impact-induced acoustic waves may
2389 be possible as well (Section 4.5.3).

2390
2391 The modeling codes to be used in analysis of the seismic signals from impacts have been
2392 benchmarked, and we endorse them for use in future work (Section 5). We outlined the processes
2393 the InSight Impacts Science Theme Group will follow during mission operations to discriminate
2394 impacts from marsquakes (Section 6.1); follow up on impact seismic detections (Section 7.1);
2395 request event data and orbital images (Section 7.2); search those images for the impact site
2396 (Sections 7.2.2 and 7.2.3); and finally analyze those data (Section 8). A plan for possible night-
2397 time meteor imaging is also presented (Section 7.3); this valuable, but not required, experiment
2398 would provide a direct measurement of the small end of the size distribution of the Martian
2399 impact flux.

2400
2401 Using data from InSight, these analyses will lead to better understanding of the shallow
2402 subsurface structure, physical and seismic properties of the interior, the seismic efficiency and
2403 other seismic-impact parameters, and the current impact flux at Mars.

2404
2405

2406 **ACKNOWLEDGEMENTS**

2407 We are grateful to Jay Melosh and an unnamed reviewer for thoughtful and helpful comments.
2408 We appreciate the hard work of the engineering and operations teams who are making the
2409 InSight mission possible. Elizabeth Barrett provided valuable input. Thank you to Matthew
2410 Siegler for helping to address a reviewer comment. A portion of this research was carried out at
2411 the Jet Propulsion Laboratory, California Institute of Technology, under a contract with the
2412 National Aeronautics and Space Administration. French co-authors thank the support of the
2413 French Space Agency CNES as well as ANR SIMARS. IPGP coauthors (IPGP contribution
2414 number 3988) also received support from the UnivEarth Labex at Sorbonne Paris Cité (ANR-10-
2415 LABX-0023 and ANR-11-IDEX-0005-02). N. Teanby and J. Wookey are funded by the UK
2416 Space Agency. Swiss co-authors recognize the support of the (1) Swiss National Science
2417 Foundation and French Agence Nationale de la Recherche (SNF-ANR project 157133
2418 “Seismology on Mars”) and (2) Swiss State Secretariat for Education, Research and Innovation
2419 (SEFRI project “MarsQuake Service—Preparatory Phase”). We gratefully acknowledge the
2420 developers of the iSALE hydrocode. A portion of this work was performed using HPC resources
2421 of CINES (Centre Informatique National de l’Enseignement Supérieur) under the
2422 allocation A0030407341 made by GENCI (Grand Equipement National de Calcul Intensif). KM
2423 research is fully supported by the Australian Government (project numbers DE180100584 and
2424 DP180100661). This is InSight Contribution Number 47.

2425
2426
2427

2428

REFERENCES

- 2429 Aki, K. and P. G. Richards (2002) Quantitative Seismology, 2nd Ed. Published by University
2430 Science Books, ISBN 0-935702-96-2, 704pp.
- 2431 Anderson, D. L., Duennebier, F. K., Latham, G. V, Toksöz, M. F., Kovach, R. L., Knight, T. C.,
2432 ... Sutton, G. (1976). The viking seismic experiment. *Science (New York, N.Y.)*,
2433 194(4271), 1318–21. doi:10.1126/science.194.4271.1318
- 2434 Artemieva N., and E. Pierazzo (2009) The Canyon Diablo impact event: Projectile motion
2435 through the atmosphere, *Meteorit. Planet. Sci.* 44, Nr. 1, 25-42.
- 2436 Baldwin B. and Y. Sheaffer. Ablation and breakup of large meteoroids during atmospheric entry.
2437 *Journal of Geo- physical Research*, 76(19):4653–4668, 1971.
- 2438 Banerdt, W. B. et al. (2018) “The InSight Mission”, this issue.
- 2439 Banerdt, W. B., Smrekar, S. E., Hoffman, T., Spath, S., Lognonné, P., Spohn, T., , H. Stone, J.
2440 Willis, J. Feldman, R. De Paula, R. Turner, S. Asmar, D. Banfield, U. Christensen, J.
2441 Clinton, V. Dehant, W. Folkner, R. Garcia, D. Giardini, M. Golombek, M. Grott, T.
2442 Hudson, C. Johnson, G. Kargl, B. Knapmeyer-Endrun, J. Maki, D. Mimoun, A. Mocquet,
2443 P. Morgan, M. Panning, W. T. Pike, C. Russell, N. Teanby, J. Tromp, R. Weber, M.
2444 Wieczorek, K. Hurst, E. Barrett, and the InSight Team. (2017). The InSight Mission for
2445 2018. *Lunar & Planetary Science Conference 48*, abstract 1896.
- 2446 Banerdt, W.B., Smrekar, S., Lognonné, P., Spohn, T., Asmar, S.W., Banfield, D., Boschi, L.,
2447 Christensen, U., Dehant, V., Folkner, W., Giardini, D., Goetze, W., Golombek, M., Grott,
2448 M., Hudson, T., Johnson, C., Kargl, G., Kobayashi, N., Maki, J., Mimoun, D., Mocquet,
2449 A., Morgan, P., Panning, M., Pike, W.T., Tromp, J., van Zoest, T., Weber, R., Wieczorek,
2450 M.A., Garcia, R., Hurst, K. (2013). InSight: A Discovery Mission to Explore the Interior
2451 of Mars, in *Lunar and Planetary Science Conference*, Lunar and Planetary Inst. Technical
2452 Report, 44, p. 1915.
- 2453 Banks, Maria E., Ingrid J. Daubar, N. C. Schmerr, and Matthew P. Golombek. 2015. “Predicted
2454 Seismic Signatures of Recent Dated Martian Impact Events: Implications for the InSight
2455 Lander.” *Lunar and Planetary Science Conference 46*, Abstract 2679.
- 2456 Bart, Gwendolyn D., and P. L. Spinolo. 2013. “Formation of Airblast Features Associated with
2457 Young Martian Craters.” *Geological Society of America Abstracts with Programs*. Vol. 45,
2458 No. 7, Paper No. 200-10.
- 2459 Bass, Henry E., and James P. Chambers. 2001. “Absorption of Sound in the Martian
2460 Atmosphere.” *The Journal of the Acoustical Society of America* 109, 2371–2371.
2461 doi:10.1121/1.4744345.

- 2462 Becker, K.J., et al. (2013) ISIS Support for NASA Mission Instrument Ground Data Processing
2463 Systems, Lunar Planet. Sci. XLIV, Houston, Texas, Abstract #2829.
- 2464 Bell, J. F., Wolff, M. J., Malin, M. C., Calvin, W. M., Cantor, B. A., Caplinger, M. a., ...
2465 Thomas, P. C. (2009). Mars Reconnaissance Orbiter Mars Color Imager (MARCI):
2466 Instrument description, calibration, and performance. *Journal of Geophysical Research*,
2467 *114*(E8), E08S92. <http://doi.org/10.1029/2008JE003315>
- 2468 Ben-Menahem, Ari. 1975. "Source Parameters of the Siberian Explosion of June 30, 1908, from
2469 Analysis and Synthesis of Seismic Signals at Four Stations." *Physics of the Earth and*
2470 *Planetary Interiors* 11 (1): 1–35. doi:10.1016/0031-9201(75)90072-2.
- 2471 Bézier P., Définition numérique des courbes et surfaces I. *Automatisme* 11, 625–632 (1966)
- 2472 Bézier P., Définition numérique des courbes et surfaces II. *Automatisme* 12, 17–21 (1967)
- 2473 Böse, M., Clinton, J., Ceylan, S., Euchner, F., van Driel, M., Khan, A., Giardini, D., Lognonné,
2474 P. and Banerdt, W.B. (2017). A probabilistic framework for single-station location of
2475 seismicity on Earth and Mars, *Phys. Earth Planet. Inter.* 262, 48-65, doi:
2476 10.1016/j.pepi.2016.11.003.
- 2477 Böse, M., D. Giardini, S. Stähler, S. Ceylan, J. Clinton, M. van Driel, A. Khan, F. Euchner, P.
2478 Lognonné, B. Banerdt (in review). Magnitude Scales for Marsquakes.
- 2479 Brown, P. G., Assink, J. D., Astiz, L., Blaauw, R., Boslough, M. B., Borovic'ka, J., Brachet, N.,
2480 Brown, D., Campbell-Brown, M., Ceranna, L., et al., 2013. A 500-kiloton airburst over
2481 Chelyabinsk and an enhanced hazard from small impactors. *Nature* 503, 238–241.
- 2482 Brown, P., ReVelle, D. O., Silber, E. A., Edwards, W. N., Arrowsmith, S., Jackson, L. E.,
2483 Tancredi, G., Eaton, D., 2008. Analysis of a crater-forming meteorite impact in Peru. *J.*
2484 *Geophys. Res.* 113, E09007.
- 2485 Burleigh K. J., Melosh H. J., Tornabene L. L., Ivanov B., McEwen A. S., and Daubar I. J. 2012.
2486 Impact airblast triggers dust avalanches on Mars. *Icarus* 217: 194-201
- 2487 Chenet, H., Lognonné, P., Wiczorek, M. A., & Mizutani, H. (2006). Lateral variations of lunar
2488 crustal thickness from the Apollo seismic data set. *Earth and Planetary Science Letters*,
2489 *243*, 1–14. doi:10.1016/j.epsl.2005.12.017
- 2490 Christensen, P.R., B.M. Jakosky, H.H. Kieffer, M.C. Malin, H.Y. McSween, Jr., K. Nealson,
2491 G.L. Mehall, S.H. Silverman, S. Ferry, M. Caplinger, and M. Ravine, The Thermal
2492 Emission Imaging System (THEMIS) for the Mars 2001 Odyssey Mission, *Space Science*
2493 *Reviews*, 110, 85-130, 2004.
- 2494 Christensen, Phillip R., E Engle, S Anwar, S Dickenshied, D Noss, N Gorelick, and M Weiss-
2495 Malik. 2009. "JMARS - A Planetary GIS." *American Geophysical Union Fall Meeting*,
2496 IN22A-06.

- 2497 Chyba C. F., P. J. Thomas, and K. J. Zahnle. The 1908 tunguska explosion: atmospheric
2498 disruption of a stony asteroid. *Nature*, 361(6407):40–44, 1993.
- 2499 Clévéde, Éric, Lognonné, Philippe. (2003). 85.16 Higher order perturbation theory: 3D synthetic
2500 seismogram package. *International Geophysics*. 81. 1639-1639. doi: 10.1016/S0074-
2501 6142(03)80295-4.
- 2502 Clinton. et al., 2018, "Marsquake Service - building a Martian seismicity catalogue for InSight",
2503 this issue.
- 2504 Collins, G.S., Melosh, H.J. and Marcus, R.A., 2005. Earth Impact Effects Program: A Web-
2505 based computer program for calculating the regional environmental consequences of a
2506 meteoroid impact on Earth. *Meteoritics & planetary science*, 40(6), pp.817-840.
- 2507 Dainty A. M., M. N. Toksz, K. R. Anderson, P. J. Pines, Y. Nakamura, and G. Latham, Seismic
2508 scattering and shallow structure of the Moon in Oceanus Procellarum. *Moon* 9, 11- 29,
2509 1974.
- 2510 Daubar, I. J., A. S. McEwen, S. Byrne, M. R. Kennedy, and B. Ivanov (2013) The current
2511 Martian cratering rate. *Icarus* 225, 506-516. doi: 10.1016/j.icarus.2013.04.009
- 2512 Daubar, I. J., C. Atwood-Stone, S. Byrne, A. S. McEwen, and P. S. Russell (2014), The
2513 morphology of small fresh craters on Mars and the Moon, *J. Geophys. Res. Planets*, 119,
2514 2620– 2639, doi:10.1002 / 2014JE004671.
- 2515 Daubar, I. J., Dundas, C. M., Byrne, S., Geissler, P. E., Bart, G. D., McEwen, A. S., ...
2516 Chojnacki, M. (2016). Changes in Blast Zone Albedo Patterns Around New Martian
2517 Impact Craters. *Icarus*, 267, 86–105. doi:10.1016/j.icarus.2015.11.032
- 2518 Daubar, I. J., Golombek, M. P., McEwen, A. S., Byrne, S., Kreslavsky, M. a., Schmerr, N. C., &
2519 Banks, M. E. (2015). Measurement of the current Martian cratering size frequency
2520 distribution, predictions for and expected improvements from InSight. *Lunar and*
2521 *Planetary Science Conference Abstracts*, Abs. 2468.
- 2522 Daubar, I. J., M. E. Banks, N. C. Schmerr, and M. P. Golombek (2018) “Recently Formed Crater
2523 Clusters on Mars, in prep.
- 2524 Davis, D. M., 1993. Meteoroid impacts as seismic sources on Mars 105, 469–478.
- 2525 Delage, P., Karakostas, F., Dhemaied, A., Belmokhtar, M., Lognonné, P., Golombek, M., De
2526 Laure, E., Hurst, K., Dupla, J.-C., Kedar, S., Cui, Y. J., and Banerdt, B., 2017, An
2527 investigation of the mechanical properties of some Martian regolith simulants with
2528 respect to the surface properties at the InSight mission landing site: *Space Science*
2529 *Reviews*, v. 211, p. 191-213, DOI 10.1007/s11214-017-0339-7.
- 2530 Domokos, A., J. F. Bell III, P. Brown, M.T. Lemmon, R. Suggs, J. Vaubaillon and W. Cook,
2531 2007. Measurement of the Meteoroid Flux at Mars. *Icarus* **191**, 141-150,
2532 doi:10.1016/j.icarus. 2007.04.017.

- 2533 Dreibus G., H. Wänke, Mars: a volatile rich planet. *Meteoritics* 20, 367–382 (1985)
- 2534 Drilleau M., E. Beucler, A. Mocquet, O. Verhoeven, G. Moebs, G. Burgos, J.P. Montagner, P.
2535 Vacher, A Bayesian approach to infer radial models of temperature and anisotropy in the
2536 transition zone from surface wave dispersion curves. *Geophys. J. Int.* 195, 1165–1183
2537 (2013)
- 2538 Edwards, C. S., K. J. Nowicki, P. R. Christensen, J. Hill, N. Gorelick, and K. Murray (2011),
2539 Mosaicking of global planetary image datasets: 1. Techniques and data processing for
2540 Thermal Emission Imaging System (THEMIS) multi-spectral data, *J. Geophys. Res.*, 116,
2541 E10008, doi:10.1029/2010JE003755
- 2542 Edwards, W. N., Eaton, D. W., Brown, P. G., 2008. Seismic observations of meteors: coupling
2543 theory and observations. *Rev. Geophys.* 46, 2007RG000253.
- 2544 Friederich, W. and J. Dalkolmo (1995) Complete synthetic seismograms for a spherically
2545 symmetric Earth by a numerical computation of the Green's function in the frequency
2546 domain. *Geophysical Journal International* 122, 537-550. doi:10.1111/j.1365-
2547 246X.1995.tb07012.x
- 2548 Gagnepain-Beyneix, Jeannine, Philippe Lognonné, Hugues Chenet, Denis Lombardi, and Tilman
2549 Spohn. 2006. “A Seismic Model of the Lunar Mantle and Constraints on Temperature and
2550 Mineralogy.” *Physics of the Earth and Planetary Interiors* 159 (3–4): 140–66.
2551 doi:10.1016/j.pepi.2006.05.009.
- 2552 Garcia R.F., J. Gagnepain-Beyneix, S. Chevrot, P. Lognonné, Very preliminary reference Moon
2553 model. *Physics of the Earth and Planetary Interiors* 188, 96–113 (2011).
2554 doi:10.1016/j.pepi.2011.06.015
- 2555 Garcia, Raphael F., Quentin Brissaud, Lucie Rolland, Roland Martin, Dimitri Komatitsch,
2556 Aymeric Spiga, Philippe Lognonné, and William Bruce Banerdt. 2017. “Finite-Difference
2557 Modeling of Acoustic and Gravity Wave Propagation in Mars Atmosphere: Application to
2558 Infrasounds Emitted by Meteor Impacts.” *Space Science Reviews* 211 (1–4), 547–570.
2559 doi:10.1007/s11214-016-0324-6.
- 2560 Geller R.J. and Takeuchi N., 1995. A new method for computing highly accurate DSM synthetic
2561 seismograms, *Geophys. J. Int.* , 123, 449–470.
- 2562 Geller, J. R., Ohminato, T. (1994) Computation of synthetic seismograms and their partial
2563 derivatives for heterogeneous media with arbitrary natural boundary conditions using the
2564 Direct Solution Method, *Geoph. J. Int.*, 116, 2, 421-446.
- 2565 Gilbert, F. and Dziewonski, A.M. (1975) An application of normal mode theory to the retrieval
2566 of structural parameters and source mechanism from seismic spectra, *Philosophical
2567 Transaction of the Royal Society A*, 278, doi: 10.1098/rsta.1975.0025

- 2568 Gilbert, F. and Dziewonski, A.M. (1975) An application of normal mode theory to the retrieval
2569 of structural parameters and source mechanism from seismic spectra, *Philosophical*
2570 *Transaction of the Royal Society A*, 278, doi: 10.1098/rsta.1975.0025
- 2571 Golombek M., Kipp, D., Warner, N., Daubar, I. J., Fergason, R., Kirk, R., Beyer, R., Huertas, A.,
2572 Piqueux, S., Putzig, N. E., Campbell, B. A., Morgan, G. A., Charalambous, C., Pike, W.
2573 T., Gwinner, K., Calef, F., Kass, D., Mischna, M., Ashley, J., Bloom, C., Wigton, N.,
2574 Hare, T., Schwartz, C., Gengl, H., Redmond, L., Trautman, M., Sweeney, J., Grima, C.,
2575 Smith, I. B., Sklyanskiy, E., Lisano, M., Benardini, J., Smrekar, S., Lognonné, P., and
2576 Banerdt, W. B., 2017, Selection of the InSight landing site: *Space Science Reviews*, 211,
2577 5-95, DOI 10.1007/s11214-016-0321-9.
- 2578 Golombek M.P. et al., Assessment of Mars Exploration Rover landing site predictions. *Nature*
2579 436, 44–48 (2005). doi:10.1038/nature03600
- 2580 Golombek M.P., A.F.C. Haldemann, R.A. Simpson, R.L. Fergason, N.E. Putzig, R.E. Arvidson,
2581 J.F. Bell III, M.T. Mellon, Martian surface properties from joint analysis of orbital, Earth-
2582 based, and surface observations, in *The Martian Surface: Composition, Mineralogy and*
2583 *Physical Properties*. ed. by J.F. Bell III (Cambridge University Press, Cambridge, 2008),
2584 pp. 468–497 Chap. 21
- 2585 Golombek, M. P. et al., 2018, Geology and physical properties investigations by the InSight
2586 lander, *Space Sci. Rev.*, this issue.
- 2587 Golombek, M. P., A revision of Mars seismicity from surface faulting, *Lunar Planet. Sci. Conf.*,
2588 XXXIII, Abstract 1244, 2002
- 2589 Golombek, M. P., W. B. Banerdt, K. L. Tanaka, and D. M. Tralli, A prediction of Mars
2590 seismicity from surface faulting, *Science*, V258, pp. 979-981, 1992
- 2591 Gudkova T., Lognonné Ph., Gagnepain-Beyneix J. 2011. Large impacts detected by the Apollo
2592 seismometers: Impactor mass and source cutoff frequency estimations. *Icarus*, 211, 1049-
2593 1065.
- 2594 Gudkova, T. V., Lognonné, P., Miljković, K., & Gagnepain-Beyneix, J. (2015). Impact cutoff
2595 frequency – momentum scaling law inverted from Apollo seismic data. *Earth and*
2596 *Planetary Science Letters*, 427, 57–65. doi:10.1016/j.epsl.2015.06.037
- 2597 Güldemeister, N., Wünnemann, K., 2017. Quantitative analysis of impact-induced seismic
2598 signals by numerical modeling. *Icarus* 296, 15–27.
- 2599 Gwinner K. et al., The High Resolution Stereo Camera (HRSC) of Mars Express and its
2600 approach to science analysis and mapping for Mars and its satellites. *Planet. Space Sci.*
2601 (2016). doi: 10.1016/j.pss.2016.02.014.
- 2602 Hartmann, W. K. (1966). Martian Cratering. *Icarus*, 5(1–6), 565–576. doi:10.1016/0019-
2603 1035(66)90071-6

- 2604 Hartmann, W. K. (1977). Relative Crater Production Rates on Planets, *276*(1971), 260–276.
- 2605 Hartmann, W. K., & Daubar, I. J. (2017). Martian cratering 11. Utilizing decameter scale crater
2606 populations to study Martian history. *Meteoritics & Planetary Science*, *52*, 493–510.
2607 doi:10.1111/maps.12807
- 2608 Hartmann, W. K., 2005. Martian cratering 8: Isochron refinement and the chronology of Mars.
2609 *Icarus* *174*, 294–320.
- 2610 Hartmann, W. K., Daubar, I. J., Popova, O. P., & Joseph, E. (2017). Martian Cratering 12.
2611 Utilizing Primary Crater Clusters to Study Crater Populations and Meteoroid Properties.
2612 *Meteoritics & Planetary Science*, accepted.
- 2613 Haskell, N. A. (1967) Analytic approximation for the elastic radiation from a contained
2614 underground explosion. *Journal of Geophysical Research* *72*, 2583-2587.
2615 doi:10.1029/JZ072i010p02583
- 2616 Hedlin M.A.H., Stump B.W., Pearson D.C., Yang X. (2002) Identification of Mining Blasts at
2617 Mid- to Far-regional Distances Using Low Frequency Seismic Signals. In: Walter W.R.,
2618 Hartse H.E. (eds) *Monitoring the Comprehensive Nuclear-Test-Ban Treaty: Seismic*
2619 *Event Discrimination and Identification*. Pageoph Topical Volumes. Birkhäuser, Basel.
- 2620 Helmberger, D. C., and Hadley, D. M., Seismic source functions and attenuation from local and
2621 teleseismic observations of the NTS events Jorum and Handley, *Bull. Seis. Soc. Am.*, Vol
2622 *71*. No. 1, pp 51-67, 1981
- 2623 Herrmann, R.B. (2013) Computer programs in seismology: An evolving tool for instruction and
2624 research, *Seism. Res. Lettr.* *84*, 1081-1088, doi:10.1785/0220110096
- 2625 Herrmann, R.B. (2013) Computer programs in seismology: An evolving tool for instruction and
2626 research, *Seism. Res. Lettr.* *84*, 1081-1088, doi:10.1785/0220110096
- 2627 Hills J. G. and M. P. Goda. The fragmentation of small asteroids in the atmosphere. *The*
2628 *Astronomical Journal*, *105*:1114–1144, 1993.
- 2629 Holsapple, K. A. (1993). The scaling of impact processes in planetary sciences. *Annual Review*
2630 *of Earth and Planetary Sciences* *21*, 333–373. doi:10.1146/annurev.earth.21.050193.002001
- 2631 Holsapple, K. A. and R. M. Schmidt (1987) Point source solutions and coupling parameters in
2632 cratering mechanics. *Journal of Geophysical Research* *92*, 6350-6376.
2633 doi:10.1029/JB092iB07p06350
- 2634 Holsapple, K., K.R. Housen (2007) A crater and its ejecta: An interpretation of Deep impact,
2635 *Icarus* *187*, 345--356.
- 2636 Holsapple, K.A. and K.R. Housen (2012) Momentum transfer in asteroid impacts. I. Theory and
2637 scaling, *Icarus* *221*, 875--887.

- 2638 Ivanov BA, Artemieva NA (2002) Numerical modeling of the formation of large impact craters.
 2639 In Koeberl C, MacLeod KG (eds) Catastrophic events and mass extinctions: Impacts and
 2640 beyond. Geological Society of America Special Paper 356: 619-630
- 2641 Ivanov, B. (2001). Mars/Moon cratering rate ratio estimates. *Space Science Reviews*,
 2642 96(February), 87–104. doi:10.1023/A:1011941121102
- 2643 Ivanov, B., D. Deniem, and G. Neukum. Implementation of dynamic strength models into 2d
 2644 hydrocodes: Applications for atmospheric breakup and impact cratering. *International*
 2645 *Journal of Impact Engineering*, 20(1):411– 430, 1997.
- 2646 Ivanov, BA, Henry J. Melosh, and Alfred S. McEwen. 2010. “New Small Impact Craters in High
 2647 Resolution HiRISE Images - III.” *Lunar and Planetary Science Conference Abstracts*,
 2648 abstract 2020.
- 2649 Jaumann R., G. Neukum, T. Behnke, T.C. Duxbury, E. Eichertopf, H. Hoffmann, A.
 2650 Hoffmeister, U. Köhler, K-D. Matz, T.B. McCord, V. Mertens, J. Obserst, R. Pischel, D.
 2651 Reiss, E. Ress, T. Roatsch, P. Saiger, F. Scholten, G. Schwartz, K. Stephan, M. Wählisch,
 2652 the HRSC Co-Investigation Team, The High-Resolution Stereo Camera (HRSC)
 2653 experiment on the Mars Express: instrument aspects and experiment conduct from
 2654 interplanetary cruise through the nominal mission. *Planet. Space Sci.* 55, 928–952 (2007)
- 2655 JeongAhn, Malhotra, The current impact flux on Mars and its seasonal variation, *Icarus*, Volume
 2656 262, p. 140-153., 2015
- 2657 Kawamura, T., P. Lognonné, Y. Nishikawa, and S. Tanaka (2017) Evaluation of deep
 2658 moonquake source parameters: Implication for fault characteristics and thermal state.
 2659 *Journal of Geophysical Research (Planets)* 122, 1487-1504. doi:10.1002/2016JE005147.
- 2660 Kedar, Sharon, Jose Andrade, William Bruce Banerdt, Pierre Delage, Matthew P. Golombek,
 2661 Matthias Grott, Troy Hudson, et al. 2017. “Analysis of Regolith Properties Using Seismic
 2662 Signals Generated by InSight’s HP3 Penetrator.” *Space Science Reviews* 211 (1–4).
 2663 Springer Science+Business Media B.V.: 315–37. doi:10.1007/s11214-017-0391-3.
- 2664 Khan A., J.A.D. Connolly, A. Pommier, J. Noir, Geophysical evidence for melt in the deep lunar
 2665 interior and implications for lunar evolution. *Journal of Geophysical Research: Planets*
 2666 119(10), 2197–2221 (2014). doi:10.1002/2014JE004661.
- 2667 Khan, A., and K. Mosegaard. 2002. “An Inquiry into the Lunar Interior: A Nonlinear Inversion
 2668 of the Apollo Lunar Seismic Data.” *Journal of Geophysical Research* 107 (E6): 5036.
 2669 doi:10.1029/2001JE001658.
- 2670 Khan, A., van Driel, M., Böse, M., Giardini, D., Ceylan, S., Yan, J., Clinton, J., Euchner, F.,
 2671 Lognonné, P., Murdoch, N., Mimoun, D., Panning, M., Knapmeyer, M., & Banerdt,
 2672 W.B., 2016. Single-station and single-event marsquake location and inversion for
 2673 structure using synthetic Martian waveforms, *Phys. Earth Planet Int.*, 258, 28-42,
 2674 doi:10.1016/j.pepi.2016.05.017.

- 2675 Kirk R.L., E. Howington-Kraus, B. Redding, D. Galuszka, T.M. Hare, B.A. Archinal, L.A.
 2676 Soderblom, J.M. Barrett, High-resolution topomapping of candidate MER landing sites
 2677 with Mars Orbiter Camera narrow-angle images. *J. Geophys. Res.* 108 (E12), 29 (2003).
 2678 Doi: 10.1029/2003JE00213
- 2679 Knapmeyer-Endrun, B., Golombek, M. P., and Ohrnberger, M., 2017, Rayleigh wave ellipticity
 2680 modeling and inversion for shallow structure at the proposed InSight landing site in
 2681 Elysium Planitia, Mars: *Space Science Reviews*, v. 211, p. 339-382, DOI:
 2682 10.1007/s11214-016-0300-1.
- 2683 Knapmeyer, M., Oberst, J., Hauber, E., Wählisch, M., Deuchler, C., and Wagner, R., Working
 2684 models for spatial distribution and level of Mars' seismicity, *Jour. Geophys. Res.*, VOL.
 2685 111, E11006, doi:10.1029/2006JE002708, 2006
- 2686 Komatitsch, D., & Vilotte, J. P. (1998). The spectral element method: an efficient tool to
 2687 simulate the seismic response of 2D and 3D geological structures. *Bulletin of the*
 2688 *seismological society of America*, 88(2), 368-392.
- 2689 Latham, G. V., McDonald, W. G., Moore, H. J., 1970b. Missile impacts as sources of seismic
 2690 energy on the moon. *Science* 168, 242–245.
- 2691 Latham, G., Ewing, M., Dorman, J., Press, F., Toksoz, N., Sutton, G., Meissner, R., Duennebi,
 2692 F., Nakamura, Y., Kovach, R., Yates, M., 1970a. Seismic data from man-made impacts
 2693 on the moon. *Science* 170, 620–626.
- 2694 Le Feuvre, M., and M.A. Wieczorek (2011) Nonuniform cratering of the Moon and a revised
 2695 crater chronology of inner Solar System, *Icarus* 214, 1–20.
- 2696 Le Pichon, A., Antier, K., Cansi, Y., Hernandez, B., Minaya, E., Burgoa, B., Drob, D., Evers, L.
 2697 G., Vaubaillon, J., 2008. Evidence for a meteoritic origin of the September 15, 2007,
 2698 Carancas crater. *Meteoritics & Planetary Science* 43, 1797–1809.
- 2699 Lognonné P., J. Gagnepain-Beyneix, H. Chenet, A new seismic model of the Moon: implications
 2700 for structure, thermal evolution and formation of the Moon, *Earth Planet. Sci. Lett.* 211
 2701 (2003) 27–44.
- 2702 Lognonné, P, B. Mosser and F.A. Dahlen (1994), Excitation of the Jovian seismic waves by the
 2703 Shoemaker-Levy 9 cometary impact, *Icarus*, **110**, 186-195, doi : [10.1006/icar.1994.1115](https://doi.org/10.1006/icar.1994.1115)
 2704 ,1994.
- 2705 Lognonné, P. and C.L. Johnson (2015). 10.03—Planetary Seismology, in *Treatise on*
 2706 *Geophysics*, 2nd edn. ed. by G. Schubert (Elsevier, Oxford, 2015), pp. 65–120. 978-0-
 2707 444-53803-1. doi:10.1016/B978-0-444-53802- 4.00167-6.
- 2708 Lognonné, P., et al., 2018, “SEIS: The Seismic Experiment for Internal Structure of InSight”,
 2709 this issue.

- 2710 Lognonné, P., & Kawamura, T. (2015). Impact seismology on terrestrial and giant planets. In V.
2711 Tong & R. García (Eds.), *Extraterrestrial Seismology* (pp. 250-263). Cambridge:
2712 Cambridge University Press. doi:10.1017/CBO9781107300668.021
- 2713 Lognonné, P., Karakostas, F., Rolland, L., & Nishikawa, Y. (2016). Modeling of atmospheric-
2714 coupled Rayleigh waves on planets with atmosphere: From Earth observation to Mars
2715 and Venus perspectives. *The Journal of the Acoustical Society of America*, 140(2), 1447-
2716 1468.
- 2717 Lognonné, P., Le Feuvre, M., Johnson, C.L., Weber, R.C. 2009. Moon meteoritic seismic hum:
2718 steady state prediction. *J. Geophys. Res.* 114, E12003.
- 2719 Lognonné, Philippe & Clévéde, Eric. (2002). 10 Normal modes of the earth and planets.
2720 *International Geophysics*. 81. 125-. doi:10.1016/S0074-6142(02)80213-3.
- 2721 Lognonné, Philippe, and B. Mosser. 1993. "Planetary Seismology." *Surveys in Geophysics* 14
2722 (3): 239–302. doi:10.1007/BF00690946.
- 2723 Lognonné, Philippe, and C. Johnson (2007). "Planetary Seismology." In *Treatise on Geophysics*,
2724 vol. 10, 69–122. doi:10.1016/B978-044452748-6.00154-1.
- 2725 Lorenz, Ralph D., and Mark Panning. 2017. "Empirical Recurrence Rates for Ground Motion
2726 Signals on Planetary Surfaces." *Icarus* 303. Elsevier Inc.: 273–79.
2727 doi:10.1016/j.icarus.2017.10.008.
- 2728 Lucas A., C. Narteau, S. Rodriguez, O. Rozier, Y. Callot, A. Garcia, S. Courrech Du Pont,
2729 Sediment flux from the morphodynamics of elongating linear dunes, *Geology*, (2015),
2730 doi:10.1130/G37101.1
- 2731 Maki, et al. (2018) "The Mars Insight Lander Cameras", this issue.
- 2732 Maki, J. N., JF Bell, KE Herkenhoff, SW Squyres, A Kiely, M Klimesh, M Schwochert, T
2733 Litwin, R Willson, A Johnson, M Maimone, E Baumgartner, A Collins, M Wadsworth,
2734 ST Elliot, A Dingizian, D Brown, EC Hagerott, L Scherr, R Deen, D Alexander, J Lorre
2735 (2003) The Mars Exploration Rover Engineering Cameras, *J. Geophys. Res.*, 108(E12),
2736 8071, doi:10.1029/2003JE002077.
- 2737 Maki, J., D. Thiessen, A. Pourangi, P. Kobzeff, T. Litwin, L. Scherr, S. Elliott, A. Dingizian, and
2738 M. Maimone, The Mars Science Laboratory Engineering Cameras, *Space Science*
2739 *Reviews*, 170:77-93, doi:10.1007/s11214-012-9882-4, 2012.
- 2740 Malin M.C. et al., Context Camera Investigation on board the Mars Reconnaissance Orbiter. *J.*
2741 *Geophys. Res.* 112, E05S04 (2007). doi:10.1029/2006JE002808.
- 2742 Malin, M. C., Edgett, K. S., Cantor, B. A., Caplinger, M. A., Danielson, G. E., Jensen, E. H., ...
2743 Supulver, K. D. (2010). An overview of the 1985-2006 Mars Orbiter Camera science
2744 investigation. *The Mars Journal*, 5, 1–60. doi:10.1555/mars.2010.0001

- 2745 Malin, M. C., Edgett, K. S., Posiolova, L. V., McColley, S. M., Dobreá, E. Z. N., 2006. Present-
2746 day impact cratering rate and contemporary gully activity on Mars. *Science* 314, 1573–
2747 1577.
- 2748 Matsumoto K., R. Yamada, F. Kikuchi, S. Kamata, Y. Ishihara, T. Iwata, H. Hanada, S. Sasaki,
2749 Internal structure of the Moon inferred from Apollo seismic data and selenodetic data
2750 from GRAIL and LLR. *Geophys. Res. Lett.* 42, 7351–7358 (2015).
2751 doi:10.1002/2015GL065335
- 2752 May, S. Meteor impact detection on Mars with change detection framework, IEEE IGARSS
2753 2018, submitted.
- 2754 McEwen A.S. et al., Mars Reconnaissance Orbiter’s High Resolution Imaging Science
2755 Experiment (HiRISE). *J. Geophys. Res.* 112, E05S02 (2007). doi:10.1029/2005JE002605
- 2756 McEwen, A. S., Eliason, E. M., Gulick, V. C., Spinoza, Y., Beyer, R. A., and HiRISE Team
2757 (2010). HiRISE: The People’s Camera. *AGU Fall Meeting Abstracts*, abstract #ED23A-
2758 0712.
- 2759 McGarr, A., Latham, G. V., Gault, D. E., 1969. Meteoroid impacts as sources of seismicity on
2760 the Moon. *J. Geophys. Res.* 74, 5981–5994.
- 2761 Melosh, H.J. (1989) *Impact Cratering: A Geological Process*, Oxford Monographs on Geology
2762 and Geophysics. Oxford University Press, New York.
- 2763 Miljkovic, K., E.K. Sansom, I.J. Daubar, F. Karakostas, P. Lognonné (2016) Fate of meteoroid
2764 impacts on Mars detectable by the InSight mission, 47th Lunar Planet. Sci. Conference,
2765 LPI Contribution No. 1768.
- 2766 Miljković, K., G.S. Collins, S. Mannick, P.A. Bland (2013) Morphology and population of
2767 binary asteroid impact craters, *Earth Planet. Sci. Lett.* 363, 121--132.
- 2768 Mimoun, D., Murdoch, N., Lognonné, P., Hurst, K., Pike, W.T., Hurley, J., Nébut, T., Banerdt,
2769 W.B., 2017. The Noise Model of the SEIS Seismometer of the InSight Mission to Mars.
2770 *Space Sci. Rev.* 211, 383–428. doi:10.1007/s11214-017-0409-x
- 2771 Morgan et al. (2018), “A Pre-Landing Assessment of Regolith Properties at the InSight Landing
2772 Site”, this issue.
- 2773 Murchie, Scott L., Raymond E. Arvidson, P. Bedini, K. Beisser, J. P. Bibring, J. Bishop, J.
2774 Boldt, et al. 2007. “Compact Reconnaissance Imaging Spectrometer for Mars (CRISM) on
2775 Mars Reconnaissance Orbiter (MRO).” *Journal of Geophysical Research E: Planets* 112
2776 (5): 1–57. doi:10.1029/2006JE002682.
- 2777 Murdoch, N., Mimoun, D., Garcia, R. F., Rapin, W., Kawamura, T., Lognonné, P., Banfield, D.,
2778 Banerdt, W. B. (2017). Evaluating the Wind-Induced Mechanical Noise on the InSight

- 2779 Seismometers. *Space Science Reviews*, 211(1–4), 429–455. doi:10.1007/s11214-016-
2780 0311-y
- 2781 Nakamura, Yosio. 2011. “Timing Problem with the Lunar Module Impact Data as Recorded by
2782 the LSPE and Corrected Near-Surface Structure at the Apollo 17 Landing Site.” *Journal of*
2783 *Geophysical Research E: Planets* 116 (12): 3–5. doi:10.1029/2011JE003972.
- 2784 Nakamura Y, Lammlein DR, Latham GV, et al. (1973) New seismic data on the state of the deep
2785 lunar interior. *Science* 181: 49–51. [http://dx.doi.org/10.1126/](http://dx.doi.org/10.1126/science.181.4094.49) science.181.4094.49.
- 2786 Nakamura, Y. (2003) New identification of deep moonquakes in the Apollo lunar seismic data.
2787 *Physics of the Earth and Planetary Interiors*, 139(3–4), 197–205.
2788 doi:10.1016/j.pepi.2003.07.017
- 2789 Nakamura, Y. and D. L. Anderson (1979) Martian wind activity detected by a seismometer at
2790 Viking lander 2 site. *Geophysical Research Letters* 6, 499-502.
2791 doi:10.1029/GL006i006p00499
- 2792 Nakamura Y., G.V. Latham, H.J. Dorman, F.K. Duennebieer, Seismic structure of the Moon: a
2793 summary of current status. *Proc. Lunar Sci. Conf.*, 7th (1976), pp. 3113-3121
- 2794 Neslusan, Svoren, Porubcan, A computer program for calculation of a theoretical meteor-stream
2795 radiant, *Astron. Astrophys.* 331, 411–413, 1998
- 2796 Neukum G., R. Jaumann, the HRSC Co-Investigator Team, HRSC, The high resolution stereo
2797 camera of Mars Express. ESA special publications, SP-1240 (2004)
- 2798 Neukum, G., & Ivanov, B. (1994). Crater size distributions and impact probabilities on Earth
2799 from lunar, terrestrial-planet, and asteroid cratering data. In T. Gehrels, M. S. Matthews,
2800 & A. Schumann (Eds.), *Hazards due to Comets and Asteroids* (pp. 359–416). Tucson,
2801 AZ: University of Arizona Press.
- 2802 Neukum, G., & Wise, D. U. (1976). Mars: A Standard Crater Curve and Possible New Time
2803 Scale, *194(4272)*, 1381–1387.
- 2804 Nissen-Meyer, T., van Driel, M., Stähler, S. C., Hosseini, K., Hempel, S., Auer, L., Colombi, A.,
2805 Fournier, A. (2014) AxiSEM: Broadband 3-D seismic wavefields in axisymmetric media,
2806 *Solid Earth* 5, 425-445, doi: 10.5194/se-5-425-2014
- 2807 Nissen-Meyer, T., van Driel, M., Stähler, S. C., Hosseini, K., Hempel, S., Auer, L., Colombi, A.,
2808 Fournier, A. (2014) AxiSEM: Broadband 3-D seismic wavefields in axisymmetric media,
2809 *Solid Earth* 5, 425-445, doi: 10.5194/se-5-425-2014
- 2810 Oberst, J., A. Christou, R. Suggs, D. Moser, I.J. Daubar, A.S. McEwen, M. Burchell, T.
2811 Kawamura, H. Hiesinger, K. Wünnemann, R. Wagner, M.S. Robinson, 2012. The present-
2812 day flux of large meteoroids on the lunar surface—A synthesis of models and
2813 observational techniques, *Planet. Space Sci.*, 74, 179-193.

- 2814 Oberst, J., Nakamura, Y., 1989. A New Estimate of the Meteoroid Impact Flux on the Moon. In:
2815 Proceedings of the Lunar Science Conference XX. pp. 802–803.
- 2816 Panning M. P., P. Lognonné, W.B. Banerdt, R. Garcia, M. Golombek, S. Kedar, B. Knapmeyer-
2817 Endrun, A. Mocquet, N.A. Teanby, J. Tromp, R. Weber, E. Beucler, J.-F. Blanchette-
2818 Guertin, E. Bozdog, M. Drilleau, T. Gudkova, S. Hempel, A. Khan, V. Lekic, N.
2819 Murdoch, A.-C. Plesa, A. Rivoldini, N. Schmerr, Y. Ruan, O. Verhoeven, C. Gao, U.
2820 Christensen, J. Clinton, V. Dehant, D. Giardini, D. Mimoun, W.T. Pike, S. Smrekar, M.
2821 Wieczorek, M. Knapmeyer, and J. Wookey (2017). Planned products of the Mars
2822 structure service for the InSight mission to Mars, *Space Sci. Rev.* 211, 611–650, DOI
2823 10.1007/s11214-016-0317-5
- 2824 Panning M.P., E. Beucler, M. Drilleau, A. Mocquet, P. Lognonné, W.B. Banerdt, Verifying
2825 single-station seismic approaches using Earth-based data: Preparation for data return
2826 from the InSight mission to Mars. *Icarus* 248, 230–242 (2015).
2827 doi:10.1016/j.icarus.2014.10.035
- 2828 Panning, M., Lognonné, P., Banerdt, W.B., Garcia, R., Golombek, M., Kedar, S., Knapmeyer-
2829 Endrun, B., Mocquet, A., Teanby, N.A., Tromp, J., Weber, R., Beucler, E., Blanchette-
2830 Guertin, J.-F., Bozdog, E., Drilleau, M., Gudkova, T., Hempel, S., Khan, A., Lekic, V.,
2831 Murdoch, N., Plesa, A.-C., Rivoldini, A., Schmerr, N., Ruan, Y., Verhoeven, O., Gao, C.,
2832 Christensen, U., Clinton, J., Dehant, V., Giardini, D., Mioun, D., Pike, W.T., Smrekar, S.,
2833 Wieczorek, M., Knapmeyer, M., Wookey, J. (2017) Planned Products of the Mars
2834 Structure Service for the InSight Mission to Mars, *Space Sci. Rev.* 221, 611-650.
- 2835 Passey Q. R. and H. Melosh. Effects of atmospheric breakup on crater field formation. *Icarus*,
2836 42(2):211– 233, 1980.
- 2837 Patton, H. J., Walter, W. R., 1993. Regional moment - magnitude relations for earthquakes and
2838 explosions. *Geophys. Res. Lett.* 20, 277–280.
- 2839 Peterson, J., 1993. Observations and modeling of seismic background noise. U.S. Geol. Surv.
2840 Tech. Rept. 93-322, 1–95.
- 2841 Petersson, N.A. et al. (2010) Lawrence Livermore National Laboratory Technical Report LLNL-
2842 TR-422928.
- 2843 Plesa A.C., M. Grott, N. Tosi, D. Breuer, T. Spohn, M. Wieczorek, How large are present-day
2844 heat flux variations across the surface of Mars? *J. Geophys. Res.* (2016).
2845 doi:10.1002/2016JE005126
- 2846 Plesa, A. C., M. Knapmeyer, M. P. Golombek, D. Breuer, M. Grott, T. Kawamura, P. Lognonné,
2847 N. Tosi, and R. C. Weber. 2018. “Present-Day Mars’ Seismicity Predicted From 3-D
2848 Thermal Evolution Models of Interior Dynamics.” *Geophysical Research Letters* 45 (6):
2849 2580–89. doi:10.1002/2017GL076124.

- 2850 Plescia, Jeffrey B., M.S. S. Robinson, Robert Wagner, and Richard Baldrige. 2016. “Ranger
2851 and Apollo S-IVB Spacecraft Impact Craters.” *Planetary and Space Science* 124 (May).
2852 Elsevier: 15–35. doi:10.1016/j.pss.2016.01.002.
- 2853 Pomeroy, P. W., 1963. Long period seismic waves from large, near-surface nuclear explosions.
2854 *Bull. Seism. Soc. Am.* 53, 109–149.
- 2855 Popova O., J. Borovic`ka, W. K. Hartmann, P. Spurny`, E. Gnos, I. Nemtchinov, and J. M.
2856 Trigo-Rodríguez. Very low strengths of interplanetary meteoroids and small asteroids.
2857 *Meteoritics & Planetary Science*, 46(10):1525– 1550, 2011.
- 2858 Popova, O. P., Nemtchinov, I. V., & Hartmann, W. K. (2003). Bolides in the present and past
2859 Martian atmosphere and effects on cratering processes. *Meteoritics & Planetary Science*,
2860 38(6), 905–925. doi:10.1111/j.1945-5100.2003.tb00287.x
- 2861 Quaide, W.L. and V.R. Oberbeck (1968) Thickness determinations of the lunar surface layer
2862 from lunar impact craters, *J. Geophys. Res* 73, 5247--5270.
- 2863 Register P. J., D. L. Mathias, and L. F. Wheeler. Asteroid fragmentation approaches for
2864 modeling atmospheric energy deposition. *Icarus*, 284:157–166, 2017.
- 2865 Richardson, J. E., & Kedar, S. (2013). An experimental investigation of the seismic signal
2866 produced by hypervelocity impacts. *Lunar and Planetary Science Conference 44*,
2867 Abstract 2863.
- 2868 Richardson, James E., H. Jay Melosh, Richard J. Greenberg, and David P. O’Brien. 2005. “The
2869 Global Effects of Impact-Induced Seismic Activity on Fractured Asteroid Surface
2870 Morphology.” *Icarus* 179 (2): 325–49. doi:10.1016/j.icarus.2005.07.005.
- 2871 Rivoldini, A., Van Hoolst, T., Verhoeven, O., Mocquet, A., Dehant, V. (2011) Geodesy
2872 constraint on the interior structure and composition of Mars, *Icarus* 213, no. 2, 451-472,
2873 doi: 10.1016/j.icarus.2011.03.024
- 2874 Ruff, S. W. and P. R. Christensen (2002) Bright and dark regions on Mars: Particle size and
2875 mineralogical characteristics based on Thermal Emission Spectrometer data. *Journal of*
2876 *Geophysical Research (Planets)* 107, 1-22. doi:10.1029/2001JE001580.
- 2877 Schmerr, N. C., Maria E. Banks, and I.J. Daubar. 2016. “The Seismic Signatures of Impact
2878 Events on Mars: Implications for the InSight Lander.” *LPSC 47*, abstract 1320.
- 2879 Schmidt, R.M., and K.R. Housen (1987), Some recent advances in the scaling of impact and
2880 explosion cratering, *Int. J. Impact Engng.*, 5, 543-560, doi:10.1016/0734-
2881 743X(87)90069-8.
- 2882 Selsis, F., M.T. Lemmon, J. Vaubaillon, J.F. Bell, III, 2005. Extraterrestrial meteors: A Martian
2883 meteor and its parent comet. *Nature* 435, 581, doi:10.1038/435581a.

- 2884 Senft, L.E. and S.T. Stewart (2007) Modeling impact cratering in layered surfaces, *J. Geophys.*
2885 *Res.* 112, E11002, doi:10.1029/2007JE002894.
- 2886 Shean, David E., Oleg Alexandrov, Zachary M Moratto, Benjamin E Smith, Ian R Joughin,
2887 Claire Porter, and Paul Morin. An automated, open-source pipeline for mass production
2888 of digital elevation models (DEMs) from very-high-resolution commercial stereo satellite
2889 imagery. *ISPRS Journal of Photogrammetry and Remote Sensing*, 116:101-117, 2016.
- 2890 Shearer P., *Introduction to Seismology 2nd Ed.* (2009) Cambridge University Press, Cambridge,
2891 412 pp.
- 2892 Shishkin, N. I. (2007) Seismic efficiency of a contact explosion and a high-velocity impact.
2893 *Journal of Applied Mechanics and Technical Physics* 48, 145-152. doi:10.1007/s10808-
2894 007-0019-6
- 2895 Smrekar et al. (2018), “Pre-Mission InSights on the Interior of Mars”, this issue.
- 2896 Sohl, F. and T. Spohn (1997) The interior structure of Mars: Implications from SNC meteorites.
2897 *Journal of Geophysical Research* 102, 1613-1636. doi:10.1029/96JE03419
- 2898 Spohn, T. et al. (2018), HP3 Instrument Paper, this issue.
- 2899 Stevanović, J., Teanby, N. A., Wookey, J., Selby, N., Daubar, I. J., Vaubaillon, J., Garcia, R.,
2900 2017. Bolidé Airbursts as a Seismic Source for the 2018 Mars InSight Mission. *Space*
2901 *Sci. Rev.* 211, 525–545.
- 2902 Sweeney, J., Warner, N. H., Golombek, M. P., Kirk, R., Ferguson, R. L., and Pivarunas, A.,
2903 2016, Crater degradation and surface erosion rates at the InSight landing site, western
2904 Elysium Planitia, Mars (expanded abstract): 47th Lunar and Planetary Science, Abstract
2905 #1576, Lunar and Planetary Institute, Houston.
- 2906 Tancredi, G., Ishitsuka, J., Schultz, P. H., Harris, R. S., Brown, P., ReVelle, D. O., Antier, K., Le
2907 Pichon, A., Rosales, D., Vidal, E., Varela, M. E., Sanchez, L., Benavente, S., Bojorquez,
2908 J., Cabezas, D., Dalmau, A., 2009. A meteorite crater on earth formed on September 15,
2909 2007: The Carancas hypervelocity impact. *Meteoritics & Planetary Science* 44, 1967–
2910 1984.
- 2911 Teanby, N.A., and J. Wookey (2011) Seismic detection of meteorite impacts on Mars, *Phys.*
2912 *Earth Planet. Int.* 186, 70-80.
- 2913 Teanby, Predicted detection rates of regional-scale meteorite impacts on Mars with the InSight
2914 short-period seismometer, *Icarus*, Volume 256, p. 49-62., 2015
- 2915 Thomas, N., Cremonese, G., Ziethe, R., Gerber, M., Brändli, M., Bruno, G., ... Wray, J. J.
2916 (2017). The Colour and Stereo Surface Imaging System (CaSSIS) for the ExoMars Trace
2917 Gas Orbiter. *Space Science Reviews*, 1897–1944. doi:10.1007/s11214-017-0421-1

- 2918 Toksöz, M. N., Press, F., Anderson, K., Dainty, A., Latham, G., Ewing, M., ... Duennebieer, F.
 2919 (1972). Velocity structure and properties of the lunar crust. *The Moon*, 4(3–4), 490–504.
 2920 doi:10.1007/BF00562013
- 2921 Vaubaillon, A confidence index for forecasting of meteor showers, *Planetary and Space Science*,
 2922 Volume 143, p. 78-82., 2017
- 2923 Vaubaillon, Colas, Jorda, A new method to predict meteor showers. I. Description of the model,
 2924 *Astronomy and Astrophysics*, Volume 439, Issue 2, August IV 2005, pp.751-760, 2005
- 2925 Wagner, R. V., Nelson, D. M., Plescia, J. B., Robinson, M. S., Speyerer, E. J., & Mazarico, E.
 2926 (2017). Coordinates of anthropogenic features on the Moon. *Icarus*, 283, 92–103.
 2927 doi:10.1016/j.icarus.2016.05.011
- 2928 Walker, J. D., 2003. Loading sources for seismological investigations of asteroids and comets.
 2929 *Int. J. Impact Eng.* 29, 757–769.
- 2930 Warner N.H., Golombek, M. P., Sweeney, J., Fergason, R., Kirk, R., and Schwartz, C., 2017,
 2931 Near surface stratigraphy and regolith production in southwestern Elysium Planitia,
 2932 Mars: Implications for Hesperian-Amazonian terrains and the InSight lander mission:
 2933 *Space Science Reviews*, 211, 147-190, DOI 10.1007/s11214-017-0352-x.
- 2934 Watters, W. A., L. M. Geiger, M. Fendrock, and R. Gibson (2015), Morphometry of small
 2935 recent impact craters on Mars: Size and terrain dependence, short-term modification, J.
 2936 *Geophys. Res. Planets*, 120, 226–254, doi:10.1002/2014JE004630.
- 2937 Werth, G. C. and R. F. Herbst (1963) Comparison of Amplitudes of Seismic Waves from
 2938 Nuclear Explosions in Four Mediums. *Journal of Geophysical Research* 68, 1463-1475.
 2939 doi:10.1029/JZ068i005p01463
- 2940 Wheeler L. F., P. J. Register, and D. L. Mathias. A fragment-cloud model for asteroid breakup
 2941 and atmospheric energy deposition. *Icarus*, 2017.
- 2942 Whipple, F.J.W. The great Siberian meteor and the waves, seismic and aerial, which it produced.
 2943 *Q. J. R. Meteorol. Soc.* 56, 287–304 (1930)
- 2944 Whitaker, E. A. (1972) Artificial Lunar Impact Craters: Four New Identifications. *NASA Special*
 2945 *Publication* 315, 29-39.
- 2946 Williams, J.-P. 2001. “Acoustic Environment of the Martian Surface.” *Journal of Geophysical*
 2947 *Research E: Planets* 106 (E3): 5033–41.
- 2948 Williams, J.-P., Pathare, A. V., Aharonson, O., 2014. The production of small primary craters on
 2949 Mars and the Moon. *Icarus* 235, 23–36.
- 2950 Woodhouse, J.H. (1988) The Calculation of Eigenfrequencies and Eigenfunctions of the Free
 2951 Oscillations of the Earth and the Sun, 1988. In D.J. Doornbos (ed) “Seismological

- 2952 Algorithms, Computational Methods and Computer Programs”, Academic Press, London,
2953 321-370.
- 2954 Woodhouse, J.H. (1988) The Calculation of Eigenfrequencies and Eigenfunctions of the Free
2955 Oscillations of the Earth and the Sun, 1988. In D.J. Doornbos (ed) “Seismological
2956 Algorithms, Computational Methods and Computer Programs”, Academic Press, London,
2957 321-370.
- 2958 Wunnemann, K., D. Nowka, G.S. Collins, D. Elbeshausen, M. Bierhaus (2011) Scaling of impact
2959 crater formation on planetary surfaces -- insights from numerical modeling, Proc. 11th
2960 Hypervelocity Impact Symposium, No.120.
- 2961 Yasui, M., Matsumoto, E., Arakawa, M., Experimental study on impact-induced seismic wave
2962 propagation through granular materials, Icarus, VOL. 260, pp 320-331, 2015.
- 2963